UNIVERSITÀ
DEGLI STUDI
FIRENZE

PhD in
Atomic and Molecular Photonics

CYCLE XXXIV

COORDINATOR
Prof. Diederik Wiersma

Development of light-responsive materials for biomedical applications

A perspective on the use of Liquid Crystalline Elastomers as artificial muscles and cell culture substrates

Academic Discipline (SSD) CHIM/04

Doctoral Candidate
Dr. Bruno Grandinetti

Supervisor
Prof. Camilla Parmeggiani

Coordinator
Prof. Diederik Wiersma

Years 2018/2021

Abstract

Smart soft materials possess an unmatched potential in biomedical applications. Among them, liquid crystalline elastomers (LCEs) exhibit various properties exploited in the fabrication of microrobots and responsive coatings, and, very recently, also in the design of biomedical implants and devices. LCEs are shape-changing materials able to modify their structure upon stimulation, generating tension during this process. Biocompatibility and cell-instructiveness have been demonstrated for different classes of LCEs, whose mechanical properties and response time can be easily tuned. The research presented in this Thesis follows two applications of LCEs in the biomedical field.

In the first part of the study, LCEs were investigated as artificial muscles. Starting from the demonstration of the ability of films obtained from a light-responsive LCE mixture in assisting cardiac contraction, its composition was tuned to improve its performance, and completely characterized in terms of efficiency, level of tension developed upon stimulation and kinetics of force development. The aims of the work were to find the correct light stimulation pattern and azobenzene-based dye to enhance its capabilities in muscle assistance and to miniaturize an implantable LCE-miniLED device.

In the second part of the research, the ability of different supports to direct cell culturing was approached. The effect of different surface patterning methods on two different materials on cell adhesion and growth was evaluated. In the first study, the ability of linear motifs in directing cell alignment and growth of cardiomyocytes derived from human induced pluripotent stem cells, on hydrogels made of commercially available polymers, was pinpointed. Substrate rigidity was modulated to assess the relation between this parameter and cell functionality. The focus of the second study was the development of reconfigurable coatings based on light-responsive LCEs. Surfaces were patterned with fingerprint-like structures, which arose from self-assembly of a mixture of mesogenic monomers doped with a chiral crosslinker. The surfaces possessed hills and valleys with different molecular alignment, that underwent topography inversion upon irradiation. Different types of coatings were prepared, tuning pattern spacing, roughness and actuation level. The biocompatibility of the materials was studied in view of their use as active cell culture scaffolds capable of live stimulation of cultured cells.

Preface

Materials Science and Engineering have evolved throughout the whole history of mankind, determining the milestones of its evolution: from the Bronze Age to the Silicon Age, from the first ceramics to plastics, from the discovery of building materials, capable of challenging time and ageing, to the exploration of the infinitely small, a world dominated by nature's most fascinating physical and chemical phenomena.

The rise of microelectronics and nanotechnology, the need for energy-harvesting materials, new frontiers in tissue engineering and biomedical engineering, *smart* materials: social needs and scientific challenges move the progress in this interdisciplinary field, whose roots continuously breathe new life from physics, chemistry, engineering, biotechnology and to which nature is always a trove for new ideas.

Smart materials, in this context, are a hot topic in materials research. A first definition of smart materials can be found in a paper by T. Takagi, who described *intelligent* materials, in 1990, as materials that can respond to external stimuli and adapt to them consequently; nowadays, this idea is still generally accepted by the scientific community to describe a smart material.[1]

Throughout the years, a plethora of smart materials has emerged, both organic and inorganic, that rely on different working principles and stimuli (heat, light, chemical signaling, electric/magnetic fields, etc.) to adapt their properties. Their applications span from adaptive optics to industrial actuators, to the manufacturing of devices in the healthcare field to aerospace engineering. Among the different types of smart materials, *soft* actuators are appealing for applications in biomedical engineering, since their mechanical properties are compatible with those of biological tissues; this feature allows them to interact more easily with soft systems than *hard* materials can do.

The objectives of this Thesis work are part of a wider research project, carried out at the research group of Optics of Complex Systems at the European Laboratory for Non-Linear Spectroscopy (LENS) at Università degli Studi di Firenze, on the possibilities to use liquid crystalline elastomers (LCEs) to design cardiac contraction-assist devices and

artificial muscles and to take advantage of the particular properties of these polymers in the preparation of new substrates for cell cultures.

LCEs are an emergent class of smart materials, and were first theorized by P. G. De Gennes in the 1970s.[2] They share their properties with liquid crystals (LCs), from which they take their high degree of order and intrinsic responsiveness, and with elastomers, whose mechanical properties are similar to those of rubber and can be tuned via the modification of the crosslinking degree of their network.

Starting from earlier results that demonstrate the ability of LCEs to contract and generate force upon stimulation and their biocompatibility, the aims of the research that underlies this Thesis project were:

- The optimization of the properties of light-responsive materials towards their use in the design of a cardiac contraction-assist device, via the insertion of different dyes that respond to different visible light wavelengths and modulation of stimulation pattern.
- The use of LCEs as scaffold for cell cultures, based on the recent findings that show their biocompatibility and cell-instructiveness, thanks to the ease in surface patterning of these materials.

The first chapter of this Thesis work focuses on the working principles of LCEs and photoactive soft materials.

The second chapter deals with the use of LCE mixtures to prepare photoactive materials towards assistance in heart contraction, with an insight into the possibilities offered by shape-changing materials in the field of biomedical engineering and tissue engineering. This work was conducted in collaboration with the Division of Physiology of the Department of Experimental and Clinical Medicine at the Università degli Studi di Firenze, the National Institute of Optics of the Italian Research Council (CNR-INO), Delft University of Technology (TU Delft) and the partners of the European project REPAIR. The objective of the research was to develop a new lightweight untethered contraction assist device based on a LCE material, starting from the early results contained in the work by Ferrantini *et al*, who offered a proof of concept of the use of such polymers to assist cardiac contraction in murine muscles *ex vivo*; the aim of the use

of LCEs as a cardiac artificial muscle is to overcome the limitations of the currently marketed devices used in the field of cardiovascular surgery.[3]

In the third chapter, substrate patterning to control cell adhesion and growth is discussed. The results of the use of linearly patterned substrates, prepared via soft lithography on commercially available hydrogels for cell growth of cardiomyocytes derived from human induced pluripotent stem cells (hiPSC-CMs), are presented. Such ordered structures had the aim to help cell alignment and maturation towards adult and full functional hiPSC-CMs *ex vivo*.[4] In a similar way, another surface patterning approach, which relies on the self-assembly of chiral LC monomers, was used to obtain surfaces with responsive *fingerprint* motifs. The effect of this shape-changing grooved structure on the functionality and growth of two cell lines was assessed, along with their properties upon stimulation, to prepare materials with reprogrammable surfaces for tissue engineering. The use of reprogrammable surfaces aimed at mimicking the characteristics of the extracellular matrix, which is a dynamic system where topographical stimuli change throughout the growth of cells. LCEs were chosen thanks to their demonstrated ability to host certain types of cell cultures helping their alignment. The research was carried out in collaboration with the research group of Stimuli-Responsive Functional Materials and Devices (SFD) at Eindhoven University of Technology (TU/e).

1. Introduction

1.1. Liquid crystals: general concepts

Liquid crystals (LCs) are a class of substances whose properties lie between those of crystalline solids and those of isotropic liquids.

In the crystalline phase, molecules or atoms are arranged in a lattice structure with long-range positional and orientational order, while the isotropic liquid phase is totally disordered, with molecules having neither positional order nor orientational one. LC *mesophases*, instead, possess a certain degree of orientational order, but molecules are positionally disordered and are allowed to flow. This particular condition is allowed by the high anisotropy displayed by their molecules, which accounts for the partial order of liquid crystalline mesophases.[5,6]

Molecules in liquid crystal mesophases are oriented, on average, following a direction identified by the *molecular director* (**n**).

Liquid crystals are divided into two categories:

- *Lyotropic* LCs, composed of mixtures of organic amphiphilic molecules (showing, thus, a polar head and a hydrophobic tail) in a polar or nonpolar solvent, whose molecules aggregate in nanosized non-spherical clusters and for which transitions from a mesophase to another one are dependent on liquid crystalline species concentration and/or temperature;
- *Thermotropic* LCs, in which transitions from a mesophase to another occur when temperature varies.

The most important features that make a substance display thermotropic mesophases are the presence, within its structure, of both a stiff central core and an aliphatic side chain. The former is, generally, composed of aromatic rings linked through strong bonds, such as double bonds or ester groups; the latter must be flexible and long enough to disturb the order of the aromatic core. The tendency of the former to organize itself in a crystalline lattice is, indeed, contrasted by the mobility of the latter; the interplay between these two opposing factors favors liquid crystallinity.[5,6]

An example of the structural characteristics of a LC molecule is 5CB, 4-cyano-4'-pentylbiphenyl, one of the first commercial synthetic LCs (depicted in Figure 1.1). In this molecule, it is possible to observe all the basic components of a LC molecule: a rod-like shape with high aspect ratio, the stiff biphenyl core, the aliphatic five-term tail and a nitrile substituent that gives the LC a strong dipole.

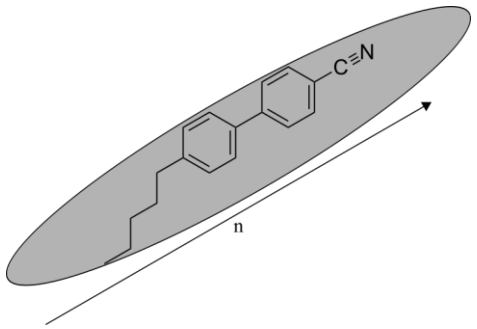

*Figure 1.1: Chemical structure of 5CB liquid crystal, where the **n** vector is the molecular director.*

The order in a LC is given quantitatively by the value of its *scalar order parameter*, conventionally indicated with *S*. It measures how packed and organized molecules are in a LC, taking into account the fluctuations of the angle between the director and molecule long axis; *S* is defined as:

$$S = < \frac{1}{2}(3cos^2\theta - 1) > = \int \frac{1}{2}(3cos^2\theta - 1) f(\theta) d\Omega \qquad \text{Equation 1.1}$$

where Ω is the solid angle and $f(\theta)$ is molecule orientation distribution which satisfies the normalization condition $\int_0^\pi f(\theta) sin\theta d\theta = 1$. The order parameter ranges from 0 (complete disorder) to 1 (crystalline solid) and is strongly dependent on temperature.[5,6]
Thermotropic LCs undergo phase transition from crystalline to liquid crystalline at a certain temperature, known as *melting temperature*; if temperature is raised to their *clearing temperature*, they become isotropic liquids.
Different types of thermotropic LCs have been characterized in the last century. Depending on their shape, they are categorized into *calamitic*, *discotic* or *bent-core* LCs. Calamitic LCs are rod-shaped molecules, which are highly anisotropic and, sometimes, possess a strong molecular dipole along their major axis. Discotic LCs have disk-like shape and possess two-dimensional positional order, stacking themselves in columnar mesophases. Bent-core LC molecules (sometimes referred to as *banana*-shaped LCs)

were discovered later than the other two types of thermotropic LCs, and present exotic mesophases.

Thermotropic calamitic LCs only were used throughout this work, and the following discussions and results of this thesis will only take into account this type of LCs. The most famous calamitic mesophases are depicted in Figure 1.2, each one with its own molecular ordering, depending on the variations of orientation of the molecular director. The simplest calamitic LC mesophase is the *nematic* one (conventionally indicated with *N*). Molecules in the nematic mesophase do not possess any residual positional order and are arranged in order for molecular axes to be parallel one another along the direction of the molecular director. The system is axisymmetric, and the presence of such a privileged alignment makes nematic LCs birefringent.

Smectic LC mesophases retain a higher level of positional order compared to nematic ones; these are more viscous than nematic LCs since molecules can move freely between two layers, but inter-layer movement is restricted. The most important ones, which are of interest for technological applications and are the most common among the other smectic mesophases, are *A* and *C* phases. Smectic *A* mesophase (S_A) presents molecules stacked on consecutive parallel layers, with molecule long axis perpendicular to layer planes; in smectic *C* mesophase (S_C) molecules are tilted and are not aligned with the smectic plane normal direction.

The mesophases that have been described so far are typical of molecules (or mixtures of molecules) lacking chirality; in presence of chiral molecules, S_C phase is substituted with the smectic C^* mesophase, while nematic mesophase is replaced by the *chiral nematic* or *cholesteric* (N^*) mesophase. In such phases, a helicoidal molecular organization is present. Cholesteric LCs have the same positional disorder as nematic ones, but the molecular director, in this case, continuously changes its direction describing a helix; molecules complete a 360° full turn after a certain distance known as *cholesteric pitch*. Smectic C^* LCs are analogous to smectic C ones; molecules are stratified, and the director changes its direction describing a helix with *p* pitch, after which molecules have completed a whole 360° turn.

If a transition between two different LC phases occurs above the melting temperature and it is observed both on heating and cooling, it is said to be *enantiotropic* and is thermodynamically stable; on the other hand, when a transition between two LC phases occurs during the cooling from the melt only, it is said to be *monotropic* and it is not thermodynamically stable.

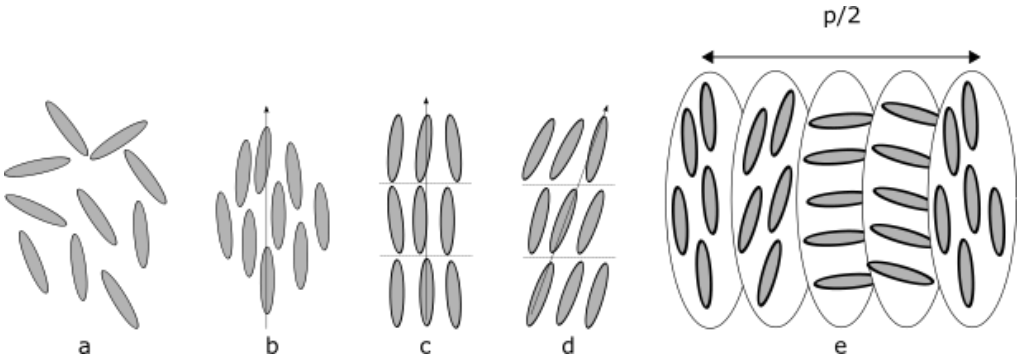

Figure 1.2: Different mesophases for thermotropic calamitic LCs. From left to right: isotropic (a), nematic (b), smectic A (c), smectic C (d), and chiral nematic (e) mesophases (where p *is pitch length in the case of the chiral nematic mesophase).*

If a LC possesses both a smectic and a nematic phase (or, in the case of chiral systems, smectic C^* and cholesteric mesophases), smectic-to-nematic (SI) transition temperature will occur at a lower temperature compared to nematic-to-isotropic (NI) one (with the isotropic liquid phase commonly indicated with the letter *I*), being the former more ordered than the latter.

Different techniques can be used to investigate LC transitions and molecular organization. The easiest one is differential scanning calorimetry (DSC), which measures the change of enthalpy in the transition from crystalline phase to a LC mesophase to isotropic liquid phase. Observing a DSC trace, it is possible to characterize transition temperatures, taking into account that typical values of enthalpy change in crystalline-to-nematic transition are in the order of 30-50 kJ/mol, while a LC-to-isotropic phase changes or transitions between smectic and nematic phases present smaller enthalpy changes, in the order of 1-2 kJ/mol.[6]

X-ray diffraction (XRD) and polarized optical microscopy (POM), instead, give information about the spatial arrangement of molecules in LCs. Every LC mesophase

possesses its own X-ray scattering pattern and its own lattice defects; the latter, visible by analyzing the LC between two polarizers, can be inspected through POM to fully understand which LC mesophases a certain substance exhibit. A typical characterization of a nematic molecule is reported in Figure 1.3. Below 55°C, the LC mixture is in its nematic mesophase: it can be deduced from the POM image, in which both two-brush and four-brush Schlieren textures appear; above T_{NI} the POM image is completely dark, meaning that the sample is in its isotropic phase and does not show birefringence.

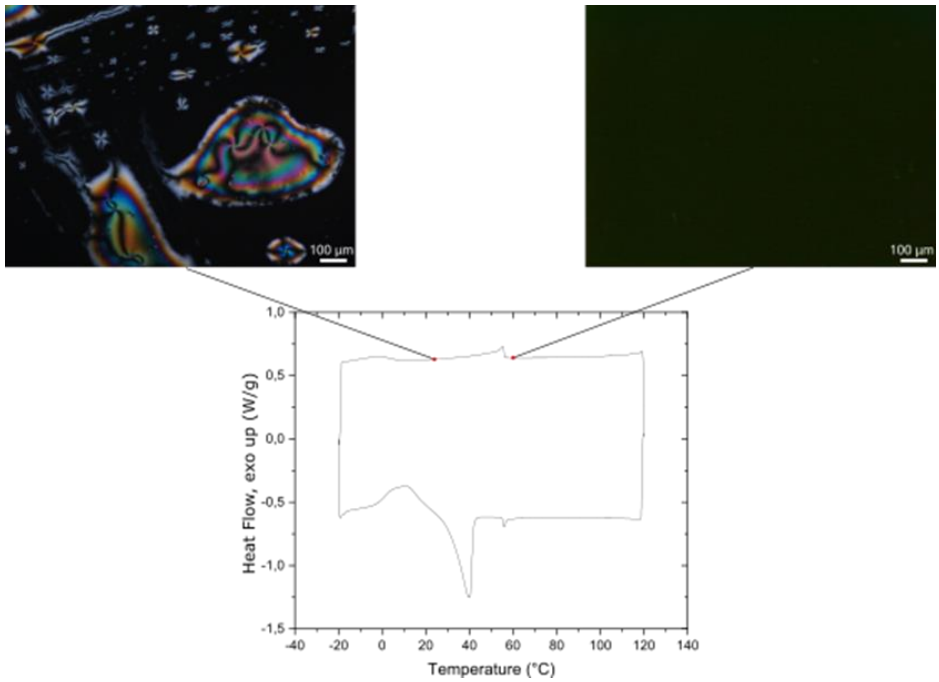

Figure 1.3: DSC sample trace of a nematic LC (2nd heating and cooling cycles are shown), with POM images at room temperature (left) and at 60°C (right).

The main field of application of LCs, indeed, has been the manufacturing of optical devices, due to their particular optical properties, which arise from their intrinsic anisotropy, exploitable in non-linear optics or manufacturing of opto-electronic devices. LC molecules are birefringent, meaning that they possess two refractive indexes in the different directions of the volume occupied by the LC mixture: one accounts for the light that propagates parallelly to the director, and the other one for the light that propagates perpendicularly to it. When polarized light impinges on a LC sample, it will allow faster

propagation of light in the direction of the molecular director than light that is polarized perpendicularly to the director. When exiting the sample, being the two rays out of phase, light will have a new polarization direction. A measure of the optical properties of a LC is its *dielectric anisotropy*, $\varepsilon = \varepsilon_{//} - \varepsilon_{\perp}$, which is the difference between the dielectric constants of the LC parallelly and perpendicularly to the director.[6]

1.2. Liquid Crystalline Elastomers

In the last 40 years, different classes of polymers capable of displaying liquid crystalline mesophases, referred to as liquid crystalline polymers (LCPs), have been developed. LCPs comprise a wide set of materials, from commercial main-chain performance materials such as Kevlar © or Vectra © and some natural biopolymers, to the densely crosslinked glassy LC networks (LCNs) obtained from the polymerization of polyfunctional LC monomers.[7,8]

LCEs lie between these two classes of LC materials described above, and exhibit a slightly crosslinked network in which the mesogens are linked to a main flexible polymer chain and the chains are not densely crosslinked. Their particular molecular structure, which derives from mesogenic molecules and is highly anisotropic, enables them a set of properties which is not easily displayed by other types of soft systems: LCEs, being liquid crystalline, are intrinsically responsive to thermal variations, for instance. Any change in the order at a molecular level reflects itself in a reversible macroscopic shape change that is reversible upon cooling; in addition to shape change, their color can also vary upon stimulation, and these modifications are larger than in LCNs and experienced by the polymers with little energy cost.[7,9,10] LCEs were theorized by P.G. De Gennes in 1975, and were immediately regarded as potential candidates to design an artificial muscle.[2,11] First synthesis attempts were carried out between the late 1970s and the 1980s.[7]

1.1.1 Alignment in Liquid Crystalline Elastomers

Lattice defects in unconstrained LCs arise because of the presence of different domains, each one locally aligned following the direction of the molecular director.[5,6]

Though, the direction of the molecular director can be spatially programmed in order to obtain monodomain samples with long range alignment: the easiest and most common methods are the use of electric or magnetic fields or the action of an anisotropic surfactant on a coated substrate; the alignment of LCs plays an important role in determining their optical properties, and it is crucial in LCEs to give them the particular mechanical properties they exhibit.[12,13]

Surface effects are easier to be exploited than the application of electric/magnetic fields to align LC molecules. Taking into account nematic LCs, these can be *anchored* onto surfaces in three different ways, according to the angle θ between the director and the surface plane (Figure 1.4):

- If θ = 90°, LC molecules are oriented perpendicularly to the substrate, and the configuration is said to be *homeotropic*;
- If θ = 0°, then the director lies parallelly to the surface plane; this anchoring condition is referred to as *planar* anchoring;
- If 0° < θ < 90°, the anchoring is *tilted*.

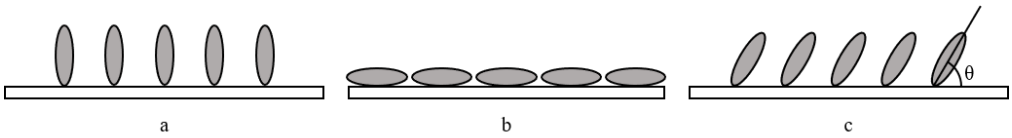

Figure 1.4: Anchoring in LCs. Homeotropic (a), planar (b) and tilted (c) anchoring onto surfaces.

One easy way to take advantage of surface effect to create planar homogeneous alignment is the *rubbing* method. The glass substrates that will host the LC substance are coated with a thin polymer layer, either a polyimide or poly(vinyl alcohol) (PVA) in most cases, usually via spin coating. These coated substrates are then rubbed unidirectionally with a velvet cloth. This way, the interaction energy between the LC and the polymer is minimized only if the molecular director has the same orientation as the rubbed film, and the LC molecules are forced to follow this pre-programmed direction. Rubbing method relies on different types of interaction phenomena between the LC and the polymer layer: through the buffing of the polymer layer, microgrooves are introduced in the polymer film, and polymer chains are re-oriented favoring van der Waals interactions between them and the LC molecules. Other secondary effects (such

as creation of surface charges) could also play a role in the alignment of LCs. Homeotropic anchoring is obtained by using other kinds of surface agents, such as silanes with long alkyl chains (that force the rod-shaped LC molecules to align perpendicularly to the polymer film) or amphiphilic species. Tilted alignment is achieved with the use of particular types of aligning polymers.

One of the most common methods to fabricate LC layers is to use two aligning substrates divided by a spacer whose thickness is known (for instance silica beads or Mylar films). Then, when the LC substance is infiltrated in the hollow space between the two substrates, it is aligned following the anchoring direction dictated by the surfactants on both surfaces. This kind of sample is known as a *LC cell*.

The use of two aligning substrates with different orientations generates a continuous variation of the direction of the molecular director in the space, leading to different possible alignment conditions for LCs. Considering nematic LCs, it is possible to have four different configurations (Figure 1.5):

- Planar homogeneous alignment, when uniaxially rubbed surfaces are used, and the rubbing directions lie parallelly one another;
- Homeotropic alignment, when two homeotropically-aligning substrates are used;
- Twisted alignment, when two planarly-aligning substrates are used with their alignment directions at an angle that is different from 0°;
- Splayed alignment, when a homeotropic and a planar substrate are used: this way, the molecular director changes its direction continuously from one plane to the other, describing a fan and going from 0° to 90° in the plane perpendicular to the two substrates.

The latter two cases, then, induce a distortion of the director throughout the whole volume of the LC substance.

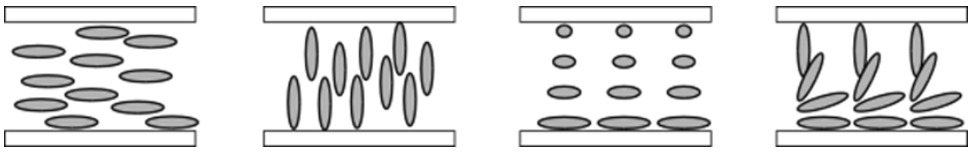

Figure 1.5:Different alignments of LC molecules in a cell. From left to right: planar homogeneous, homeotropic, twisted and splayed alignment.

As mentioned before, there exist other methods to program the direction of the molecular director; one feasible way to obtain planar substrates is to use photoactive polymer layers, which reorient themselves when polarized light is shone on them (*photoalignment* technique). This way, the disadvantages of the rubbing method (such as leaving dirt on the polymer layer, introducing defects in it) could be avoided, while also enabling the creation of complex alignment patterns through the use, for instance, of particular photomasks or laser projectors.[14] Even though it is straightforward to obtain well-aligned LC samples via the use of surfactants and LC cells, this method also poses a geometrical constraint on the size of the LC device: this cannot exceed the size of the aligning substrate, and for large samples homogeneity in sample thickness and alignment in all of its zones could be an issue. Electric-field-driven director reconfiguration is the principle that underlies how LC displays (which have dominated the market for years until the advent of organic-light-emitting-diode and plasma displays) work. This method relies on the torque exerted by the electric field on the dipoles in LC molecules, to re-orient; the direction of the reorientation is related to the sign of the dielectric anisotropy of the LC substance. Similarly, magnetic fields can also be used to align LCs. However, the main downside of aligning LCs through magnetic or electric fields are the high field strengths sometimes required (7-11 T for magnetic fields, for instance), which are difficult to be easily achieved. The methods so far discussed are borrowed from low-molecular weight LC physics; in slightly crosslinked systems as LCEs, alignment can also be obtained through mechanical stretching of the sample.[15]

Alignment in LCEs is the driving force behind their shape-changing properties. Loss of order in the polymer slightly crosslinked network, indeed, is translated into a macroscopic change of shape, whose path is pre-programmed through alignment. In Figure 1.6, the mechanism underlying shape change is depicted. Chains in nematic LCEs can have two possible configurations: linear or hairpin; upon transition from nematic to isotropic, chains in the network assume a random coil configuration. This loss of order in the polymer network drives the macroscopic shape change.[10,16] LCEs with planar alignment can contract uniaxially along the direction of the molecular director, and so

do LCEs with homeotropic alignment. LCEs in splayed and twisted alignment exhibit, respectively, bending and twisting when LC order decreases.

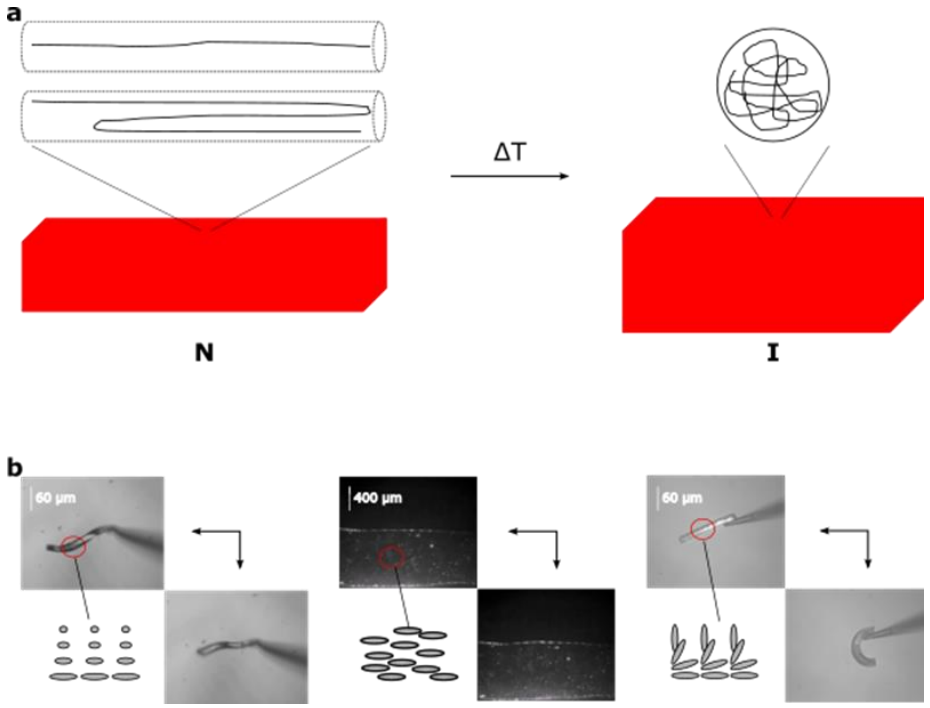

Figure 1.6: Shape change in LCEs. (a): Transition between linear/hairpin and random coil configurations in LCEs. (b): Possible deformations depending on the alignment of LCEs. From left to right: rotation in LCEs with twisted alignment (in a micrometer-sized actuator); contraction in LCEs with planar homogeneous alignment (strip from a LCE film); bending, enabled by splayed alignment (in another micrometer-sized structure). The frame in the central part of (b) is taken from ref. 3*; the other frames are taken from unpublished videos that are a kind courtesy of dr. D. Martella and dr. S. Nocentini.*

Throughout this Thesis work, LC samples were aligned mainly via the use of polyimide or PVA coating and the manufacturing of LC cells.

1.2.1 Architectures and synthetic methods of Liquid Crystalline Polymers

LCEs are composed of mesogenic units embedded in a polymer chain. Mesogens can be linked to the polymer backbone in two ways: either throughout the length of the polymer chain or with mesogens linked to the polymer chains as pendant groups. The first architecture results in a structure referred to as *main-chain* (MC) LCE, while the latter as *side-chain* (SC) LCE. Another difference stands between polymers which have

mesogens linked to the backbone through their ends (*end-on*) or perpendicularly to their long axes (*side-on*). Thus, four types of architectures of LCPs can be distinguished, depicted in Figure 1.7.

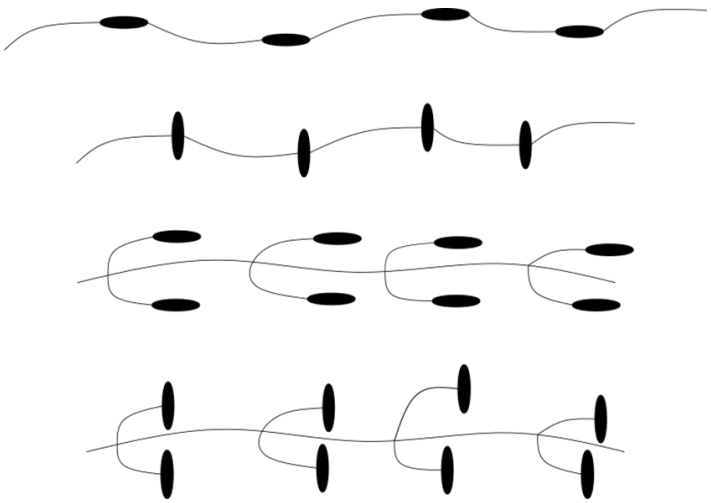

Figure 1.7: Different architectures for LCPs. From the top to the bottom: main-chain end-on and main-chain side-on LCPs, side-chain end-on and side-chain side-on LCPs.

MC-LCEs display a high degree of coupling between the mesogens and the backbone; it reflects in a higher actuation degree compared to side-chain systems, at the expense of a slower response in time. Such a high orientational order, though, is beneficial for their mechanical properties. On the other hand, since SC-LCEs are faster than MC ones, they find applications in electro-optics, where response time is crucial in devices.[9,11,13] Ever since the first trials in synthesizing LCEs, various synthetic pathways have been explored.

Even though SC-LCEs have been developed more extensively than MC ones, these ones have gained interest because of their high degree of anisotropy and coupling between the backbone and the LC mesogens; these features enable them a higher level of actuation and greater energy dissipation compared to SC-LCEs.[13] These favorable properties come at expense of more challenging processing (due to their tendency to crystallize and the generally high clearing temperatures) and synthesis.[11] Indeed, preparation strategies are mostly limited to step-growth reactions.

A pioneering study was presented by Bergmann *et al.*, who synthesized a MC-LCE (Scheme 1) exploiting hydrosilylation of a vinyl-ended prepolymer with a four-arm cyclosiloxane crosslinker.[17]

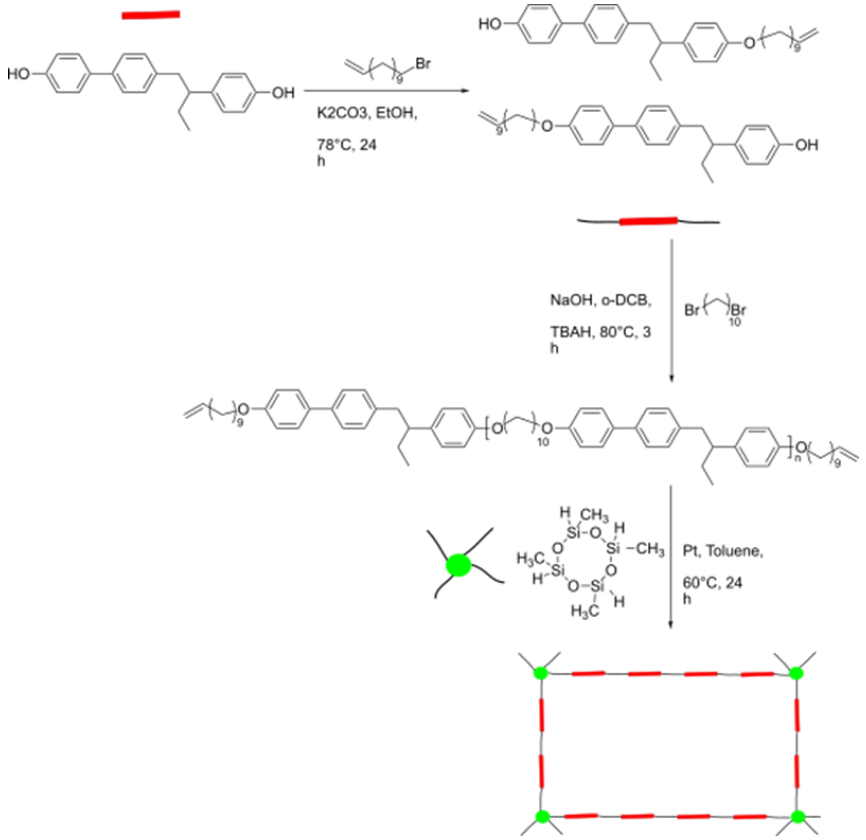

Scheme 1: Synthesis of a MC-LCE through hydrosilylation, from ref. 17.

Other feasible strategies to synthesize a MC-LCE are the use of a UV-mediated crosslinking of LC prepolymers functionalized with pendant benzophenone groups,[18] or through the routes opened by thiol-ene *click* reactions, which nowadays constitute one of the paradigms for the 3D printing of LCE-based materials. The first works on 3D printing of MC-LCEs were presented in 2017 by Ambulo *et al.* and Lopez-Valdelolivas *et al.* The two research groups independently designed a pathway based on Michael addition of diacrylate mesogens and, respectively, either a dithiol or a primary amine chain extender to synthesize a prepolymer retaining acrylate ends for subsequent crosslinking under UV irradiation. Alignment was obtained through shear while the

LCE-based ink was deposited on the printing stage. Further research dealt with printing parameters, the influence of crosslinking reaction and the dithiol spacer used.[19–22]

Historically, the first and most common two routes to synthesize SC-LECs have mainly been hydrosilylation reaction and radical polymerization.

The former exploits the Pt-catalyzed reaction between a siloxane group and an unsaturated C=O or C=C bond, and it was developed by Kupfer and Finkelmann (Scheme 2). In the first step, the reaction between the vinyl groups and the polysiloxane is catalyzed by a Pt-cyclooctadiene complex, and a slightly crosslinked system is obtained; the methacrylate ends do not react as fast as the vinyl in the former step. The crosslinking is then completed via heating and under mechanical stretching to align the mesogen and evaporate the solvent, and a monodomain LCE is obtained.[15]

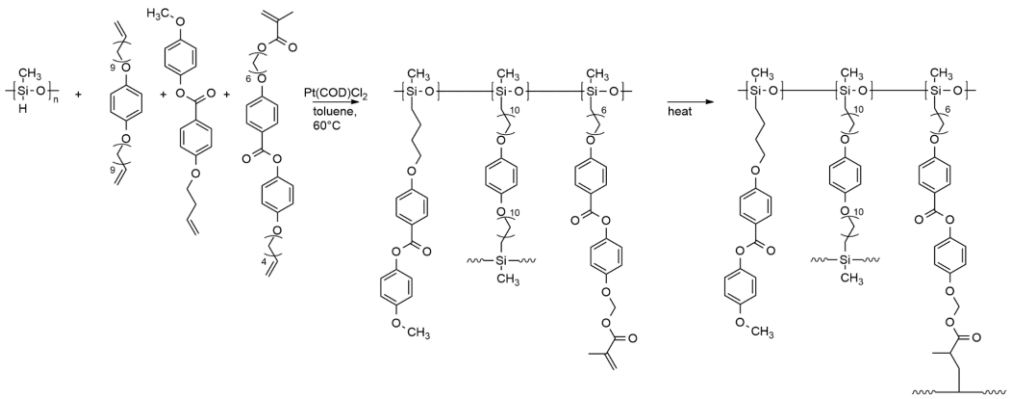

Scheme 2: SC-LCE prepared via hydrosilylation reaction between a siloxane precursor (n~100), a divinyl crosslinker, a polymerizable vinyl mesogen and a bifunctional LC crosslinker with a methacrylate end and a vinyl one (from ref. 15*).*

Radical polymerization allows easy preparation of LCEs; plus, a plethora of polymerizable LC monomers is available, allowing a degree of tunability of mechanical/thermomechanical properties of the LCEs obtained through this technique that is not easily accessible by the other synthetic routes. Moreover, its versatility lies in the mild conditions needed for the radical polymerization to be carried out, in its fast kinetics and in the various commercially available monomers on the market. These can be mixed with the LC species to further widen the spectrum of the tunability of the LCEs. Initiation can be guaranteed via the use of photo-responsive initiators, which are

commercially available and span a long range of wavelengths to which they are reactive. Thermal initiators are also available and widely employed.

As an example, Thomsen *et al.* prepared two different SC side-on LCEs exploiting two different mesogens crosslinked with 1,6-hexanediol diacrylate, using a photoinitiator to start the polymerization under UV light irradiation (Scheme 3). The mixture was aligned uniaxially via the surface effect of two rubbed PVA-coated glass slides.[23]

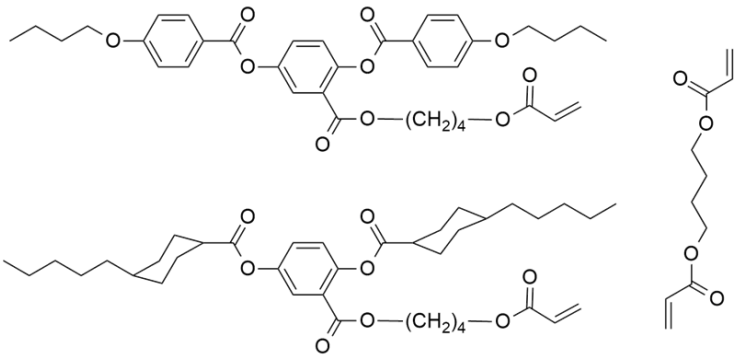

Scheme 3: Radical polymerization of acrylate-ended mesogens towards the preparation of LCEs. An example of LC mesogens and a commercial diacrylate crosslinker usable to prepare a LCE (as in ref. 23*).*

Schuhladen *et al.*, later, used a similar LCE mixture to prepare an electrical driven iris which closed itself upon heating via Joule effect. Radial alignment of LC mesogens was obtained through the use of a magnetic field.[23,24]

The drawbacks of radical polymerization, though, lie in its ease. It is oxygen-sensitive, thus in most cases it must be conducted in inert atmosphere; acrylates exhibit a large polymerization shrinkage, and this could lead to brittle and fragile networks; bulk polymerization could not be effective due to autoacceleration processes or cage effect; copolymerization of different mesogens is random and cannot be controlled; termination reactions are of different nature, and thus dispersity is high. To circumvent these disadvantages, polymerizable LCs with epoxide, oxetane or vinyl ether ends have been synthesized, to polymerize them in ionic polymerization conditions.[9,11]

However, the great advantage of using radical polymerization in the context of preparation of LCEs is the ease in aligning low-molar-mass LC monomers before and during the polymerization process, which overcomes the limitations of the two-step crosslinking process described above. Indeed, while planar alignment only is accessible

through alignment via mechanical stretching, the use of a low-viscosity mixtures of monomers and crosslinkers enables the alignment of LCs to be carried out via the use of external fields or surfactants, for instance. Thus, complex actuation paths can be achieved, besides uniaxial contraction; examples of LCE samples capable of macroscopically bending, twisting, rotating have been reported in literature.[7,9,12,25,26]
Other feasible alternatives to the processes described above are, for instance, the method developed by Komp *et al.*, who used UV-mediated H-abstraction on a weak C-H bond by a benzophenone side group (Scheme 4), or the grafting of LC mesogens onto polymeric supports, among others.[27,28]

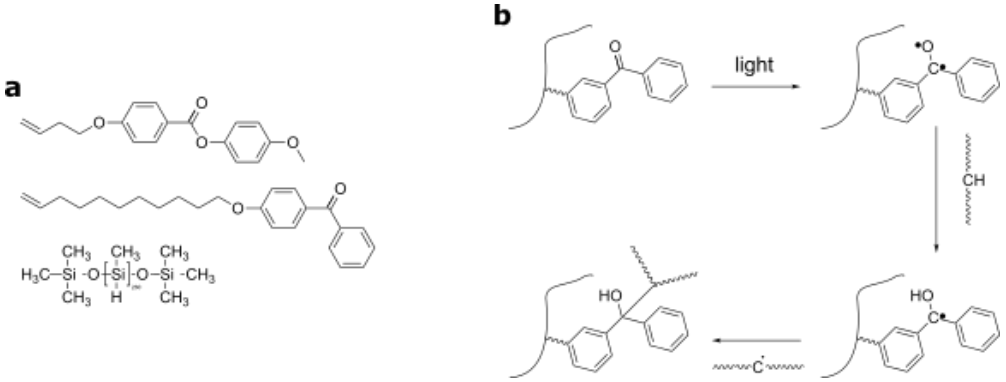

Scheme 4: Crosslinking via benzophenone-mediated H-abstraction triggered with UV light, as in ref. 27. *(a): A SC-LCE is prepared via addition of vinyl-based monomers to the siloxane chain. Among the vinyl monomers, the topmost one is a polymerizable LC, while the other carries the crosslinkable benzophenone group. (b): Scheme of the H-abstraction and crosslinking of the chains.*

Other synthetic protocols allow the formation of mixed systems, whose main advantage compared to SC- or MC-LCEs is the high contraction they exhibit upon stimulation. Wermter *et al.* used an approach similar to the one developed by Bergmann to crosslink a SC side-on LC polymer using a MC end-on vinyl-ended prepolymer. Thus, they obtained a mixed MC/SC-LCE, which presents a high length contraction when aligned in a single monodomain.[29] In particular, click chemistry based on sulphur-containing moieties has been widely used through the last years in the context of the synthesis of LCEs. Hong *et al.* used the approach developed by Lub *et al.* to prepare homeotropically-aligned pillared structures based on thiol-ene radical photopolymerization. They obtained arrays of soft posts based on MC-LCEs capable of contracting up to 300-400%

of their initial length.[30] Martella *et al.* were the first to exploit thiol-yne click chemistry to design a mixed MC/SC-LCE capable of a high degree of actuation (40-50% contraction). This synthetic pathway was also used in a later work by Lupi *et al.*, who confirmed the effectiveness of this route towards the preparation of LCEs capable of 50% contraction in length.[31,32] Other click-chemistry-based approaches towards the synthesis of LCEs take into account, for instance, the widely known copper-catalyzed azido-alkyne coupling (CuAAC) to graft azide-functionalized mesogens onto alkyne-bearing polymers (or vice versa).[33,34]

The field is constantly growing and gaining inspiration from all the techniques offered by macromolecule engineering and is extensively reviewed in literature.[35]

1.3. Photoactive Liquid Crystalline Elastomers

The use of light as activation stimulus for actuators has always drawn the attention of researchers due to its advantages compared to other kinds of triggers. Indeed, light enables untethered actuation and a high degree of spatial and temporal resolution, due to the various types of light sources and chromophores (both organic and inorganic) that are available nowadays. This degree of accuracy is unattainable for other types of stimuli, and this makes the use of light highly desirable.

A feasible strategy to trigger nematic-to-isotropic transition in LCEs is the incorporation of nanomaterials, such as, as an example, metal nanoparticles or carbon-based nanomaterials in their network. The field of LCE nanocomposites is widely reviewed in literature.[36,37] Carbon-based nanomaterials (single-wall or multi-wall nanotubes, graphene sheets, etc.) have become commercially available and less costly throughout the last decades, and exhibit high thermal and chemical stability, responsiveness to magnetic fields and high electrical conductivity. Different preparation methods have been studied, from one-pot mixing of the LCE mixture with the nanomaterials, followed by alignment and polymerization, to the inclusion of the nanomaterial guest by swelling into a preformed polymer. The effect of the inclusion of carbon-based nanomaterials is beneficial to LCE electrical and thermal conductivity, which would otherwise be low, and to mechanical properties, since toughening of the polymer was reported upon

inclusion of carbon-based nanomaterials. Plus, carbon nanomaterials readily convert visible/near-IR light into heat, providing local heating to the LCE and thus triggering thermal NI transition. Metal-nanoparticle-LCE composites have also been reported. Various works on the exploitation of the surface plasmon resonance of gold nanoparticles, in particular, have been disclosed, with actuation wavelengths ranging from 600 nm to near-infrared light used to excite two-photon absorption in such systems. It is worthy to remark that the use of near-infrared light and two-photon absorption processes allows a more effective irradiation of the entire specimen compared to the use of visible-light-responsive chromophores, since scattering is highly reduced in the near-infrared spectral window.

Another strategy to allow photosensitivity in LCEs is the inclusion of organic chromophores inside the polymer network. Different photochromic groups have been embedded in LCE matrices, with response to light translating into light-induced heating or isomerization.[38]

In the latter case, the change in the molecular shape is accompanied by a change in steric hindrance, polarity or molecular symmetry of the chromophore, among other properties. This process, in non-crosslinked systems (such as low-molecular-weight LC mixtures doped with a dye), disturbs LC ordering and triggers LC-to-isotropic transition isothermally, driving the macroscopic shape change described previously. This mechanism was also studied in LCEs; scientific literature on this matter is excellently reviewed, and examples of LCEs doped with diarylethenes, fulgides, or menthanes (among others) have been studied throughout the years.[9,39] Each type of moiety enables a particular photomechanical process, which can be exploited to actuate polymeric LC networks.

Azobenzene-based dyes, among the other types of photochromic molecules, have been by far the most studied ones in LCE systems. Legge and Mitchell, in 1991, studied the isothermal NI transition of dye-doped nematic liquid crystals; in their work, they show how doping 5CB with an azobenzene derivative causes an isothermal change in LC order parameter upon irradiation with UV light.[40] These results were further supported by later works that show how disorder is induced in azobenzene-doped nematic liquid crystals

with subsequent modulation of refractive index upon irradiation.[41,42] Li *et al.* demonstrated the photochemical NI transition in a polysiloxane SC-LCE in 2000 (Figure 1.8).[43]

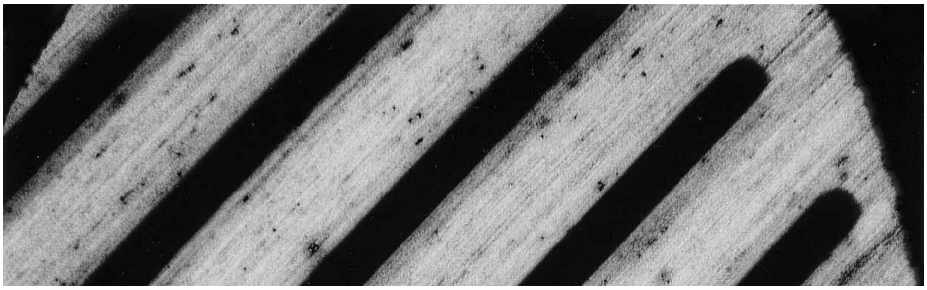

Figure 1.8: POM image of an azobenzene-doped on a PI-coated substrate covered by a mask, after UV stimulation (365nm). The irradiated parts (black stripes) are isotropic, and the masked parts remain in the nematic phase in planar alignment. The image is reproduced from ref. 43.

A seminal research on uniaxial contraction of dye-doped LCEs was disclosed by Finkelmann *et al*. in 2001, who obtained up-to-20% length reduction upon UV stimulation (>30 min).[44]

Azobenzene, the common name of the derivatives of E/Z-diphenyldiazene, and its derivatives are widely used as a photo-responsive substance, since their optical response is easy to tune. Being a diazene, it is characterized by the presence of a *N*=*N* double bond within its structure. The two conformational isomers show two absorption bands within their UV-Vis spectra, which are well separated: in bare azobenzene, *trans*-to-*cis* isomerization occurs via irradiation with an ultraviolet source, while the inverse process is triggered with visible-light stimulation or heat (Scheme 5).

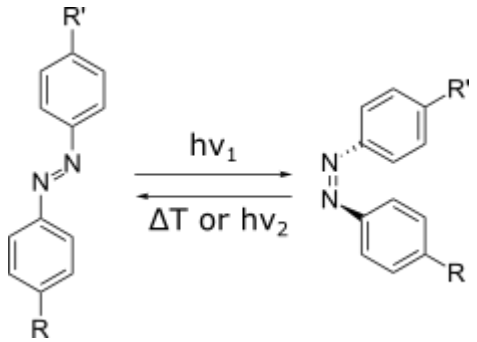

Scheme 5: Photoisomerization of azobenzene. The trans *isomer is planar, with no net dipole, 9.0 Å long; the* cis *isomer is kinked, with a dipole of 3.0 D and 5.5 Å long.*

The two isomers possess different physical and chemical properties, such as refractive index, dielectric constant, molecular symmetry and absorption spectrum (Figure 1.9).[45,46] *Trans*-azobenzene, or (E)-azobenzene, absorption spectrum displays an intense band centered at 320 nm, and a weaker band in the visible range at 450 nm. The two bands are related, respectively, to the π-π^* symmetry-allowed transition and to the symmetry-prohibited n-π^* one. It is a planar molecule with C_2 symmetry. *Cis*-azobezene, or (Z)-azobenzene, has strong absorption in the UV at 250 nm, and a weaker band in the visible region at 440 nm. Similarly, in *trans*-azobenzene the two bands correspond to π-π^* and n-π^* transitions, the former being symmetry-allowed and the latter the symmetry-prohibited. Gas phase experiments suggest that, in vapor phase, phenyl rings are twisted of about 30°; *cis*-azobenzene shows C_{2h} symmetry. Emission has a low quantum yield in azobenzenes, because of the competition between this process and photoisomerization; the latter is more efficient than the former.

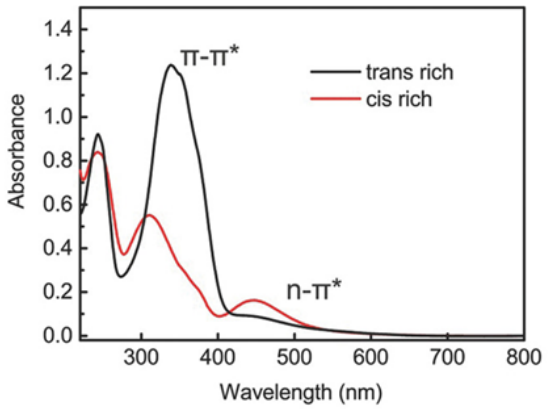

Figure 1.9: Absorption spectrum of a typical azobenzene dye, reproduced from ref. 47.

Trans-azobenzene has a rod-like shape, and stabilizes LC order; *cis*-azobenzene, instead, disturbs LC order, as previously mentioned. Chemical modification of the substituents on the aromatic ring in azobenzene-derived compounds is a straightforward method to change photoisomerization wavelengths. The presence of either electron-withdrawing or electron-acceptor groups changes the energy gap between ground and excited states; thus, the light wavelength to which the compound is responsive is modified.

Besides bare azobenzenes, three main classes of azobenzene-based dyes can be distinguished, according to the nature of the substituents on the ring and spectroscopic features:[47,48]

- Amino-azobenzenes, in which an amine-derived group acts as an electron-donating substituent;
- *Push-and-pull* azobenzenes, or p-donor-p'-acceptor azobenzenes/pseudostilbenes, which possess an electron-donating group and an electron-withdrawing group on both sides of the rings;
- Sterically-hindered azobenzenes, such as *tetra-ortho*-substituted systems.

In the first ones, the lifetime of the *cis* isomer decreases, and the two absorption bands in the spectrum partially overlap. In the second kind of azobenzene dyes, the overlap between the two bands is complete, and forward and backwards isomerization are triggered with the same light. The third class of azobenzenes has an extremely slow backwards isomerization, and thus *cis* isomer possesses an extremely long lifetime, compared to the other two classes.

Since the response time of the materials we studied in this research work is crucial towards the application we designed, we used azobenzene-based dyes that pertain to the first two classes.

1.4. Stimuli-responsive materials and shape-changing materials for biomedical applications in tissue engineering and as artificial muscles

Biomaterials science is one of the youngest sons of materials science and engineering; since the first examples of biomaterials in the 1950s, this field has kept growing up with the objective of providing physicians, surgeons and professionals in medicine not only with new instruments and solutions to diseases, but also with new strategies to understand the interactions between human physiological environment and nonviable synthetic materials. The term *biomaterial* gained an accurate definition in 1987, after the

Conference of the European Society for Biomaterials, when D. F. Williams defined it as:[49]

"*a nonviable material used in a medical device,*
intended to interact with biological systems".

The first meeting of the Society for Biomaterials dates back to 1975, even if the nascent society had already been meeting for six years at Clemson University (South Carolina, USA) to discuss the emerging tendencies in materials science and engineering for biomedical purposes.[50]

Among the widespread range of interests in biomaterials science, one of the newest directions (mid-1980s - present) for research is *tissue engineering*, whose promises of facile preparation of tissue replacements are leading the way to regenerative therapeutics for a wide range of pathologies. Apart from tissue reconstruction, its aims also include a complete understanding of the mechanisms underlying cell growth outside the biological environment, disease modeling and drug testing (as an alternative to animal testing, which poses ethical issues). In this sense, biomaterials must provide the right environment for tissues to fully develop to a mature system that ideally preserves all the features, functionality and properties possessed by their *in vivo* analogue.

Another important subject that has emerged in biomaterials science is the investigation of the possibilities offered using programmable, interactive-surfaced or shape-changing materials. These materials can respond to external stimuli, rearranging their macroscopic shape or showing a transition between two different surface topographies. First applications in dentistry of shape-memory alloys (SMAs) jump back to 1975, while shape-memory polymers (SMPs) became commercially available in the mid-1990s. These materials are attractive for biomedical purposes, since their shape-changing properties find a plethora of applications in the creation of low-weight instruments, surgical aids, actuators, replacements and cell scaffolds.[51,52]

In this sense, LCEs can be regarded as the new entry in the field of shape-changing materials; their potential in this field has been unveiled since the second half of 2010s,

and biomedical applications of LCE-based actuators are envisaged and are the subject of current discussion and research.[53]

2. Use of materials based on Liquid Crystalline Elastomers as Artificial Muscles to assist cardiac contraction

2.1. Introduction and aim of the research

Heart disease is the first cause of death all over the world, according to the World Health Organization; it accounts for 16% of total number of deaths yearly, and of one in five deaths in Europe and North America according to the United States Centre for Disease Control.[54,55] The reduction of the deaths caused by non-communicable diseases (NCDs), of which cardiovascular ones accounted for 37.4% of the total amount in 2012, is one of the objectives of the United Nations Agenda 2030 in the frame of Goal 3 of the 17 Sustainable Development Goals, whose achievement is pursued by all the member States. [56–58]

The term *heart disease*, though, refers to a wide category of pathologies, among which heart failure (HF) and myocardial infarction (MI). These two pathological conditions were the main targets of this study; the objective of this research was the design of a device to assist heart contraction and a cardiac patch for scar tissue treatment after MI, overcoming the disadvantages of the currently marketed devices used in the treatment of both aforementioned pathological conditions. HF is a progressive disease, caused by the inability of the heart to pump the necessary amount of blood in the body. Its mortality rate reaches 25% to 50% in 5 years after diagnosis.[59] This disease leads, in the majority of the cases, to the need for a cardiac transplantation; however, the shortage of heart donors and the possible complications of such a surgical intervention pose a limitation in the number of HF cases that can be treated this way. Pharmacological treatment proved to be beneficial in the short term and to mitigate the symptoms associated with HF, but its effectiveness decreases in the long run. Thus, the need for circulatory and assist devices is of medical relevance, and through the last 50 years a considerable effort has been made to design new types of cardiac assist devices (CADs, Figure 2.1a) to help the impaired heart pumping blood efficiently. First attempts focused on the realization

of total artificial hearts; however, due to the high fatality risk to implant a total heart replacement, focus shifted to single-ventricular pumps, or ventricular assist devices (VADs). Despite major advances in the field, VADs are still bridge therapies in most cases.

The number of patients that recover heart function during treatment with a VAD is, indeed, too low to consider the implantation of a VAD a destination therapy; a VAD is mostly used, then, either as a bridge-to-device or as a bridge-to-transplant treatment. In the former case, a short-lifetime VAD is implanted in view of its later substitution with a longer-lifetime device; in the latter, a VAD is implanted to stabilize a patient waiting to undergo heart transplantation.

Various complications can arise after implantation. Even though the latest developed VADs are not as heavyweight and large in size as their predecessors, they still need to be actuated by an external power source. This is the major downside of this treatment, since driveline infections, thromboses and gastrointestinal bleeding account for 47% of hospital readmission after VAD implantation.[60] Moreover, clot formation can also occur in other components of the device in contact with bloodstream; pump thrombosis has a yearly incidence of 10%. Antithrombogenic therapies must be administered to patients with a VAD.

Research goes in the direction of lowering the number of these adverse events, and untethered power supply systems are being studied; muscle-powered actuation by means of a muscle energy converter could also be a feasible way to design a battery-free VAD. Moreover, surfaces in contact with bloodstream have been scaled down through the decades, to reduce the insurgence of thromboses. The design of direct compression heart sleeves (DCCSs, Figure 2.1b) goes in the direction of scaling down surfaces in contact with bloodstream, delivering pressure in the systole phase (*copulsation*) and thus enhancing heart ejection fraction.[60]

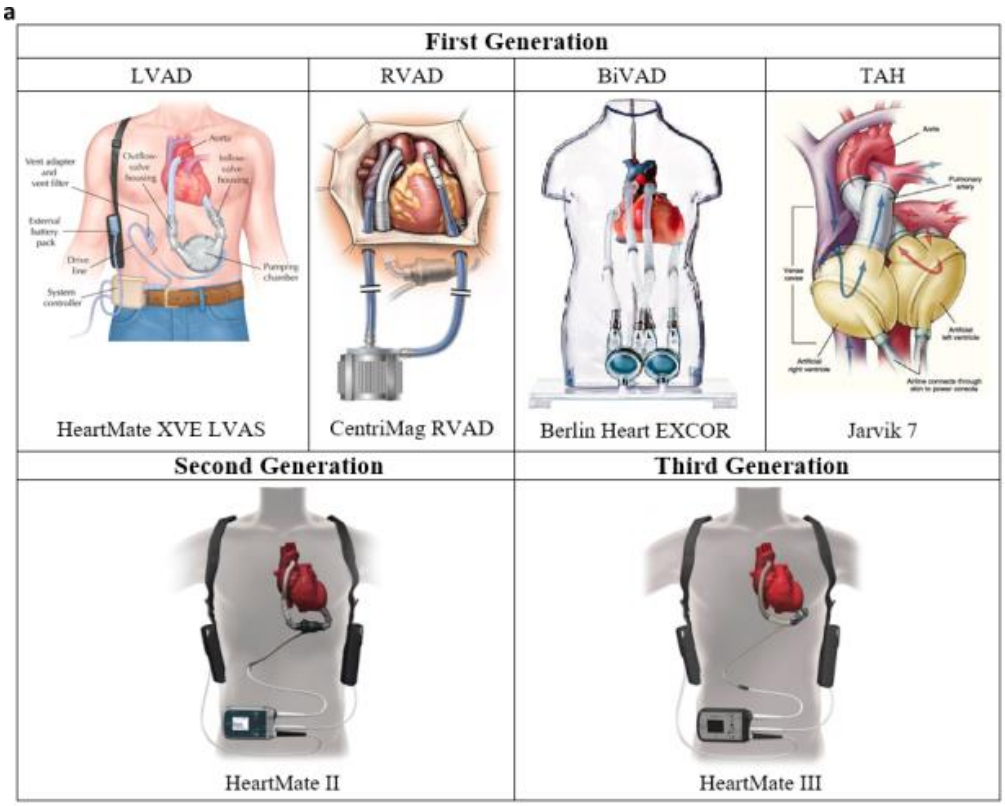

Figure 2.1: Overview of cardiac CADs and their evolution. (a): Examples of devices from the first (top), second and third generation (bottom) of CADs. From left to right: left-ventricular assist device (LVAD), right-ventricular assist device (RVAD), biventricular assist device (BiVAD) and total artificial heart (TAH). First-generation devices relied on pulsatile flow pumps to work, and were heavyweight, noisy, and large in size, causing malfunctions and affected by a high morbidity rate. Second-generation devices were actuated by continuous flow pumps, whose power was supplied by an external driveline, and were smaller than first-generation devices. Third-generation CADs constituted a further improvement in CADs in terms of size and weight. They are based on a centrifugal pump, actuated by magnetic or hydrodynamic levitation. Almost

99% of LVADs, nowadays, use this technology. (b): Examples of direct cardiac compression sleeve (DCCS). These devices, with various designs and working principles, have the task to apply direct pressure on the heart epicardial surface, thus enhancing the ejection fraction of a failing heart. From left to right: two types of DCCSs using a pneumatic air-driven McKibben-type actuator to compress the heart (A-B), a muscle-powered DCCS (B), an extra-aortic balloon pump that compresses the walls of the ascending aorta (D). The image is reproduced from ref. 60.

MI is the sudden stop of blood flow to a part of the heart, accompanied by damage to the heart tissue and necrosis; HF can be a consequence of a MI.

Besides impairment of blood pumping, heart tissue can undergo necrosis, as mentioned, or remodeling after an adverse event; when it happens, its regeneration capacity is limited. Thus, an external intervention is most likely needed to replace the scar tissue or the impaired part, which is unable to contract and whose normal functioning is compromised. Among the current treatments for HF and MI, none stimulates regeneration of tissue. Thus, the lack of an alternative to heart transplantation in end-stage patients drives the need for the design of reject-free biomimetic cardiac patches to restore heart tissue. Ideally, a heart patch able to substitute heart tissue effectively has to comply with three requirements:[61]

- Generation of tension, to assist cardiac contraction (20- 50 mN/mm^2);
- Relevant clinical thickness, in the order of 1 cm;
- Propagation of electrical pulses (with 25 cm/s velocity).

Throughout the last 30 years, the main approach that has been followed by tissue engineers is the preparation of engineered heart tissues (EHTs), using a wide range of scaffolds populated by, amongst others, hiPSC-CMs, skeletal muscle fibroblasts, primary CMs. This pathway, though promising, is still far from being a clinical reality: EHTs suffer from different drawbacks, from low engraftment rate, in case of direct cell injection, to concerns about the insurgence of arrhythmias after implantation, because of the mismatch between the electrical conductivities of the graft and the native tissue. The use of synthetic materials could also be a feasible pathway to fabricate cardiac patches; however, currently used materials, even though promising in supporting propagation of electrical pulses or in hosting cardiac cells and directing their alignment, do not offer any or sufficient assistance to contraction.[62]

In this sense, the use of biocompatible shape-changing/shape-memory materials, capable of supporting propagation of electrical pulses and directing alignment of cardiac cells, is highly desirable to fabricate low-weight devices for cardiac contraction assistance and implantable patches for scar tissue replacement. This class of smart materials, able to change shape upon stimulation and generate force behaving as artificial muscles, has been studied for half a century in different fields of biomedical engineering (to manufacture bone replacements, implants, surgical devices), and could be the breakthrough to design the next generation of cardiac implants and devices able to overcome the issue presented by currently marketed devices.

2.2. Shape-changing and shape-memory materials in the biomedical field

Shape-changing materials (SCMs) and shape-memory materials (SMMs) are a set of materials, among the wider category of smart materials, that have emerged in biomedical research because of their unique properties to switch from one shape to another upon stimulation. This introduction will pinpoint the latest advances in this direction and will provide a comparison among the main different systems that have been studied so far, highlighting their upsides and downsides. The possibilities enabled by LCEs are discussed, with a resume of the recent results and a comparison between their performances and those shown by other shape-changing systems in the biomedical field. Three parameters are taken into account in this Thesis work to compare the different materials used to fabricate soft actuators: work density, output strain and efficiency.[63] The first is the output work generated by the actuator normalized by its volume (in J/m^3); the second is the percentage change in length (or a characteristic dimension) of the actuator, normalized by the initial value; the last is the percentage of input energy converted into output work for each of the considered systems.

2.2.1 Shape-memory alloys (SMAs)

The first evidence of shape-memory effect (SME) in metal materials was reported for Au-Cd and Cu-Zn alloys.[64]

This brief introduction will focus on Ni-Ti alloys, since they represent the most performing and most used alloys for biomedical engineering, due to their biocompatibility and lower elastic modulus compared to their main competitors; moreover, besides being widely used, Ni-Ti alloys possess all the features that define the broader category of SMAs and represent a good example to discuss their properties.

From a metallurgical perspective, the working principle of SMAs relies on the *martensite*-to-*austenite* phase transition in metals (Figure 2.2a). Austenite is the high temperature phase and adopts cubic crystal structure; martensite is generated at low temperatures, and exists in two structures with monoclinic lattice, *twinned* and *detwinned* martensite. On cooling, austenite transforms into a twinned martensite phase; at low temperature, this form can be deformed to the detwinned state: now detwinned martensite can revert to its original shape by simple heating. This phenomenon is called one-way shape-memory effect (OW SME), and occurs without exerting force on the metal, but relying on its crystal structure transition only. Thus, the specimen is formed in the austenite phase, then cooled down to twinned martensite, deformed in order to reach detwinned martensite structure; application of heating causes irreversible shape change to the original one. Two-way SME (TW SME), on the other hand, allows reversible switching between two shapes: the material changes from an original shape to another one on heating, and returns to the first one on cooling. This is made possible by *training* the material; repeatedly straining the specimen in its twinned martensite phase, indeed, causes the material to detwin and to store some defects in the microscopic structure of the material. Then, the material can go from this shape to the one it had in its austenite phase on heating, and revert to the one to which it was trained, in detwinned martensite, on cooling. TW SME is less used than OW SME because of the difficulties posed by the training process, but allows a more tunable behavior of the SMA.[64,65]

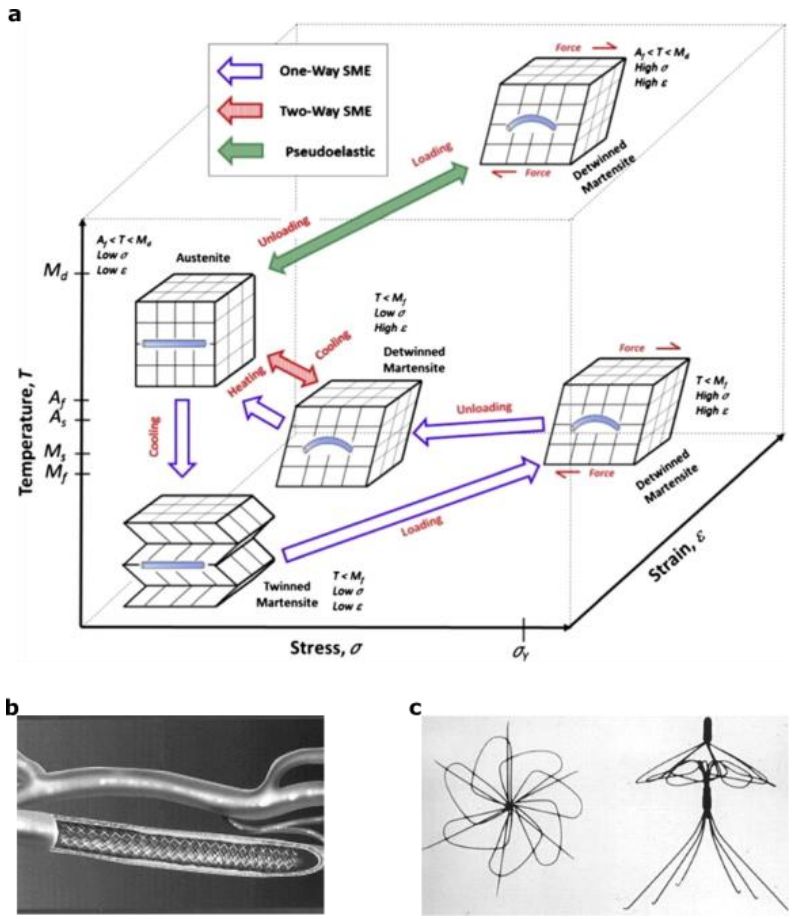

Figure 2.2: Working principle of SMAs and some application of Nitinol. (a): Crystalline structures and properties of Nitinol. OW SME relies on the transformation of detwinned martensite to austenite upon heating. TW SME becomes effective after specimen training, during which the sample stores some unrecoverable stress, and can undergo reversible shape change upon heating and cooling from martensite to austenite and vice versa. Superelasticity is the isothermal recovery of the shape of the sample when shaped in austenite form after martensite form is induced only via stress loading of the material. (b): Cardiovascular stent inserted in the carotid artery. The specimen is formed in cylindrical shape and compressed prior to surgical intervention. It is then introduced into the body at low temperature, cooling under flow of saline solution; when flow stops, physiological temperature triggers the comeback to the initial shape. (c): Simon filter to prevent blood clots. It relies on the same principle as the cardiovascular stent; when the filter gains its original shape upon heating provided by the physiological environment, the filter can trap and dissolve clots to prevent embolisms. Images are taken from ref. 65 *and* 66.

These properties have been exploited in the manufacturing of low-weight instruments, and many examples can be found in literature; the most important ones pertain to the

dental healthcare field and to orthopedic and cardiovascular surgery. Focusing on Nitinol, its alloys with various Ni-Ti ratios have been widely used since some of them have transition temperatures near the physiological value (37°C).

OW SME has found application in cardiovascular instrumentation manufacturing (Figure 2.2b-c).[65,66] The first device made of SMA wires was the Simon filter for prevention of pulmonary embolism. It traps blood clots in order for bloodstream to dissolve them, and it is useful for people unable to use anticoagulant drugs. The original shape of the filter is deformed and inserted inside the body through a catheter and kept at lower-than-physiological temperature during the surgical operation. Once it is released the bloodstream heats it up, making it spring back to the former shape. Self-expanding stents are another important cardiovascular application of SMAs. These medical devices are cylinders that are needed, in some cases, to maintain vessel diameter. In the specific case of SMAs, the scaffold is formed in the cylindrical shape, then compressed and placed in the vessel to be stented. Physiological body temperature triggers reverse transition to the original shape.

TW SME is more difficult to be used for biomedical applications, but it is used in actuator manufacturing.

2.2.2 Shape-memory polymers (SMPs)

Polymers that exhibit SME generally possess, from a molecular point of view, two segments within their macromolecular architecture: one is highly elastic, while the other is capable of decreasing its stiffness upon stimulation. SME arises from the dual nature of the structure and is enabled by the thermomechanical cycle that makes the network store a certain shape.

This cycle comprises four steps (Figure 2.3a): first, the polymer is heated up above its transition temperature, T_{trans}; then, the specimen is deformed to the desired shape by applying an external force. After that, it is cooled down below T_{trans}, and the constraint is removed to store the temporary shape. Heating the sample above the transition temperature triggers shape recovery to the original one. The two segments are linked

through either physical or chemical crosslinks, and this difference accounts for the type of transition that triggers SME.

The transition could be a glassy-to-amorphous transition (in this case $T_{trans}= T_g$, where T_g is glassy transition temperature of the SMP), or the melting of either the hard segment of a semi-crystalline polymer or the crosslinks between them (and thus in this case $T_{trans}= T_m$).[67] SMPs can exhibit both OW SME and TW SME.

As for SMAs, the most investigated SMPs are the ones whose transition temperature is in a range near body temperature (37°C); OW SME is mostly used. Figure 2.3b-c shows some applications of SMP in the biomedical field.[52,66]

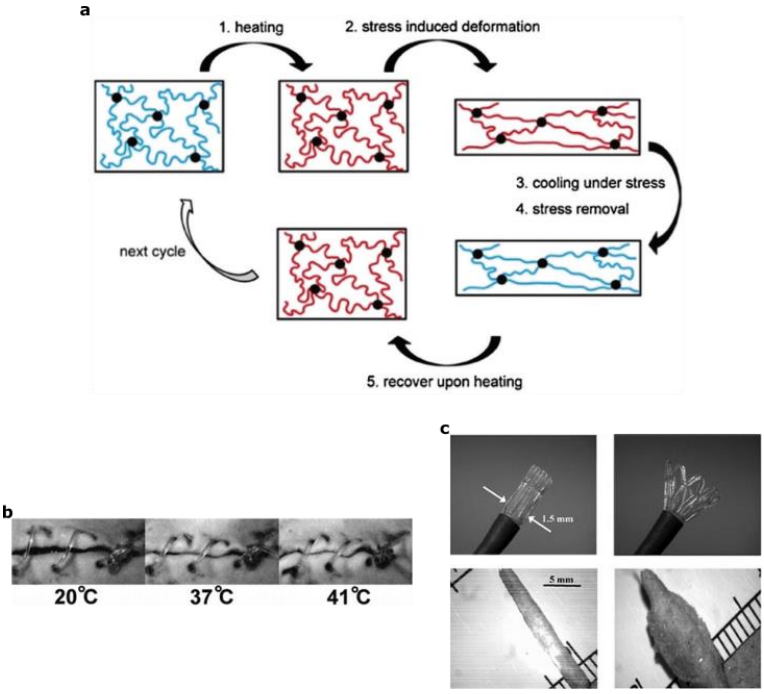

Figure 2.3: Working principle of SMPs and some applications in the biomedical field. (a): Shape fixation. The polymer is heated above the transition temperature, T_g or T_m according to the mechanism that triggers SME, deformed, and cooled down. Subsequent re-heating triggers OW SME. (b): Close-up of the evolution of a self-knotting suture upon heating. (c): An endovascular thrombectomy device for stroke treatment (top) and an SMP-based expandable foam for aneurysm bypass (bottom). Images are reproduced from ref. 66 *and* 68.

Suturing is always a concern in surgical operations; tissue strands must not be bonded too tightly, since the application of a consistent amount of force can lead to necrosis,

while a slack suture can have as a consequence the formation of scar tissue. Polyester-based SMPs have been used as smart resorbable sutures, due to their biodegradability and the possibility to self-knot on heating, exploiting SME. OW SME has been also exploited for the treatment of maxillofacial defects: Zhang *et al.* developed a poly-caprolactone foam that can be deformed by manual pressure on heating above 55°C and inserted into a bone defect. After the stress is released, the foam expands and fits to the defect; on cooling, the final shape is locked. A self-expandable poly-urethane foam has been investigated for cardiovascular surgery in the treatment of aneurysms: the polymer, exhibiting SME, is inserted inside the bulge in its compressed state at low temperature. On heating, the foam expands, and blood flow bypasses the aneurysm. The use of smart polymers has the advantage of providing the surgeon with a soft biocompatible system, mechanically different from the currently used platinum coils that can be rejected by the patient or generate allergic reactions.

2.2.3 Other examples of shape-changing systems

Even though SMAs and SMPs have dominated the market of shape-changing materials in the biomedical field, other types of smart systems are now being studied as artificial muscles and as soft actuators.[63]

The principle underlying current pneumatic actuators has its roots in the idea by J. L. McKibben to use them in artificial limbs. Pneumatic muscles, in general, generate work through the movement guaranteed by the inflation with a gas of a thin expandable membrane made of braided fibers, that swells in the radial direction while shortening in length. Even though they exhibit work densities in the order of 1000 kJ/m^3, their main limitation is in the impossibility to miniaturize such systems, that rely on the presence of a fluid tank to work.[63]

Braided and coiled fibers of highly oriented polymers also have been studied to develop low-weight artificial muscles. Polyethylene and nylon, oriented via uniaxial elongation and used for fishing lines and sewing threads, can contract in the stretching direction up to 2.5%; twisted fibers, on the other hand, can shorten by almost half of their length.[63,69] Even though new fabrication techniques allow the miniaturization of such systems, a

constraint on their performances is posed by the rate of heat transfer during relaxation and actuation, that hinder them to possess a large bandwidth (as the range of frequencies that the artificial muscle bears upon continuous actuation).

In the field of polymer science, a class of materials that is becoming increasingly attractive are electroactive polymers (EAPs). This set of materials comprises different types of polymeric systems, with various characteristics and actuation mechanisms.[70,71] Ion polymer-metal composites (IPMCs) are composed of a ionically conductive membrane that stores the electrolyte, which is interposed between two electron-conducting electrodes. When a potential difference is established, the movement of ions causes the shrinkage of one side of the composites; as a result of stress mismatch, the structure bends: inverting voltage polarity, the bending direction reverses. Chemical stability is the main issue in these systems, which find application overall in wet environments; the emergence of ionic liquids as electrolytes could increase the stability of dry IPMCs, at the expense of an increase in manufacturing costs. Dielectric elastomer actuators (DEAs) are fast responding actuators that produce strains through the application of an electric field. The applied voltage, indeed, creates an attractive force between the electrodes, where a dielectric matrix with high Poisson's ratio, such as silicone-based elastomers, polyurethanes or thermoplastic elastomers, is sandwiched. The thickness of the matrix, thus, increases when the applied field increases, and the elastomer elongates along the two other dimensions. However, the large voltages required for actuation are considered to be unsafe for wearable and biomedical devices, and applications of DEAs are still limited to soft robotics in the field of optics and sensors. Conductive polymers (CPs) can conduct ions or electrons and display volumetric changes upon electrochemical reactions. Their applications in the biomedical field are still limited, though they are being studied as drug delivery systems, micropumps and catheters.

Piezoelectric actuators, as well as magnetostrictive, electrostrictive and inorganic photostrictive ones, still find limited applications in the biomedical field, and exhibit small-amplitude deformations when compared to other types of systems. Another

important class of smart soft materials, stimuli-responsive hydrogels, have mainly found applications as drug delivery systems so far.

2.2.4 The role of LCEs as soft actuators and in biomaterials engineering

In this context, LCEs can be regarded as the new entry in the field of SCMs for biomedical applications. Latest advances in fabrication techniques and latest findings on their role as biocompatible substrates have made them possible competitors for well-established systems such as SMAs and SMPs.

Both SMAs and SMPs can be thermally actuated, but the performances of these two classes of materials are very different. The latter can recover higher deformation compared to the former (up to 800% in the first case, 6-8% in the second) and possess lower densities; in exchange for these characteristics, SMPs are slower than SMAs in shape recovery, and SMPs can generate stresses which are two orders of magnitude lower than the ones exerted by SMAs. However, SMAs have are more expensive than SMPs (450 €/kg vs. 20 €/kg). Fields of application are, thus, different.[72]

LCEs have proved to be a good alternative in the biomedical field to the systems that were described previously, showing comparable properties on stimulation and some upsides. Their biocompatibility and cell-instructiveness were demonstrated on various cell lines.[53,73–77] LCEs do not need any type of hard mechanical pre-programming such as SMAs (the repeated stress application to *train* the specimens) that exhibit TW SME, or mechanical loading as in SMPs, since their deformation is the result of the alignment of mesogens in their microstructure. During the last years, the scientific effort has been focused on overcoming the classical fabrication methods of LCE-based polymer films borrowed by low-molecular-weight LC science, based on the surface effect of aligning substrates covered with surfactants. The shape and alignment, and thus the actuation path, can now be programmed by means of direct ink writing (DIW) 3D printing, exploiting stress-induced alignment of LCEs, or, in the microscale, direct laser writing (DLW) of low-molecular-weight mixtures of reactive mesogens.[26,78] Another feasible patterning method, overall for LCP-based coatings, is soft lithography, that enables

stimuli-dependent morphological changes in active surfaces. DIW and DLW also allow the preparation of complex actuating structures.

Moreover, their hysteresis is very low, and the longevity of dye-doped LCEs has been demonstrated to be more than twenty days under continuous excitation in certain cases.[3] LCEs, being composed of mesogenic substances, are intrinsically thermoresponsive; however, a plethora of actuation stimuli that rely on the modification of the order parameter either thermically or mechanically have been studied. Light stimulation, though, guarantees high accuracy in space and time and untethered actuation.

Work densities of LCEs are also reported in literature.[79–83] This parameter, along with the efficiency and the output strain, is commonly used to compare the performances of actuators, as it was mentioned above.[63] A comparison among different types of soft actuators is drawn in Table 1.

Type of material/ composite	Typical work density (J/m^3)	Maximum output strain	Efficiency	Upsides	Downsides	Applications in the biomedical field	References
Shape-memory alloys	~10^6-10^7	4-8%	10-15%	- High energy density - Low actuation temperature	- Hysteresis - Need for pre-programming - High cost	Surgical tools (catheters, stents, braces), implants	63,72,84–86
Shape-memory polymers and highly oriented polymer fibers	5-6·10^5	From ~50% to 800%	<10%	- Inexpensive - Some of them are biodegradable - Mechanical properties in the range of biological tissues - Lightweight - Wide set of actuation stimuli	- Slow response - Low efficiency	Surgical tools (micropumps, stents, sutures, foams)	70,72,84,85
Liquid Crystalline Elastomers	<3·10^5, ~10^6 in some cases	Up to 100%	<0.1%	- Intrinsic thermal- and electric/magnetic-field responsiveness - No need for mechanical pre-programming of the specimens - High anisotropy	- Low efficiency	Possible candidates as artificial muscles, active cell culture substrates	7,53,72,87

				-	and cell-instructiveness Mechanical, optomechanical, electrical properties are tunable Possible untethered actuation via light stimulation				
Electroactive Polymers	5.5-6·10^3 (IPMCs) 1.5·10^3-10^5 (DEAs and CPS)	0.5-3% (IPMCs) 25-30% (DEAs) 12% (CPs)	From 1.5% (IPMCs) to 60-90% (DEAs)	-	Soft, flexible, low weight	-	High actuation voltage Chemical stability Need for encapsulation	N/A	63,70,72,85,86
Pneumatic artificial muscles	5·10^5-10^6	15-30%	30-40%	- -	Fast working cycle Not expensive	- -	Large size Need for a fuel tank to be actuated	Robotic grippers/arms, artificial limbs, cardiac assist devices	63,85,86

Table 1: Comparison among the most studied materials and composites used to fabricate artificial muscles and actuators in the biomedical field.

LCEs exhibit work densities in the range of 100 to 300 kJ/m^3. These values are in line with what can be observed for SMPs and soft actuators; conversely, human muscles have work density in the hundreds of kJ/m^3 range, while SMAs can display values of up to 1000 kJ/m^3. Higher values are displayed by other kinds of actuators (such as fluid-driven or pneumatic ones), but, as it was mentioned before, they rely on completely different physical principles and lack the low weight of soft materials.[86,88,89] Thus, LCEs have performances that are comparable to SMPs, in terms of actuation strain and work density. Efficiency, however, is a downside of both two of them when compared to other kinds of actuators. Actuation energies can be several orders of magnitudes higher than what is later generated by the soft system, with efficiencies that are lower than 0.01% in most cases. The enhancement of the efficiency of such systems is one of the challenges that were addressed in this research work.

In the frame of heart regenerative medicine, LCEs have the potential to be used as materials for the design of an untethered, low-weight and biocompatible VAD, but also for the preparation of a scaffold material for hiPSC-CMs in the perspective of the design of a cardiac patch (Figure 2.4). In the former case, a feasible possibility for the design of a LCE-based light-driven VAD is the use of a LCE-based film as a direct cardiac compression sleeve (DCCS). The synchronization of the device with a pacemaker would allow paced stimulation of the active material along with the heartbeat.

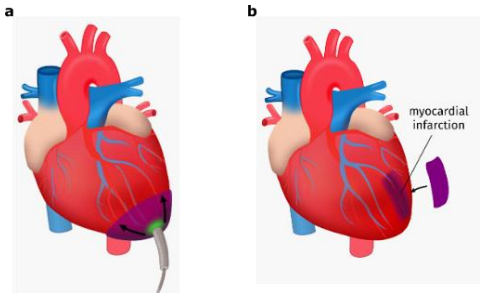

Figure 2.4: Tentative design of LCE-based cardiac implants and devices. (a): Light-stimulated DCCS to assist heart contraction in HF. (b): Stimulable patch for scar tissue regeneration after necrosis induced by MI. Images are a kind courtesy of dr. C. Ferrantini.

Besides the design of a VAD, LCEs are suitable for the design of a stimulable cardiac patch. Their responsiveness allows the possibility to contract and generate force upon stimulation, and their mechanical properties can be easily tuned to obtain the desired

response time and amount of generated force upon stimulation. Electrical stimulation, even though possible, is slow in LCEs compared to light stimulation. However, some examples of LCNs doped with carbon nanotubes (CNTs) are reported in literature; in these composites, electrical conductivity can be tuned upon variation of CNT content in the mixture.[75]

Thus, this particular class of materials allows tunability of all the features that were mentioned above to comply with the requirements for the development of an effective and implantable cardiac patch.

2.2.5 Use of a light-responsive LCE-based material to assist muscle contraction

Previous results published by our research group, in collaboration with the Division of Physiology at the Department of Experimental and Clinical Medicine at the Università degli Studi di Firenze and the National Institute of Optics at the Italian Research Council, demonstrated that a patch of a LCE material is suitable to assist muscle contraction.[3]

In the seminal article by Ferrantini *et al*., a proof-of-concept experiment to demonstrate the ability of LCEs to assist muscle contraction was carried out by coupling a rat heart trabecula to a strip of a LCE photosensitive material with the same dimensions as the muscle. Simultaneous stimulation of the LCE and the murine muscle resulted in an enhancement of the force that was developed by the rat heart muscle under electrical stimulation.

A typical LCE mixture contains a mesogenic monomer, a polyfunctional crosslinker (either liquid crystalline or not) and an initiator to start the polymerization reaction. A dye can be inserted to enable photoresponsiveness of the network. In the case of the materials used throughout the reference study, the compositions contained two commercially available reactive mesogens, an azobenzene derivative equipped with an acrylate group and a UV-responsive photoinitiator.

The most important metric that, in the study presented here and in the further developments, described the performances of the materials is *active* tension (measured as a force normalized on sample transversal cross-section, mN/mm^2), which is the tension generated by the material upon stimulation; this parameter is well established in

the context of muscle biomechanics to characterize muscle contraction.[90] Studies on kinetics of force generation take into account the half of the time in which the strip reaches the maximum value in the diagram of force to stimulation time at a given light intensity and irradiation time (50% activation, RT_{50}) and half of the relaxation time of the strip to initial tension value (50% relaxation).

Passive tension, which is linked to the rigidity of the material, constituted another important physical quantity that characterized the materials in the first screening phase. It was measured as the tension exerted by the sample undergoing stepwise stretching and relaxation along the alignment direction, as reported in the work by Ferrantini *et al*.[3] The goal was to keep this parameter the lowest possible, not to influence the properties of the native muscle to be assisted.

Among the different LCE-based materials whose active and passive properties were characterized to find a good candidate for assisting muscle contraction in a first screening phase, the reference light-responsive material contains 10% mol/mol of crosslinker **CL1**, 88% mol/mol of monomer **M1**, 1% mol/mol of dye **D1** and 1% mol/mol photoinitiator **IN1**. The dye used to dope the material has a maximum of absorption in the green-light region of the visible spectrum. This LCE-based material proved to be the best compromise in terms of force generation kinetics and active tension generated upon stimulation and low passive tension. The mixture is designated as **LCE1** (Figure 2.5) and constitutes the reference for all further studies.[3]

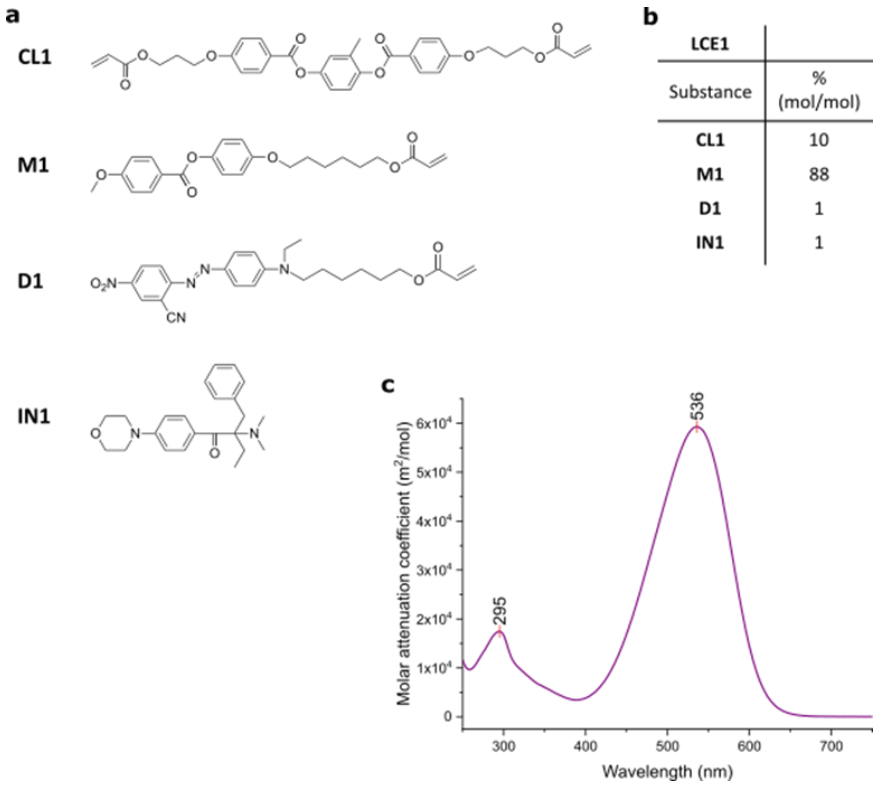

Figure 2.5: LCE mixture used in the work by Ferrantini et al. *to demonstrate the ability of dye-doped LCEs in assisting cardiac contraction.*[3] *(a): Chemical structures of LC monomers (diacrylate **CL1** and monoacrylate **M1**), dye (**D1**) and photoinitiator (**IN1**). (b): Chemical composition of the light-responsive LCE-based material that was prepared and characterized for its use in view to assist muscle contraction. (c): UV-Visible absorption spectra of dye **D1,** which has an absorption peak centered in the green region of the visible spectrum.*

In the course of the first experiments to assess the possibility to use LCE-based materials as artificial muscles, a laser source was used to excite dye **D1**, contained in **LCE1** mixture, providing a strong collimated illumination of the strip in air at room temperature confined in its central zone (Figure 2.6a). Under these conditions, with an excitation power of 100 mW/mm^2, **LCE1** was capable of developing an active tension of 387±45 mN/mm^2, which is a value almost four times higher than human atrial and ventricular myofibrils and in the order of the active tension developed by rabbit skeletal muscle myofibrils.[91,92] Active tension was measured using a setup in which the strip of the LCE material contracted in isometric conditions, clamped at both sides.

To assess the longevity of the material under confined illumination conditions, a strip was irradiated at 1 Hz frequency with the source switched ON for 250 ms and OFF for 750 ms at a constant intensity of 25 mW/mm^2 for 30 days (Figure 2.6b). This experiment demonstrated that the decay in active tension experienced by the samples after 20 days of continuous stimulation (68% decrease) is mainly due to photobleaching of the dye. Indeed, the maximum active tension value of ≈90 mW/mm^2 developed on day 0 could be generated again, at the last time point of the experiment, only if activation power was increased. Plus, irradiation of a neighboring part of the strip with respect to the one used for the lifetime assessment of the material for 30 days resulted in a re-enhancement of the active tension developed on stimulation, confirming the hypothesis of photobleaching of the dye in the irradiated zone as the main phenomenon that causes the decrease of performances of the material.

Thus, not to cause dye photobleaching and to exploit the entire length of the sample, a different illumination setup comprising a LED lamp was used, keeping the strip in a water environment under laminar flow to keep its temperature constant. In this case, though less powerful than the laser, the illumination beam was chosen to be at least as wide as strip length. In these conditions, the reference material **LCE1** was capable of generating up to 70 mN/mm^2 under irradiation with green light at 532 nm at 1.5 mW/mm^2 power, reaching the half of this value in 20 ms approximately (Figure 2.6c-d). Active tension remained constant throughout the whole duration of the experiment, not showing any run-down from the reference value after 20 days. Temperature was kept constant at 25°C by means of a water perfusion system with laminar flow. Increasing light intensity in the range 0-1.5 mW/mm^2 resulted in increasingly higher tension developed under stimulation, in a nonlinear fashion, and in faster response time in activation; relaxation time of the strip was unaffected by the increase in light power provided.

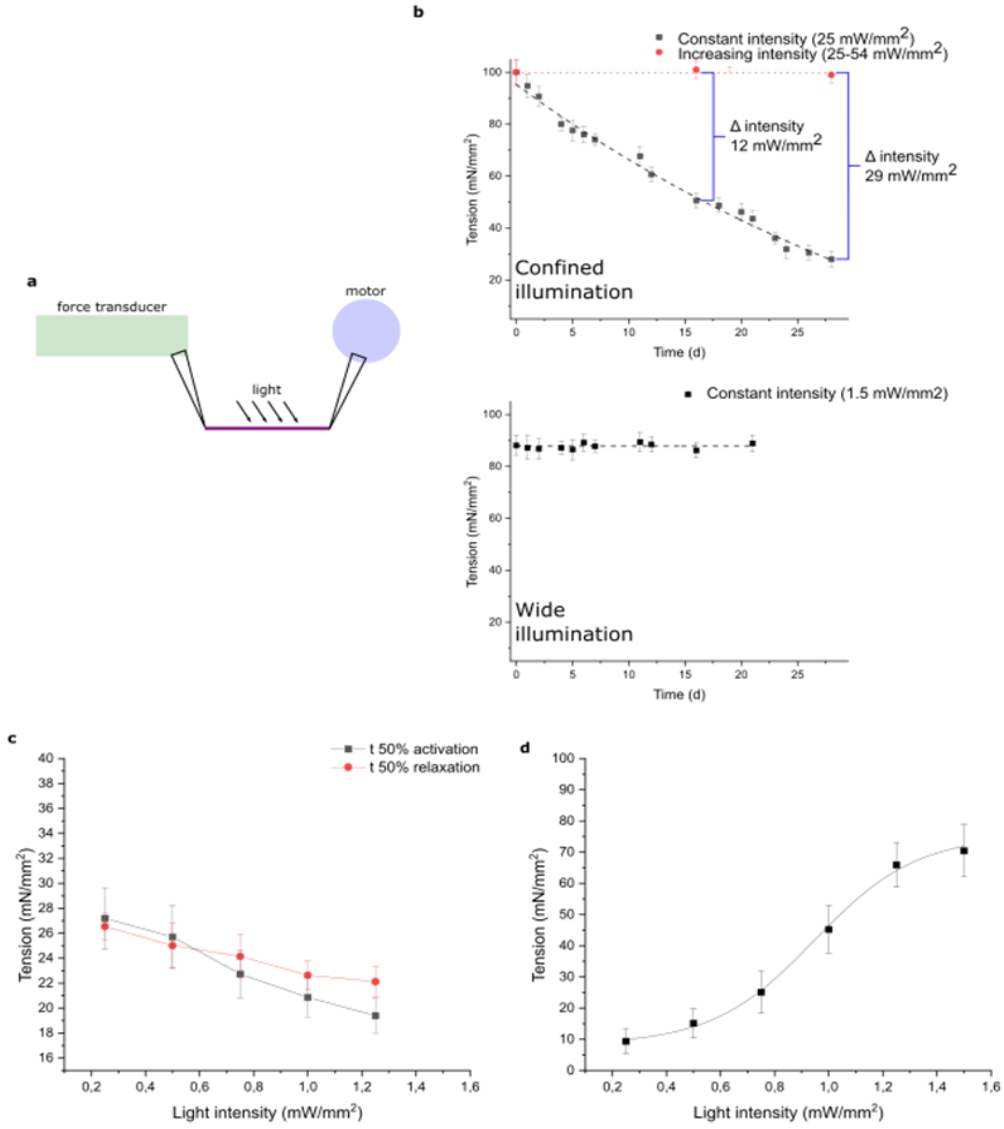

Figure 2.6: Modulation of active tension developed by a strip of ***LCE1*** *under green light stimulation, provided by either a LED lamp (wide illumination) or a green laser (confined illumination). (a): Setup used for strip mechanical characterization. The strip was mounted to contract isometrically clamped between a motor, to set strip length, and a force transducer, to measure the force exerted by the specimen upon stimulation. Light was provided to the strip illuminating from the top, both in the case of laser activation (in air and confined in strip central zone) and in the case of LED lamp activation (in water and with the beam as wide as the strip length). (b): On the top, demonstration of dye photobleaching after 30 days of continuous (1 Hz, tOFF=750 ms, tON=250 ms) irradiation at 25 mW/mm² in the central zone, using a green laser. On the bottom, the effect of illumination with a LED lamp at lower intensity for 30 days. (c-d): Modulation of*

active tension and response time as a function of light intensity in wide illumination conditions. The images are adapted from ref. 3.

After the mechanical characterization of **LCE1** mixture was carried out, a proof-of-concept experiment on the possibility to assist cardiac muscle contraction on a murine model was conducted. Intact ventricular trabeculae harvested from mouse hearts were coupled to a strip of **LCE1** material with the same dimension as the muscle, mounted between the same motor and transducer, and electrically stimulated at 1 Hz after they were stabilized in Krebs solution. Results are shown in Figure 2.7.

First, some traces of the muscle without the LCE film assistance, paced at 1 Hz through electrical stimulation provided by electrodes, were recorded. Then, the muscle was coupled to a strip of **LCE1** and the traces of the muscle, electrically stimulated, coupled to the unstimulated LCE, were recorded. It can be observed how the presence of the LCE strip does not affect muscle functionality: active tension level upon electrical stimulation remains the same with and without the unstimulated LCE coupled to the muscle, suggesting no effect of LCE passive properties on the muscle. After that, both the muscle and the LCE were simultaneously stimulated: the former through electrical pacing, the latter via illumination with a LED lamp (1.5 mW/mm^2, wide illumination, in Krebs solution environment at 25°C). The amount of active tension generated by the LCE-muscle bundle was the sum of the tensions developed by the muscle and the LCE alone, suggesting that the activation and relaxation times of the LCE strip were fast enough not to damp the muscle. The same level of initial active tension upon electrical stimulation was re-gained when the LCE was switched off and the muscle was allowed to contract upon electrical stimulation.

Thus, when both the LCE strip and the muscle were allowed to contract, it resulted in an enhancement of the active tension developed by the LCE-muscle system, with no effect on the passive properties of the muscle due to the presence of the LCE and on the kinetics of force development. The tension developed was found to be dependent on material thickness.

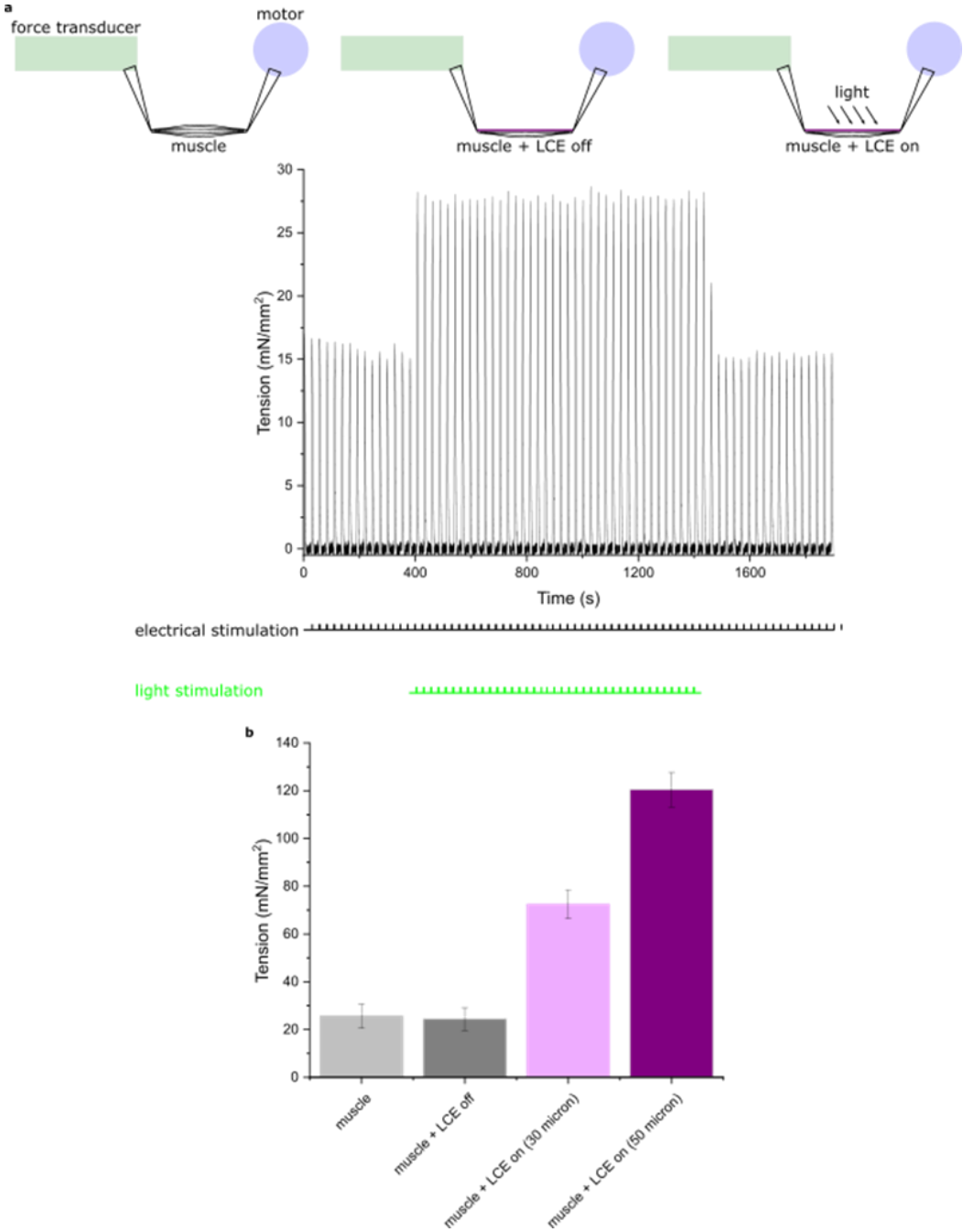

Figure 2.7: Proof-of-concept experiment on the possibility to assist cardiac contraction on a murine model. Left: on the top, setup of the experiment. A ventricular mouse heart trabecula was harvested, mounted between a motor and a transducer and coupled to a strip of ***LCE1*** *with the same dimensions. Right: effect of film thickness on force development enhancement. Images are adapted from ref.* 3.

These early results on the characterization of LCE-based materials towards the preparation of a material capable of assisting muscle contraction demonstrated how the reference material, **LCE1**, is suitable for this purpose, showing good results from the point of view of force development kinetics, modulation of activation time and active tension developed upon increasing light intensity, possibility to cooperate with a native muscle to enhance its performance.

2.3. Results and discussion

Further studies, which are the subject of this Thesis work, aimed at increasing the efficiency of the "state-of-the-art" material **LCE1** and improving its force generation kinetics.

To achieve this objective, a two-pronged strategy was followed, both modifying the composition of the material and acting on illumination system and excitation wavelength. The research pointed towards the miniaturization of the stimulation setup towards a miniLED-LCE integrated device. Plus, a deeper study of the characteristics of the material under stimulation was carried out in this phase, taking into account other physical quantities besides active tension and relaxation and activation kinetics (whose definitions are given above).

Part of the study underlying the results contained in this Thesis work was conducted in isometric conditions, in which the strip was allowed to contract while clamped at both sides; another part of the research dealt with the characterization of the strip undergoing isotonic contraction: thus, lifting a weight on one side (while shortening) and clamped on the other.

The overall goal of the research was to prepare an implantable material capable of reproducing an amount of active tension which is similar to the one generated by native human cardiac muscle, with adequate kinetics during the force generation process and which is easily stimulable and efficient.

2.3.1 Optimization of dye content

The research work on artificial muscles to assist cardiac contraction, described in this Thesis project, starts from the early results commented in the previous section. Its objective was to overcome the various issues presented by the first setup in order to enhance the performance of the contraction assist device based on the light-responsive LCE film. The first one that was encountered regarded the uneven actuation of the LCE film throughout its entire thickness.

LCE1, due to the high molar absorption coefficient of **D1** dye, results non-transparent, and the ineffective penetration of light throughout the whole sample thickness translates into uneven contraction of the sample when irradiated. Thus, an experiment considering the influence of dye content on the force generation process was set up, to assess whether reducing dye content could lead to a homogeneous activation of the sample without loss of performance.

A series of samples with a low content of dye was prepared and characterized, decreasing the amount of dye to 0.5 % mol/mol and 0.3% mol/mol, while keeping the amount of **CL1** crosslinker constant (10% mol/mol). The content of **M1** monomer was changed accordingly to the decrease in dye concentration from the reference value of 1% mol/mol; photoinitiator content was not altered (1% mol/mol).

Changing dye content in the mixture reflected itself into a change in the kinetics of force development, while crosslinker percentage in the strips affected the levels of active force developed upon stimulation. This result can be explained by considering how force is developed in the artificial LCE-based muscle: the number of azobenzene absorbers does not affect the passive properties of the material, which turned out to be the main determinant for the level of active force exerted on the transducer by the strip. Active force levels upon sustained illumination (tON = 10000 ms) were, thus, unaffected (Figure 2.8a-b); conversely, activating the strips with a short irradiation time (tON = 250 ms) resulted in a fourfold decrease in active force level. In conclusion, decreasing dye content in the mixture causes the strips to activate with a slower kinetics (Figure 2.8c) without any effect on the developable active tension.

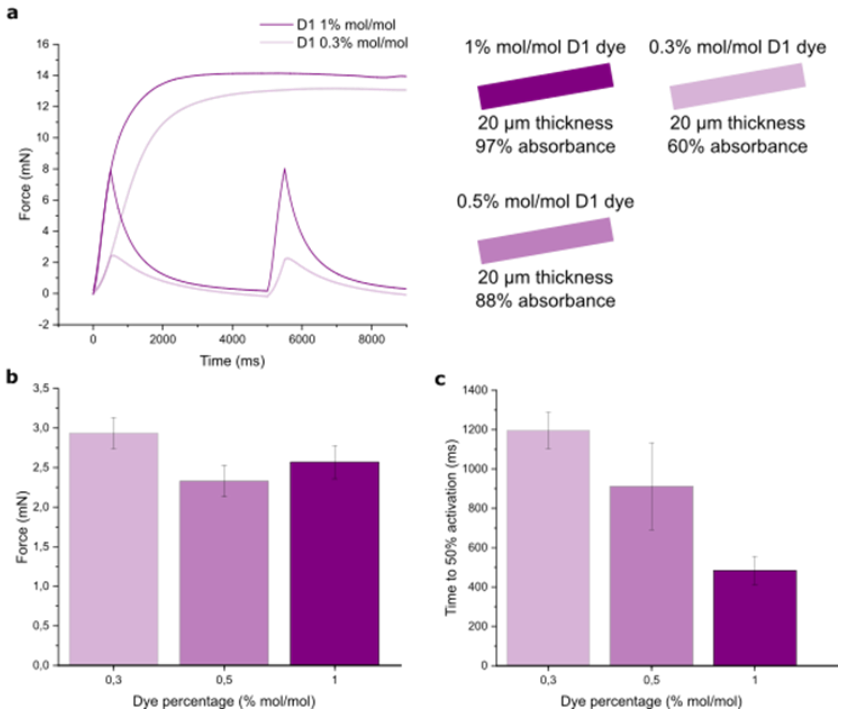

*Figure 2.8: Mechanical characterization of low-dye-content mixtures. All experiments were conducted in wide illumination conditions, at 1.5 mW/mm^2, in water environment at 25°C. (a): Sample active force-time traces for mixtures with dye **D1** at 1% mol/mol and 0.3% mol/mol percentage, showing how lowering dye content results in slower kinetics in force development, but same level of active force developed upon sustained illumination (tON = 10000 ms). On the right side, light absorbance of the strips at 530 nm at different dye concentrations are shown. (b): Active force as a function of dye content upon sustained illumination (tON = 10000 ms). (c): Activation halftime upon sustained illumination (tON = 10000 ms) as a function of dye content.*

To further consolidate this hypothesis, the influence of the crosslinker amount variation when dye content is fixed can be taken into account; early results contained in the research article by Ferrantini *et al.* show that active force (in confined illumination conditions, at 100 mW/mm^2 excitation power, in air) is dependent on the amount of crosslinker **CL1**.[3] Indeed, if the reference mixture **LCE1** (10% mol/mol) proved to be capable of developing a level of active tension of 387±45 mN/mm^2 in such conditions, keeping the same dye amount and increasing the crosslinker percentage to 15% mol/mol and 20% mol/mol results in an increase of the active tension value to 393±82 mN/mm^2 and 423±17 mN/mm^2 respectively. However, this increase in active force is obtained at

the expense of increasingly slower kinetics in force development process. Thus, altering dye content affects force generation kinetics only, and LCE mixtures with amounts of dye **D1** higher than 1% mol/mol were not characterized due to the need to maximize the absorption of light throughout the whole thickness of the sample.

2.3.2 Effect of light stimulation pattern

To further investigate the dynamics of force generation in the artificial LCE-based muscle and the influence of the stimulation spatial pattern on force generation, the efficiency of a LCE strip as an ideal machine transforming all input light power into mechanical work was estimated, in order to compare the efficiency of the LCE when illuminated using either a local illumination source (an array of four aligned green miniLEDs) or the LED lamp that had been used so far to provide wide illumination of the strip.

An experiment in which the strip is allowed to contract isotonically (while shortening lifting the same weight throughout the whole contraction, as opposed to the isometric contraction setup used thus far, in which the sample was contracting under geometrical constraint), with a known sample mass at one of its ends, was designed to calculate the peak mechanical work. This parameter was obtained, in brief, as the product between the force needed to lift the sample weight (F) and strip displacement (ΔL). The arrangement of the experimental setup was thus changed: the motor was substituted with the sample weight, the strip was mounted perpendicularly to the force transducer, which is at the other end of the sample, and light impinged on the sample perpendicularly to the plane described by the force transducer and the sample weight - LCE strip system. With a sample weight mass of 100 mg attached on the opposite side to the transducer, the muscle was able to contract isotonically. A camera recorded the displacement of the strip, actuated by the LED lamp; the strip contracts while working against weight force (Figure 2.9).

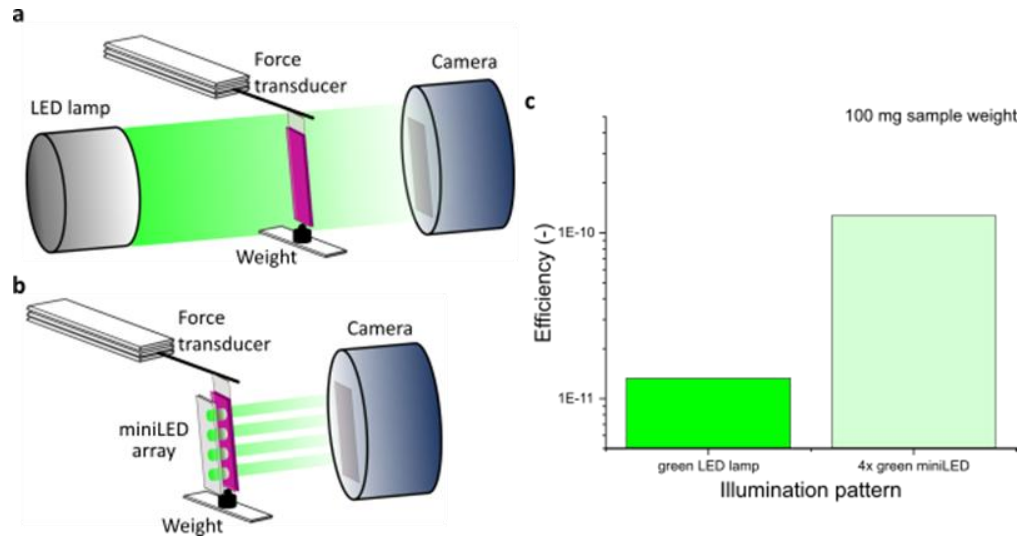

Figure 2.9: Assessment of the efficiency of the LCE strips. (a): Actuation of the LCE strip with a LED lamp in the horizontal arrangement of the illumination setup. (b): Actuation of the LCE strip with the illumination provided locally by an array of 4 miniLEDs. (c): Comparison of the efficiency of the LCE strip in different illumination conditions. Actuation with a local source (4-miniLED array) resulted in a tenfold increase of efficiency compared to the wide illumination provided by the LED lamp.

Efficiency is calculated as the ratio between peak mechanical work and provided light intensity; the latter was calculated as the product between light power (*P*) and illumination time (*tON*):

$$\eta = \frac{\Delta L \cdot F}{P \cdot tON} \qquad \text{Equation 2.1}$$

The calculation of mechanical work is explained more in detail in the experimental section. Figure 2.9c shows how illumination with a local source (an array of 4 green-emitting miniLEDs) is more effective than the wide illumination conditions used thus far. Efficiency is ten times higher than when using a LED lamp, even if this is more powerful than the 4-miniLED array in terms of total output irradiance of the source. It can be hypothesized that the increase in efficiency is due to the local irradiation of the LCE matrix, which also provides a concomitant heating effect of the polymer, that increases its mobility. Early studies, indeed, showed that **LCE1** has a T_g around 20°C, thus the polymer is rubbery in the usage conditions.[93]

In view of a future *in-vivo* implantation of a LCE-based device, this kind of illumination pattern is easier to downscale than exciting the dye-doped LCE using a conventional source such as a laser or a LED lamp.

2.3.3 Use of a different dye

To enhance the efficiency of the LCE-based muscle, dye **D1** was substituted with dye **D2** (commercially known as Disperse Red 1 acrylate), preparing **LCE2** mixture (Figure 2.10). **D2** has a strong absorption peak centered in the blue region of the UV-Visible spectrum, at 470 nm, and is used in literature to prepare light-responsive LCEs.[94]
Starting from the composition of the reference mixture **LCE1**, in **LCE2** dye content was not altered and kept at 1% mol/mol, while keeping the same amounts of crosslinker **CL1** (10% mol/mol), monomer **M1** (88% mol/mol) and photoinitiator **IN1** (1% mol/mol), as shown in Figure 2.10. Thus, passive properties were not modified in the LC network, while the absorption peak of the embedded dye shifted from 536 nm to 470 nm.

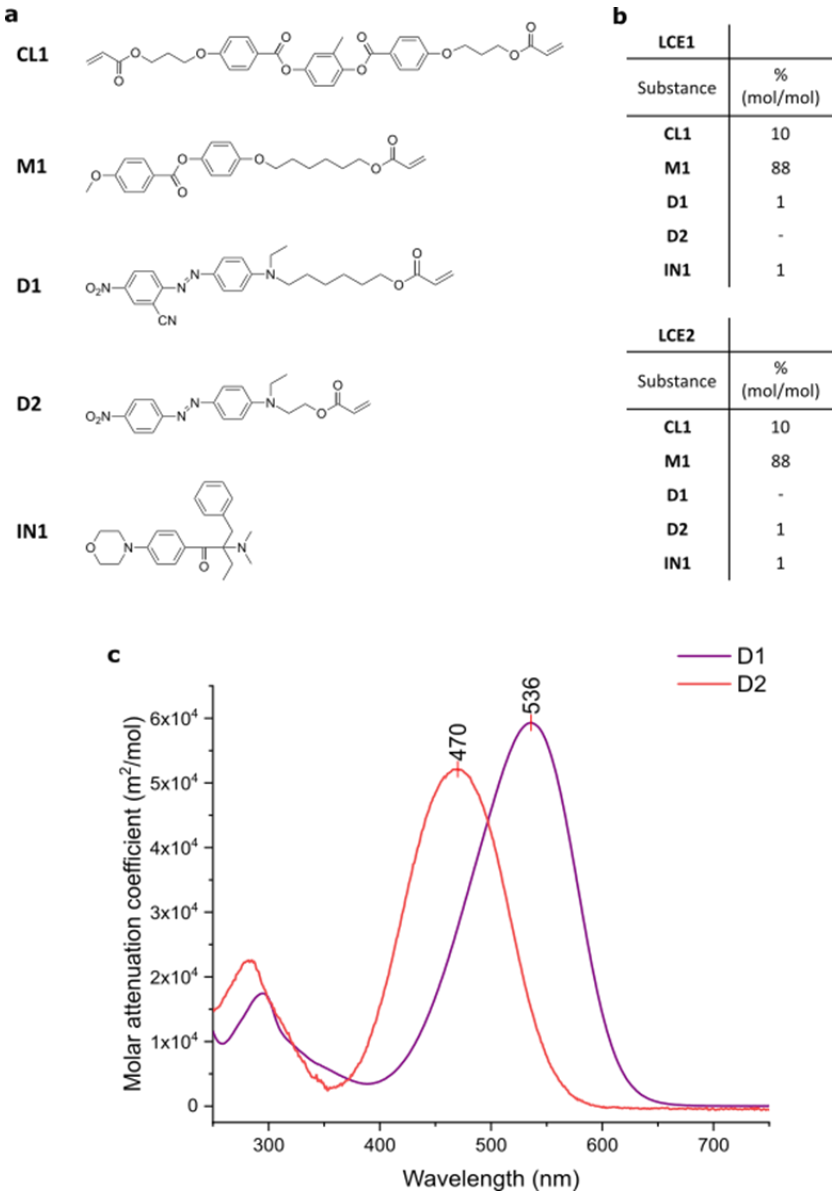

*Figure 2.10: Mixtures used throughout the work and chemical structures of the reagents. (a): Chemical structures of LC monomers (diacrylate **CL1** and monoacrylate **M1**), dyes (**D1**-**D2**) and photoinitiator (**IN1**). (b): Chemical composition of the two light-responsive LCE-based materials that were prepared and characterized: **LCE1** (top), the reference material, doped with dye **D1**, which has an absorption peak centered in the green region of the visible spectrum; **LCE2** (bottom) equipped with dye **D2**, which has an absorption peak centered in the blue region of the visible spectrum. (c): UV-Visible absorption spectra of dyes **D1** (purple line) and **D2** (red line).*

The first proof-of-concept experiment to demonstrate the superiority of **D2** to **D1** was conducted using strips cut from samples from **LCE1** and **LCE2** with splayed alignment. As it is discussed above, LCEs with splayed alignment are capable of bending upon stimulation, with the bending angle depending on the intensity of the stimulus.[26,95] This kind of deformation is easy to be measured with a simple setup (Figure 2.11).

Comparing the bending angle as a function of light intensity (in wide illumination conditions in air) in strips from the two mixtures, it can be seen how dye **D2** (under blue light irradiation at 460 nm) outperforms dye **D1** (under stimulation with green light at 515 nm), showing an almost 90% increase in actuation when the same value of light irradiance is provided to the sample. **LCE1**, equipped with dye **D1**, shows a bending angle of almost 67° under green light at 10.45 mW/cm^2; **LCE2**, with dye **D2**, shows a bending angle that doubles the one displayed by **LCE1** under blue light at the same intensity. Plus, the actuation threshold is lower in **LCE2** (Figure 2.11b, red squares) than in **LCE1** (purple dots) in these experimental conditions.

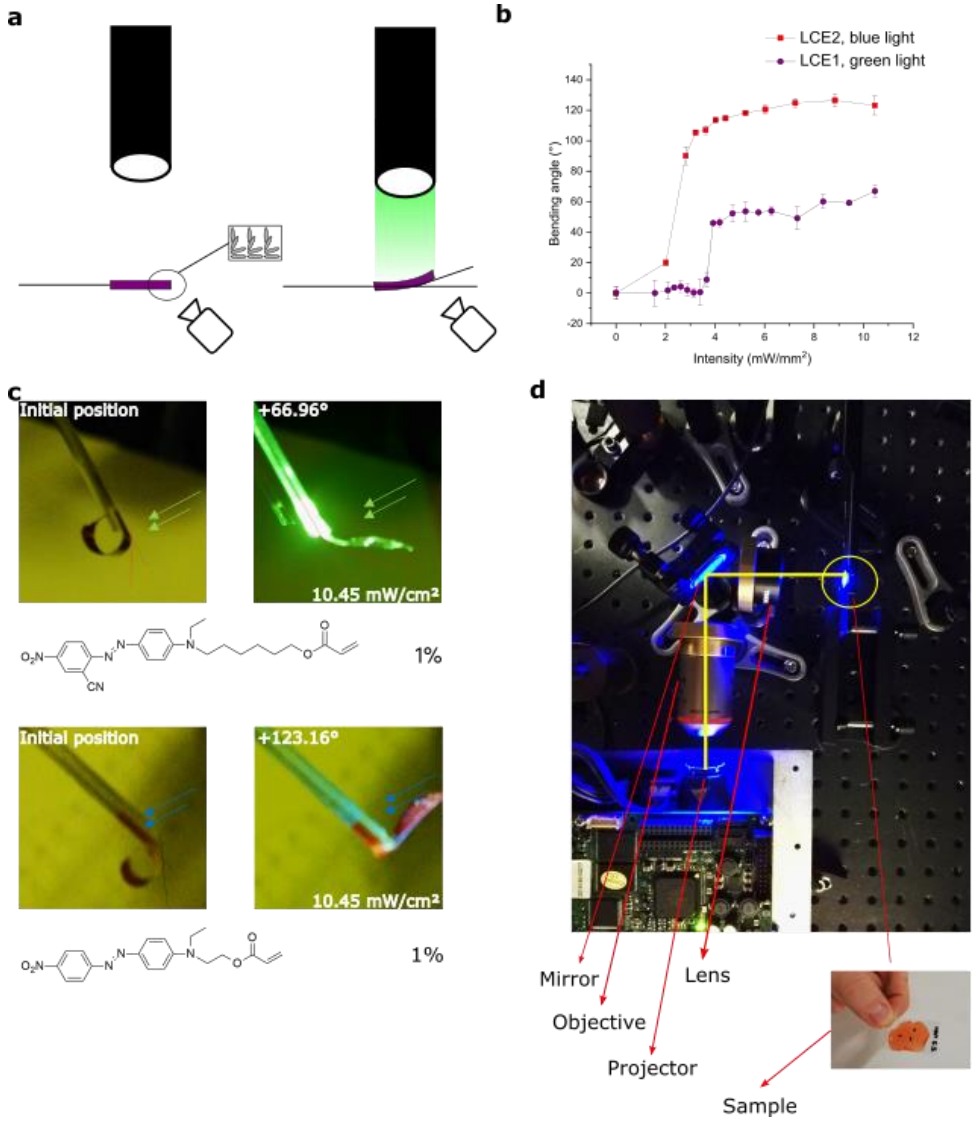

*Figure 2.11: Comparison of the performances of the dyes **D1** and **D2**. (a): Scheme of the experimental setup: a strip in splayed alignment cut from a LCE film of either **LCE1** or **LCE2** (which differ for the dye in the network only, respectively molecules **D1** and **D2** in Figure 2.10) was irradiated with a projector lamp (excitation wavelengths 460 nm and 515 nm); the resulting bending was recorded with a camera and the angle was measured as a function of the stimulation intensity. (b): Comparison between the performances of a splayed strip of **LCE1** under green light stimulation and a splayed strip of **LCE2** under blue light irradiation (wide illumination, in air). (c): Visual comparison of the bending angle of the two strips at the same intensity. Top: **LCE1**, equipped with dye **D1** (depicted below); bottom: **LCE2** (dye **D2** shown below). (d): Photo of the experimental setup, with the optical path highlighted in yellow and a close-up of a LCE film.*

2.3.4 Use of an array of blue miniLEDs

Following the findings of the previous experiments, that demonstrate how a source that guarantees a local stimulation of the sample actuates the strips more efficiently compared to the wide illumination of a LED lamp, an array of blue miniLEDs was fabricated in order to compare the performances of **LCE2** and **LCE1** in the same conditions with a local stimulation source. Thus, a new miniLED-LCE device was designed, using mixture **LCE2** with dye **D2**, which proved to have better performance than **LCE1** with dye **D1**. Two linear arrays of miniLEDs were prepared, with 4 and 6 miniLEDs respectively. The former is the analogue of the system used to excite **LCE1** in the previous experiment, while the latter is an enhancement of this system, whose length did not change (and thus, a higher number of light sources was accommodated in the same space as the previous experiment).

The efficiencies of the LCE-based device with either the 4-miniLED array or the 6-miniLED one were calculated with the same experimental setup used before, irradiating the strip to trigger its isotonic contraction using a sample weight of 100 mg. Moreover, the thickness of the samples was scaled down to 10 μm, to get a more efficient illumination throughout the whole sample. Switching to the blue miniLEDs and further reducing sample thickness contributed to an almost fourfold increase in efficiency in the case of the blue 4-miniLED array, and to a sixfold increase in efficiency in the case of the one-sided blue 6-miniLED array, compared to **LCE1** stimulated with the 4-green-miniLED array.

The illumination system was further improved, fabricating a double linear array (Figure 2.12) of 8 blue miniLEDs per side, in which the strip was sandwiched. The spacing between two LEDs corresponds to the full width at half maximum of the emission cone of the miniLED, guaranteeing homogeneous irradiation of the sample. The efficiency of the LCE with this illumination pattern was assessed as previously, using different sample weights and allowing the LCE strip to contract isotonically. All experiments were carried out in air, at ambient temperature.

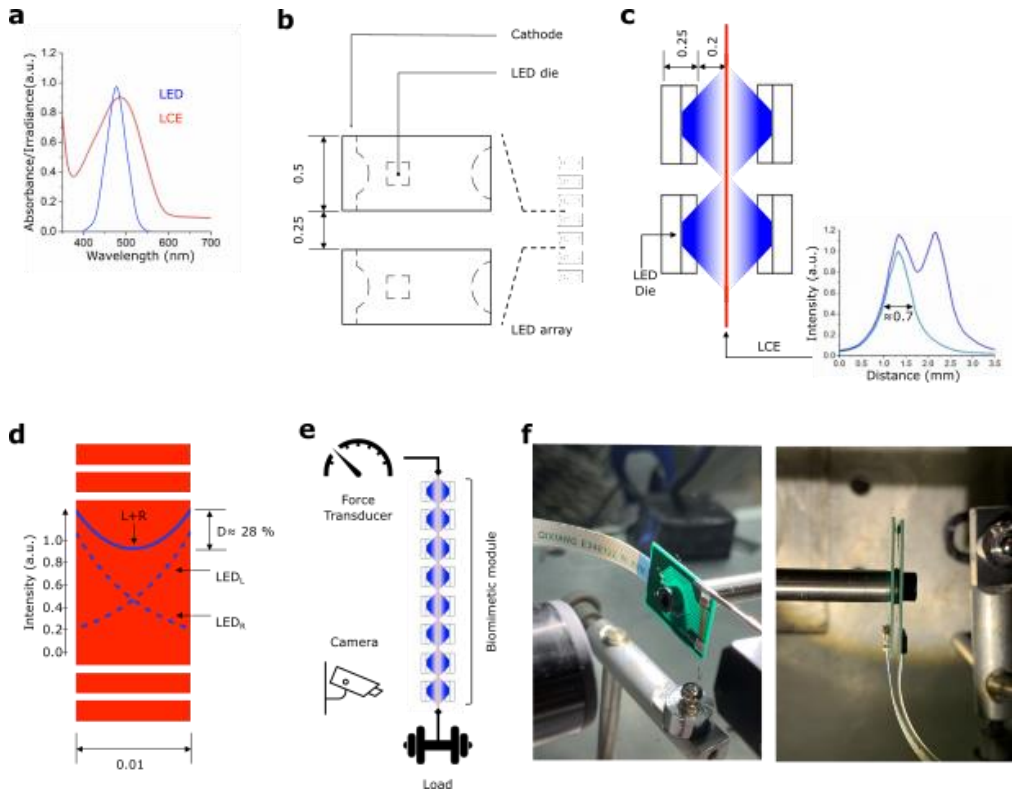

*Figure 2.12:MiniLED-LCE system with two linear arrays of miniaturized light sources. (a): Absorbance spectrum of **D2** dye, overlapped with the normalized emission spectrum of the blue LEDs. (b-c): Scheme of the miniLEDs and design of the contractile unit, with the spacing between two light sources and the size of each one. (d): Contributions from the LEDs on the left (LED_L) and on the right (LED_R) of the active layer throughout the thickness of the LCE film. (e): Scheme of the experimental setup: the LCE strip is clamped to the force transducer on one side and to the load (a sample weight) on the other side; displacement is measured through a camera, and illumination to the strip comes from the two 8-miniLED arrays in front of each other. (f): Photos of the setup, showing the arm of the force transducer, the LCE strip in front of one of the two miniLED arrays, and the sample weight on the other side to the force transducer(left) and the two miniLED arrays in front one another (right). In the particular case depicted here, a load of 5000 mg is used, thus the LCE is in isometric conditions. The other experiments were conducted using loads that enable the LCE strip to contract isotonically (100 mg, 200 mg, 500 mg).*

First, a single segment of the LCE strip was actuated, to measure the force and the kinetics of force generation and relaxation as a function of the provided light intensity (Figure 2.13). A non-linear relation between the generated force and the irradiance was found, with force increasing as light intensity increased, as expected (in the seminal work

presented by Ferrantini *et al.* a similar behavior was found for **LCE1**).[3] Kinetics of force generation and relaxation were faster as light intensity got more intense, showing a fivefold decrease in relaxation time and a threefold decrease in activation time (always taking into account the time for 50% rise and 50% fall to and from the plateau in the force-time curve). Experiments were conducted in maximal force conditions, allowing the strip to contract for four seconds (sustained irradiation), and mean data were measured on 4 LCE strips.

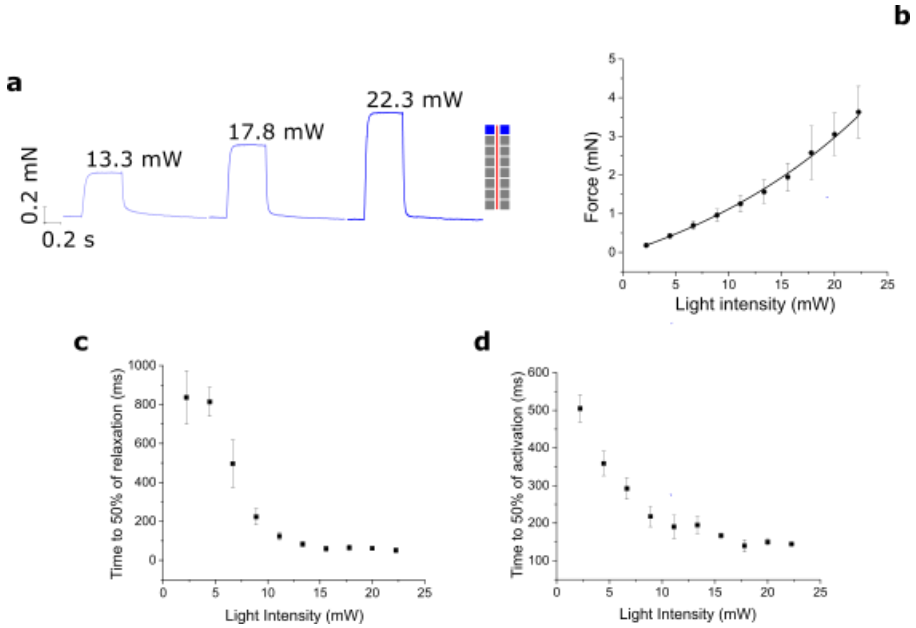

Figure 2.13: Optomechanical characterization of the miniLED-LCE strip with one activated segment. (a): Representative force-time traces at progressively increasing light intensity (left) and force-light intensity curve (right). An exponential dependency of force on light intensity was found. (c-d): Kinetics of force generation and relaxation expressed as rise time to 50% peak and fall time to 50% of the maximal force. Increasing light intensity implied faster kinetics, as expected.

The contributions of the two miniLED arrays were then evaluated, irradiating the strip with a progressively higher number of segments on the two matrices. A LED was switched ON on one matrix, then the corresponding one on the other matrix was switched ON; afterwards, the LEDs were switched OFF and the strip was allowed to relax. In the following activation cycle, the next LED on the array was switched ON, along with its

homologue on the other side, and so on. Results are reported in Figure 2.14. As expected, the force generated when progressively switching more LEDs increased non-linearly.

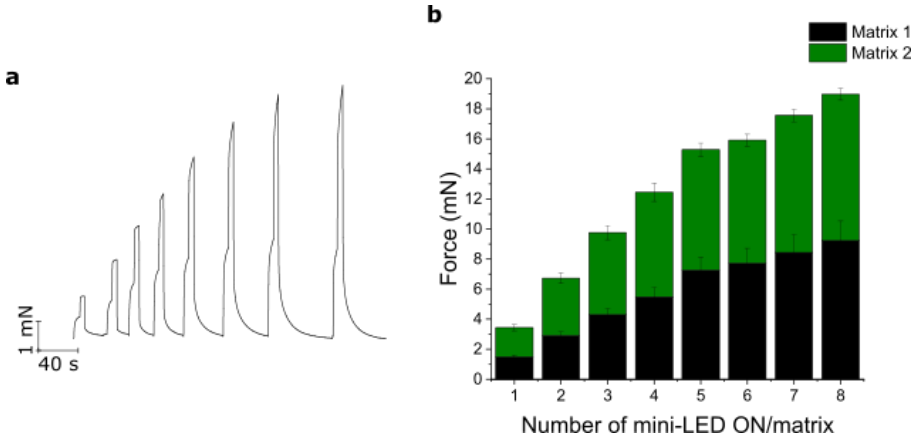

Figure 2.14: Influence of progressively increasing light intensity on force generation. (a): Representative force - time trace of the miniLED-LCE system when a progressively higher number of mini-LEDs was switched ON. First, a mini-LED was switched ON on the first matrix; then, the corresponding one on the second matrix was switched ON, and so on. (b): Dependency of the force on the number of ON miniLEDs on each matrix.

Once the non-linear dependence of force on light intensity was assessed, another experiment to study the effect of an increasingly higher number of light segments switched ON (when both LEDs in front one another were activated) on the kinetics of force generation was conducted (Figure 2.15). The LCE strip experienced a twofold decrease in the activation time when eight LED segments were switched ON compared to one active light segment, in a nonlinear fashion. Relaxation time, instead, was found to increase as a higher number of light segments were switched ON.

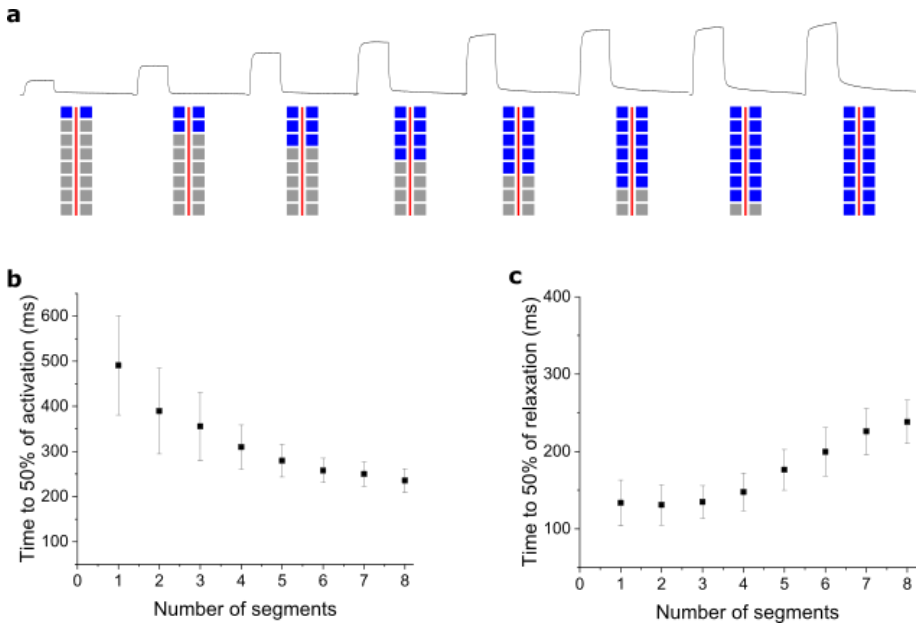

Figure 2.15: Modulation of force generation kinetics upon progressive increase of active light segments. (a): Representative force-time traces when a progressively higher number of light segments were switched ON on the LCE strip. (b-c) Effect of active segment number on contraction kinetics.

Further characterization dealt with the effect of activating two segments separated by an inactive part of the LCE strip (Figure 2.16). The force generated upon activation of one segment only is taken as a reference; then, progressively distant segments were activated along with the first one, and the dependency of force on segment spacing was assessed. When two neighboring couples of LEDs were switched ON, active force doubled, compared to the reference; this value plunged as the spacing was raised, to remain constant when the spacing between two segments reached 3 mm. This characterization further supported the design of the illumination setup, which proved to be efficient in activating the LCE strip with the provided distance between the light sources. Plus, this drop in active force is also explained by taking into account the influence of the non-irradiated, and thus inactive, segments of the LCE strips on the irradiated ones. Dark parts of the LCE, indeed, damp the stimulated ones; the light stimulus does not propagate throughout the sample, which has to be directly stimulated to work efficiently.

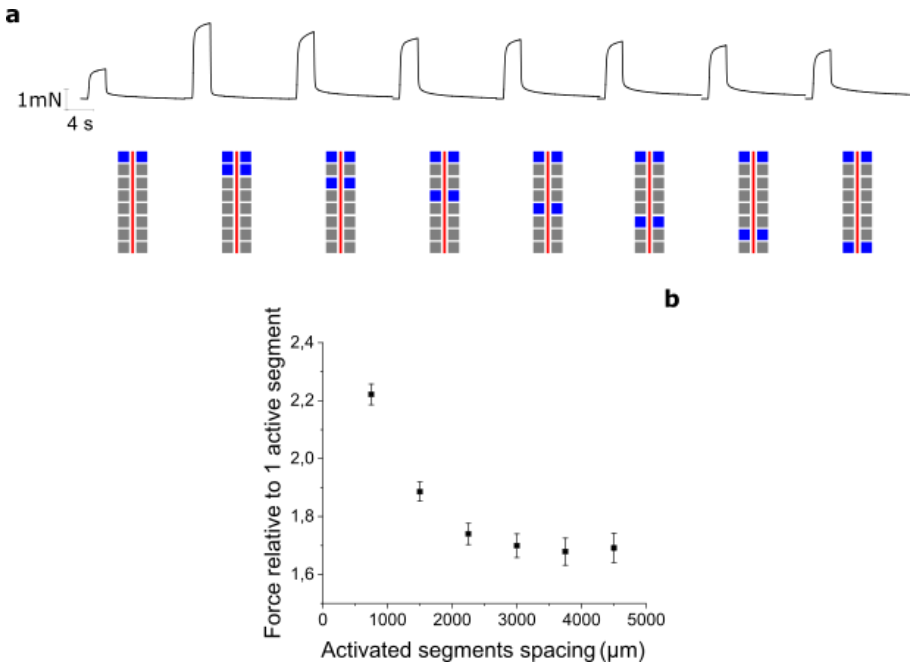

Figure 2.16: Influence of the light stimulation pattern on force generation. (a): Representative force-time curves of the minLED-LCE system. First, the reference segment was switched ON; then progressively farther LED couples on both matrices were activated. (b) Relative force amplitude at increasing source spacing.

Additional characterization in Figure 2.17 confirmed that the activation of two neighboring segments proved to be more efficient than the illumination provided by the same number of source in a different spatial arrangement, where the distance between the sources exceeded the full width at half maximum of the spatial emission spectrum of the LED (reported above in Figure 2.12a).

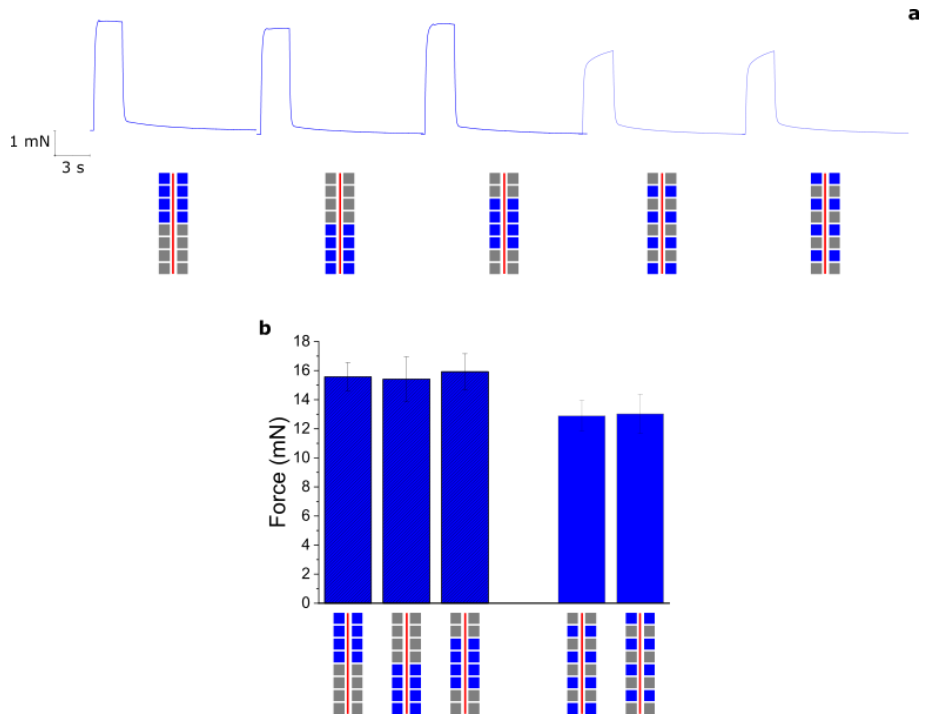

Figure 2.17: Influence of the light stimulation pattern on active force. (a): Representative force traces obtained when different light patterns were used to activate the strip. (b): Active force developed when illuminating the LCE strip with four LEDs differently arranged. The difference is evident when the same number of light sources, and thus the same light intensity, is provided inhomogeneously on the sample, exceeding the full width at half maximum of the spatial emission spectrum of the LED.

The overall goal of the experiments reported so far was to characterize the efficiency of the miniLED-LCE contractile unit and its power density, to compare these data with the currently used soft actuators in the biomedical field (Figure 2.18). Thus, in this phase, the strip was allowed to contract isotonically to measure its displacement (as it was previously done with **LCE1** actuated with either the LED lamp or the 4/6-green-miniLED array and with **LCE2** actuated with the 4/6-blue-miniLED array) to characterize its thermodynamic efficiency. The displacement was measured, as usually, with a cMOS camera, and the force needed to lift the sample weight through the force transducer. As expected, strip displacement decreased and active force increased as weight soared.

Mechanical work and efficiency were calculated on the basis of Equation 2.1 from peak mechanical work (see the experimental section for details). A great improvement in the

performance of the miniLED-LCE system was achieved using the blue two-8-miniLED illumination system. Compared to the seminal work that constituted the base for the design of the contractile unit presented here, efficiency shot up by six orders of magnitude almost reaching $\eta = 10^{-5}$, confirming the improvements guaranteed by the new design of the contractile unit and how **D2** under illumination with blue light provided by a local source outperforms **D1**, both in wide illumination conditions and in local illumination conditions under green light irradiation.

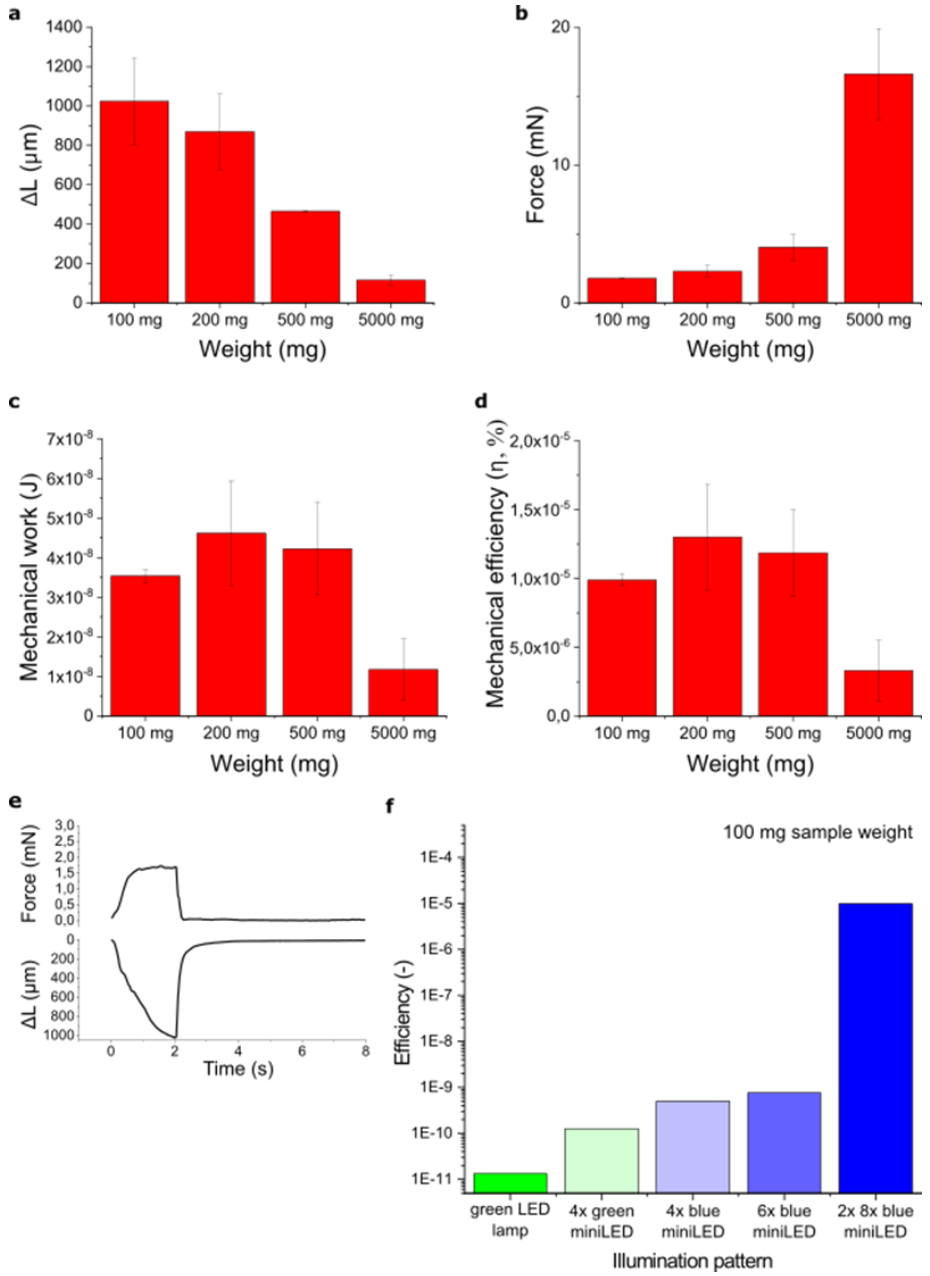

Figure 2.18: Evaluation of mechanical work and efficiency. (a-d): Dependence on sample weight mass of active force, strip displacement, mechanical work and thermodynamic efficiency for the blue 2x-8-miniLED-LCE system. (e): Sample force-time and length-time curves, showing how the artificial muscle shrinks upon stimulation while exerting force; the maximum force value is reached when sample length is at its minimum. (f): Comparison among the different light-driven LCE-based systems designed throughout the research work.

The actuator here designed has a work density in the range of hundreds of J/m^3, thus slightly lower than the other LCE-based systems reported in the literature, and an output strain of more than 10% under constraint. Efficiency is still low, but the findings reported in this chapter pave the way for a further enhancement of its performance (Table 2).

Typical work density (J/m^3)	**Efficiency** (-)	**Typical output strain** (%)
$2{,}57 \cdot 10^{2}$	$9{,}89 \cdot 10^{-6}$	11.90%

Table 2: Parameters of the 8-miniLED-LCE artificial muscle with two linear arrays of miniLEDs, taken from the experiment in which the muscle contracts isotonically subjected to a 100 mg load. The detailed calculation of the parameters is described in the experimental section.

2.3.5 Optomechanical and mechanical characterization

A deeper study of optomechanical and mechanical properties of the mixtures discussed above was carried out by Mr. Luutzen Wymenga and Dr. Tianyi Jin at TU Delft, in the context of the European Project REPAIR.

Young's Modulus was calculated from stress-strain experiments at room temperature and at 37°C (Figure 2.19); the latter measurement was carried out to assess the mechanical properties of the polymer in the usage conditions of the LCE-based contraction assist device in a physiological environment. Samples were measured using a Mitutoyo micrometer (with 0.001 µm sensibility) placing the LCE film between two smooth silicon wafers (whose thickness, 500 µm, is known and highly accurate), which are used to calibrate the micrometer. Average sample length is 30 mm, while width is in the 7-10 mm range. Films are then fixed using two clamps for DMA testing with a torque of 0.7 N·m and tested with a DMA Q800 (TA Instruments). After the first two trials with strain rates of 100 µm/min and 1000 µm/min, the strain rate was chosen to be 400 µm/min for the other experiments. Measurements were carried out in daylight for the samples measured at room temperature and in the dark for samples measured at 37°C (due to the presence of the heating chamber of the DMA tester).

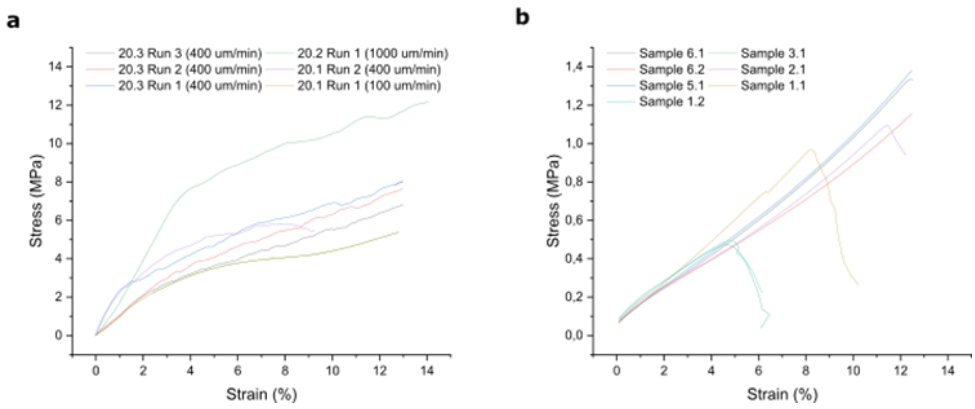

*Figure 2.19: Stress-strain diagrams for **LCE1** (20 µm thickness). (a): Stress-strain diagram at room temperature on three samples, six runs. Displacement rate for each experiment is reported. (b): Stress-strain diagram at 37°C on five samples, seven runs, with displacement rate 100 µm/min*

Samples broke when a fast strain rate (1000 µm/min) was applied. Total elongation after the experiment is between 12.5% and 25% of the initial length.

Young's modulus was calculated from the data in the range 0.1-2% strain, where a linear correlation between stress and strain was observed. Maximum tensile stress was obtained as the ratio between the force applied at the break and sample cross-section. Comparing the data shown in Table 3, a tenfold decrease in Young's modulus was observed when raising the temperature to 37°C. This phenomenon can be explained by taking into account the glass transition exhibited by **LCE1** at ~20°C, as it was previously observed.[93] The polymer is, thus, in its rubbery state in a physiological environment and displays a lower Young's modulus. The stress-strain relation and the static mechanical properties of **LCE1** are considered the same as **LCE2**, since the variation in the composition of these two systems is limited to the monoacrylate dye only; thus, properties such as T_g and Young's modulus are not affected by this change in the mixture. Mechanical tests were limited, in this phase, to LCE1 polymer only.

	25°C	**37°C**
Cross section (mm^2)	0.23±0.01	0.16±0.03
Young's Modulus (MPa)	135.96±38.30	10.05±0.50
Strain at break (%)	>7.64±2.23	0.99±0.34
Maximum tensile stress (MPa)	>11.30±2.24	9.07±3.24

*Table 3: Mechanical properties of **LCE1** obtained via stress-strain measurements at room temperature and at 37°C. A tenfold decrease in Young's modulus was observed when raising the temperature to a physiological value. LCE films at 25°C did not break during the experiments, thus ultimate values are shown as strain-at-break and maximum tensile stress values.*

Light-dependent dynamical behavior of **LCE1** and **LCE2** was assessed via dynamical mechanical analysis (DMA) under light stimulation. In this kind of experiments, storage modulus *E'* (the in-phase component of the stress, responsible for its elastic properties) and loss modulus *E''* (out of phase, damping) are measured under a dynamic load applied with a certain frequency. The ratio *E''/E'*, indicated as tan δ, accounts for the damping properties of the material.

Figure 2.20 reports the results of the optomechanical characterization of **LCE1** and **LCE2** conducted using a DMA machine. Samples were stimulated with a green LED lamp whose emission peak is at 530 nm, while **LCE2** was irradiated with a LED lamp that emits at 470 nm.

First, the influence of preload on the force generation process was assessed (Figure 2.20b). A LCE film from **LCE1** mixture was mounted in the DMA machine, and tested for 15 minutes applying a static force of 15 mN. Three pre-strain values of 0.1%, 1% and 2% were applied to the sample, which was then irradiated with a square pulse with tON = 60 s and tOFF = 60 s at an irradiance of 89.1 μW/cm^2 at 530 nm (using a LED lamp as the previous optomechanical characterization experiments). No difference in the amounts of force generated upon illumination were observed using different preload strain values.

Subsequent characterization took into account the influence of light stimulation on storage modulus *E'* and tan δ, in a DMA experiment in which the sample was subjected to a dynamic load with varying frequency (1-3 Hz) and a preload of 10 mN (Figure 2.20c). After a 5-minute waiting time, the LED lamp was switched ON and OFF with a period of 5 minutes (using a square pulse generator) and increasing the irradiance at each step. Storage modulus decreased and tan δ increased as irradiance got higher. On the other hand, tan δ did not experience such a dramatic change. Thus, elasticity declines upon irradiation, while damping properties are enhanced (*E'* experiences a 12-fold drop when irradiance reaches 43.9 mW/cm^2). Frequency of dynamical load influences storage

modulus too, since the higher is the frequency, the lower is the storage modulus, as a result of the lower recovery time of the material to its original state upon high-frequency loading.

Lastly, active tension, upon irradiation with the 530 nm LED lamp for **LCE1** and with a 470 nm LED lamp for **LCE2**, was measured using the DMA machine coupled with the light sources. The results are reported in Figure 2.20d-e. The data from this experiment are in line with the characterization carried out in the first phase of the study with a different setup, in which **LCE1** proved to be able to generate a tension of 70 mN/mm^2 when actuated at 150 mW/cm^2 irradiance.[3]

LCE2, which retains the same composition as **LCE1** but with a different dye, proved to be more efficient than **LCE1** also in this case. The blue-responsive mixture, indeed, was capable of generating almost 80 mN/mm^2 when actuated with a LED lamp at an irradiance of nearly 40 mW/cm^2; in the same conditions and at the same irradiance level, **LCE1**, its competitor, could only generate almost 60 mN/mm^2. A linear correlation between the stress (σ, in mN/mm^2) generated by the strips upon illumination and the irradiance provided by the light source (I, in mW/cm^2) can be drawn:

- $\sigma_{LCE1}\,(I) = (1.52 \pm 0{,}04) \cdot I + (0.42 \pm 0.94)$
- $\sigma_{LCE2}\,(I) = (1.99 \pm 0.05) \cdot I - (1.37 \pm 1.42)$

Comparing the two graphs in Figure 2.20d-e, it can be seen how **D2** requires a lower amount of light to actuate the LCE and generate active tension in the same order as dye **D1** in **LCE1**, under the same experimental conditions.

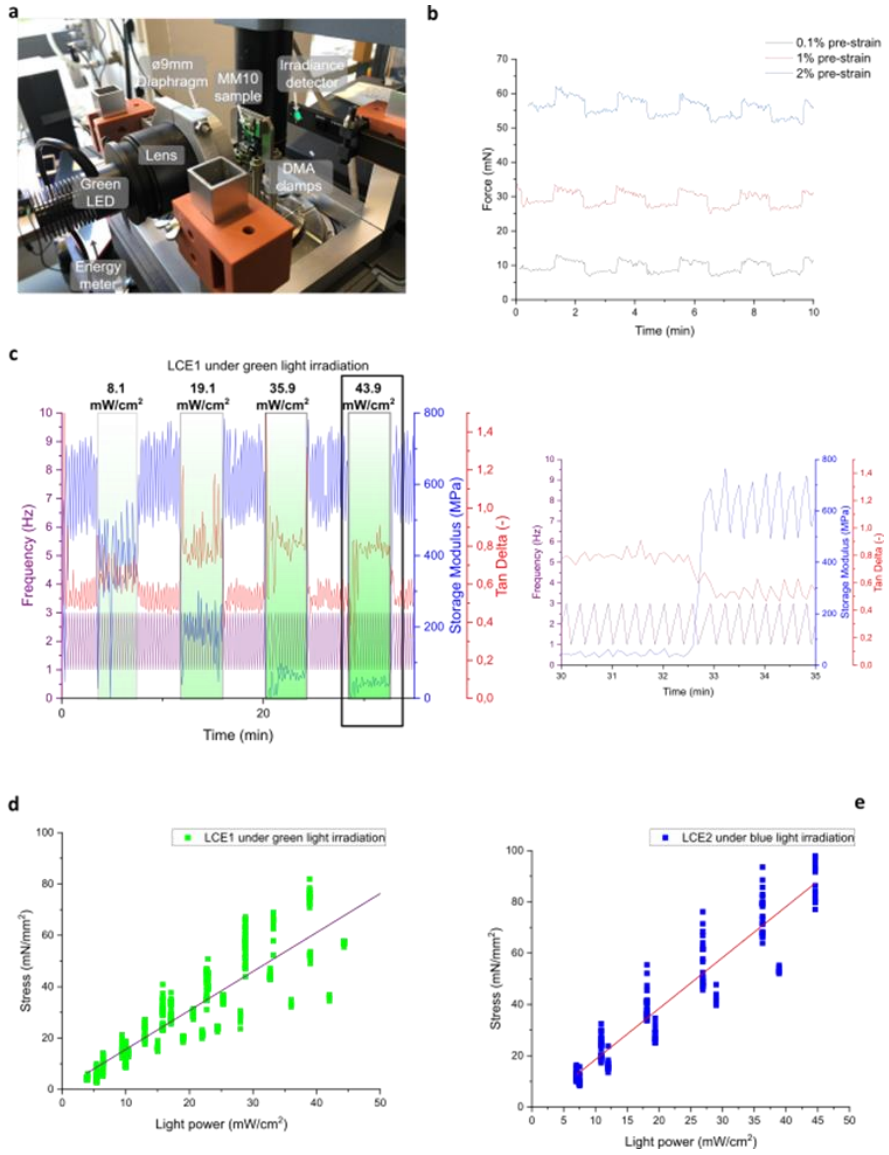

*Figure 2.20: Dynamical mechanical analysis under light stimulation and isometric force measurement upon irradiation for **LCE1** and **LCE2**. (a): Setup used for the measurements. The LED provides homogeneous irradiation of the sample, which is clamped with DMA clamps. The DMA machine provided the desired pre-strain values, dynamic load or static load on the film, and recorded the active force that was developed upon stimulation. (b): Isometric active force developed by **LCE1** upon green light stimulation under different preload conditions. (c): Storage modulus and tan δ variation upon irradiation with green light at 530 nm with varying intensity. (d): Active tension generated as a function of irradiance under green light stimulation for **LCE1**. (e): Active tension generated upon stimulation with blue light as a function of irradiance for **LCE2**.*

This strong increase in active force exhibited by **LCE1** (which in this set of experiments developed roughly the same level of active force as in the reference study with one quarter or the light intensity) can be attributed to the differences in the actuation setup, and the different load conditions experienced by the material. Indeed, in the course of the previous characterization carried out using the force transducer and the motor, strips were clamped using hooks at both ends, reinforced with standard scotch tape; on the other hand, the use of DMA clamps which constrain LCE film all over their width changes the loading condition of the material, which results in a different active force value when activated with the same illumination conditions.

2.4. Conclusions

The design of a contractile unit based on a LCE matrix as shape-changing material was presented here. Following the findings of the early results by Ferrantini et al,[3] that demonstrated the ability of LCEs to contract and support muscle contraction and the tunability of the material in terms of kinetics, active tension and passive properties, the objective of the research was to go beyond the proof-of-concept experiments and to build a prototype of the artificial muscle.

The main goal was the improvement of the efficiency of the light-sensitive system, and followed a two-pronged strategy:

- The adjustment of the composition of the LCE mixture, assessing the role of the photochromic molecule embedded in the network in the force generation process: in particular, the influence of its concentration and the use of a similar azobenzene, responsive to a different wavelength in the visible spectrum, were studied;
- The use of a different light stimulation pattern, in order not only to enhance the performance of the unit, but also to pave the way for the miniaturization of the unit in view of its use *in vivo*.

Decreasing the concentration of dye from 1% mol/mol, used as a reference, to 0.5% mol/mol and 0.3% mol/mol only had the effect of slowing down the kinetics of force buildup in the LCE system. Thus, with the concentration of dye staying at the reference

value of 1% mol/mol, another push-and-pull azobenzene was used, shifting the absorption maximum of the systems from green to blue light. From the point of view of the illumination pattern, the use of a local illumination source based on a linear array of miniLED proved to be beneficial to improve the efficiency of the artificial muscle.

Thus, bridging the gap between the two routes that were followed, the prototype of a blue-responsive miniLED-driven LCE-based contractile unit was designed. The influence of light stimulation pattern on the force generation process was studied, to characterize the thermodynamic efficiency of the system. This value, along with the active force generated and the halftime of activation and relaxation, was the benchmark metric to compare the different prototypes engineered throughout the work. Starting from the 10^{-11} efficiency of the first work published in 2018,[3] a six-order-of-magnitude increase in efficiency was found with the last prototype that was designed.

Other approaches that can be tried to modulate the response of the material, including the synthetic modification of one of its components to adjust the NI transition temperature, or the tuning of the mutual ratios among the monomers. However, the route that will be followed in the next works will be focused on the further miniaturization of the device, towards the fabrication of a light-stimulable patch or a CAD.

Indeed, further reduction of size is still possible for the LCE system presented here. First, the illumination system can be further optimized with the use of a microLED-based matrix. Apart from the miniaturization of the stimulation system, accommodating a high number of light sources in the same linear array could be even more efficient in the activation of the LCE layer, to fully exploit the entire length of the specimen. This research work will be carried out in collaboration with the research group of Prof. K. Zhang at TU Delft, whose people are kindly acknowledged for their help in the optomechanical characterization. Secondly, the possibilities enabled by 3D printing of LCEs will be explored. The use of additive manufacturing techniques, indeed, will have three immediate advantages:

- The further increase in the aspect ratio of the samples, towards the fabrication of a truly one-dimensional miniaturized contractile unit composed of independently contracting fibers;

- The improvement of the fabrication method of the LCEs, to reduce the variability induced by the use of surface effects to align the LCE mixture before polymerization: alignment via shear stress could, indeed, results more efficient in obtaining more standardized samples;
- The possibility to shape the device accurately modeling it on the patient's needs, to pave the way to personalized cardiac implants or assistance devices.

2.5. Experimental section

Materials. Molecules **CL1** and **M1** are LC reactive mesogens; the former is a diacrylate crosslinker, while the latter is a polymerizable mesogen with one acrylate end. Molecules **D1** and **D2** are polymerizable dyes. Molecule **IN1** is a UV-responsive photoinitiator, to start the polymerization of the LCN.

CL1 was purchased from Wilshire Technologies, **M1** was purchased from Synthon Chemicals GmbH , **D1** was synthesized following a procedure reported in literature,[96] **D2** was supplied by Specific Polymers, **IN1** was purchased from Sigma Aldrich. All reagents are solid and were used without any further purification.

Fabrication of LCE films. Samples were prepared using a well-known procedure to align low-molecular-weight LCs (Figure 2.21). Reagents in solid state were mixed in dichloromethane in a vial, and solvent was allowed to evaporate on hotplate at 70°C under stirring, before further evaporation at low pressure. LC cells were fabricated using two PVA-coated glass slides; these substrates are rubbed uniaxially with a velvet cloth to force planar alignment of the mesogens. After rubbing, slides were glued together using silica beads as spacer (with nominal thickness ranging from 10 μm to 50 μm). The mixture was infiltrated in the hollow space between the glass slides by capillary action in its isotropic phase (at 75°C); temperature was then decreased to 45°C, and the cell was irradiated with a UV lamp at 385 nm (M385L2-C4, Thorlabs) to trigger radical polymerization for 10 minutes at this temperature; a post-curing step, irradiating the samples with the UV light for 10 minutes at 65°C to ensure complete polymerization of the network, was then carried out. Cells were immersed in water overnight and opened

to retrieve the LCE film. Strips of the desired size were cut from the LCE films following the alignment direction.

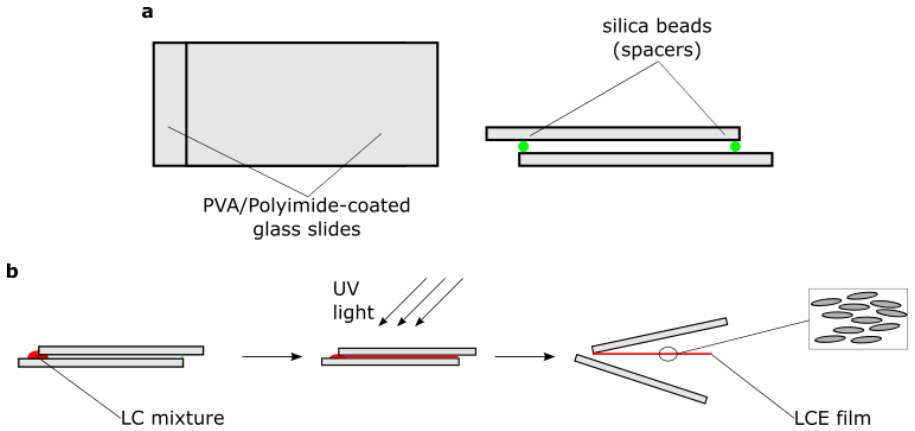

Figure 2.21: Preparation of samples. (a): Top view (left) and front view (right) of a liquid crystal cell, fabricated by gluing two polyimide-/PVA-coated glass slides using silica beads as spacers. (b): The reactive mixture is infiltrated by capillary action and, when the hollow space between the slides is completely filled with the mixture, the cell is exposed to UV light to start the photopolymerization; the cell is then opened and the LCE film, with planar alignment, is retrieved.

Active force evaluation. Unless otherwise stated, all experiments were conducted in isometric conditions, with the strip clamped at both ends with standard steel hooks commonly used to clamp intact muscles during actuation experiments. To prevent strip slipping from the hooks, ends were reinforced with standard scotch tape. The strips were mounted in a setup comprising a motor (Aurora Scientific Inc.), to control the initial length of the sample, and a force transducer (KG7A, Scientific Instruments Heidelberg), to measure the tension generated upon light stimulation coming from the top. The strips, prior to irradiation, were stretched until fully extended to their initial length, not to conduct the experiment in a condition where the sample is slack. This initial sample length was found measuring the force-displacement relation of the sample, starting with a slack strip, and lengthening it until a linear relationship between the tension measured on the transducer and the deformation is established, preloading the specimen as low as possible. Light stimulation was provided with either a continuous wave green laser (514 nm, 900±100 µm beam diameter, 0-200 mW/mm^2), a LED lamp (Thorlabs, 525 nm, ≈5 cm beam diameter, 0-1.5 mW/mm^2) or a custom-made array of commercial green

miniLEDs in the case of materials containing a **D1** dye, while a customized PCB array of commercial blue mini-LEDs (460 nm) was used to excite mixtures equipped with **D2**. Experiments in isotonic conditions were conducted substituting the motor with a sample weight of known mass that the LCE film was capable of lifting up and building the setup in a vertical configuration.

Data analysis. Active tension was measured using a LabView (National Instruments) script to analyze active tension-time relationship. Images and videos of live actuation of the strips and their displacements were recorded with a Thorlabs cMOS camera (space resolution 11.7μm/pixel, time resolution 2.8 ms).

Parameters in Table 2 are calculated as follows. Peak mechanical work was calculated from the force-time curve and the displacement-time curve (an example of the two curves is given in Figure 2.18e). From the latter, displacement speed was calculated as its first derivative, and, by multiplying force-time curve by displacement speed curve, the instantaneous power was obtained. Positive peak power value was multiplied by the sampling time of the camera, giving instantaneous peak mechanical work. The ratio between instantaneous peak mechanical work and LCE strip volume (taking into account that the dimensions of the sample in this set of experiments were 8.6 mm in length, 1.6 mm in width and 10 μm thickness) accounted for typical work density. The ratio between instantaneous peak mechanical work and the light energy provided to the sample is the thermodynamic efficiency of the system, as defined earlier in Equation 2.1. The displacement of the strip normalized by its initial length gives the typical output strain of the artificial muscle.

3. Use of micro- and nano-patterned surfaces based to enhance cell adhesion and growth

Extracellular matrix (ECM)-mimicking substrates with rational design of topography and rigidity play an important role in determining the fate of cells and the degree of maturity of *in vitro* models. [97–100]

ECM is a set of scaffold proteins that provides cells with signal molecules (i.e., growth factors) and mechanical support; it is hierarchically organized and shows a complex organization at the micro- and nano-scale. The achievement of the goal of the preparation of a synthetic tissue analogue obtained ex vivo must necessarily face a complete understanding of the processes through which cultured cells probe the environment provided by the scaffold, and their response.[101,102] Mechanobiology is the multidisciplinary study of the interaction between cells and their surrounding environment: how they sense and adapt to substrate stiffness, topography, porosity, wettability (among others) is of utmost importance when it comes to replicating the most accurately possible a viable tissue.

The research work presented here explored the influence of the first two characteristics on cell cultures derived from different lines, using either commercially available polymers or smart LCEs.

Topography provides a mechanical signal that is readily detected by cells, which can probe anisotropies or surface patterns. The use of anisotropic micro-/nano-scale cues is one of the most used methods to direct the orientational alignment and elongation of cells in culture. Alignment is, in various cell lines, a major factor that induces differentiation, proliferation and full development to maturity.[99,103–105] Substrate rigidity, on the other hand, is another aspect extensively researched in tissue engineering, since it is widely known that cells react differently to more or less rigid environments; plus, abnormal changes in ECM stiffness and tissue stiffening are correlated to the insurgence of pathological conditions and to the modification of cell functionality.[106,107]

3.1. Use of a micropatterned substrate to enhance cell adhesion and growth in cardiomyocytes derived from human induced pluripotent stem cells

The discovery of re-programmability of differentiated cells into a pluripotent state, for which S. Yamanaka received the Nobel Prize for Physiology and Medicine in 2012, paved the way to a new era in cellular biology. The generation of human induced pluripotent stem cells (hiPSCs) from ethical sources of somatic cells (e.g. dermal cells, blood or urine-derived cells) and without the constraint to harvest them from embryos, provided scientist with a powerful tool tissue repair, drug and disease modeling and can represent the breakthrough in personalized medicine.[108]

3.1.1 Introduction and aim of the research

Focusing on heart tissue engineering, cardiomyocytes derived from hiPSCs (hiPSC-CMs) are now being used as a model for various cardiac diseases, such as the ones deriving from muscular dystrophies. Their use is simpler than the exploitation of adult cardiomyocytes harvested from patients, which are hard to be grown outside the physiological environment and whose availability is limited. Plus, hiPSC-CMs maintain the genetic profile of the individual patient from which they are generated by reprogramming and subsequent differentiation (for instance, they retain the pathological condition in the case of a patient with a genetic cardiomyopathy).[109] Nevertheless, despite the potential of this approach, concerns arise on the complete maturity of cultured hiPSC-CMs.[109,110]

Mature hiPSC-CMs show a well-organized contractile system and an elongated shape. Thus, the design of new cell scaffolds and substrates and the implementation of new culture protocols (growth of cells under shear/elongation stress, electrical stimulation, etc.) to overcome the issue of incomplete cell maturation and to better mimic the *in vivo* environment has drawn attention from the scientific community.[101,111] This is a multidisciplinary challenge, in which biologists, biotechnologists, and materials engineers merge their efforts. Different approaches have been tried to fabricate cell

scaffolds with architectures similar to those found in the human body, with the goal of reproducing in vivo conditions and fully functional tissues. The field is extensively reviewed, and methods to improve maturity of cultured hiPSC-CMs to make their functionality similar to adult CMs range from mechanical loading to paced electrical stimulation.[98,99,112]

In particular, when dealing with surface topography modifications to enhance adhesion and growth of CMs, it is important to stress that this kind of cells, when adult, exhibit a high degree of spatial anisotropy, which is a determinant factor in the propagation of electrical pulses.[109] Thus, the presence on the cell scaffold of structures capable of inducing a preferential direction in hiPSC-CMs is critical, and positively affects cell behavior; a plethora of designs has been tried. For instance, Kim *et al.*, developed a ridged substrate based on poly(ethylene glycol)-diacrylate (PEGDA) that induced a high degree of anisotropy in neonatal ventricular rat myocytes; unpatterned cell cultures exhibited propagation of electrical pulses and contraction in random directions, while cells on patterned substrates displayed a marked directionality for these two parameters. A similar approach followed by Macadandang *et al.*, who cultured hiPSC-CMs using the same surface pattern on polyurethane-acrylate, led to similar results.[103,113] Au *et al.* created a polycarbonate abraded with lapping paper and combined surface patterning with electrical stimulation at 4.6 V/cm, 1 Hz frequency.[114] Electrospinning has also been used to create porous nanostructures with well-defined alignment.[115]

Another important factor that influences growth of hiPSC-CMs is substrate stiffness; Young's modulus of the materials will be taken into account as the main metric to describe this parameter. As mentioned above, various materials have been used to host hiPSC-CM cultures, with different rigidities. It is worthy to remember that myocardial tissue, in healthy adults, has a Young's modulus of 10-15 kPa; abnormal values that deviate from the 10-15 kPa range are typical of pathological conditions.

In general, the influence of substrate rigidity on the functionality of cultured hiPSC-CMs is still debated in literature. Li *et al.*, in their review, state that the 10-50 kPa range is the optimal value to recapitulate *in vivo* conditions and guarantee maturation of ventricular myocytes; Ahmed *et al.*, in their study, report evidence of cell contractility on

poly(dimethyl siloxane) (PDMS) substrates with Young's modulus of 6-10 kPa.[100,112] Querceto *et al.* have recently reviewed the literature on this matter agreeing that, even though there is not a marked tendency linking cell functionality (evaluated as cell shortening, calcium transient amplitude and CM shape) and substrate stiffness, 2D scaffolds with myocardial-like Young's modulus lead CMs to retain physiological morphology, structure and force generation capability.[116] Ribeiro *et al*., in their research work, elucidate how force generation is impaired on substrates with pathological-myocardium-like stiffness (35 kPa).[117] However, there are examples in literature of fully functional CMs cultured on substrates outside the physiological range of Young's modulus. Carson *et al.*, in their research work, cultured hiPSC-CMs on polyurethane-acrylate (PUA) patterned substrates, following a work published by Macadandang *et al.*; this polymer possesses a Young's modulus of 6.7 MPa, well outside the physiological range.[113,118] Martella *et al.* reported adhesion, growth and maturation (elongation and beating) of hiPSC-CMs on a LCE prepared via photopolymerization of acrylate-ended monomers.[73] In the work by Kim *et al.* on nanopatterned surfaces mentioned above, the elastic modulus of the PEGDA substrate is reported to be 70 MPa.[103]

In the research work that is presented here, conducted in collaboration with dr. J.M. Pioner at the Division of Physiology of the Department of Experimental and Clinical Medicine at the Università degli Studi di Firenze, hiPSC-CMs were cultured onto nanopatterned PEGDA substrates with different stiffness values, tuning the rigidity of the network by adding as a comonomer di(ethylene glycol)-diacrylate (DEGDA) in different percentages, to study the influence of substrate rigidity on the functionality of hiPSC-CMs. This study goes in the direction of determining the correct conditions to grow such hiPSC-CMs to full maturity and with the proper characteristics to *in-vitro* model cardiac tissue. Modelling hiPSC-CMs using biomimetic substrates may serve as a paradigm for elucidating aspects of cell-substrate (or ECM) interaction. Similar principles of cell-instructing substrates could also be applied to other cell types of interest.

3.1.2 Results and discussion

To assess the influence of the rigidity of the substrate on cell functionality, hiPSC-CMs were cultured onto micropatterned hydrogels composed of a blend of PEGDA and a comonomer, di(ethylene glycol)-diacrylate (DEGDA), after 20 days post differentiation (p.d.). The former is constituted by oligomers of ethylene glycol (average number of units is 250) capped with two acrylate ends; the latter has a shorter flexible spacer composed of a dimer of ethylene glycol with acrylate groups at both ends. Varying the ratio between the two components affects the number of crosslinks between the chains, and thus the Young's modulus of the hydrogel. Increased amount of DEDGA is expected to lead to higher mechanical modulus due to the increased concentration of acrylate units in the monomer mixture. Different mixtures (Figure 3.1) were prepared, all of them with 1% w/w photoinitiator (molecule **IN1**) to polymerize the monomeric mixture under irradiation with UV light at 385 nm: PEGDA (molecule **1**) only, DEGDA (molecule **2**) only, blends of the two components in various ratios.

To ease the notation, "DA" is omitted in the figures, so that "PEG" stands for PEGDA and "DEG" stands for PEGDA.

Patterning was obtained through soft lithography, a widely used technique to fabricate patterned surfaces. In brief, a replica of the surface pattern that has to be printed on the surface was fabricated using poly(dimethyl siloxane) (PDMS), which has a low surface energy and does not stick to the surface of the polymer to be patterned, thus guaranteeing high replicability and little-to-no damage to the surface when the PDMS mold is peeled off.[119] To promote adhesion of the hydrogel to the glass slides, these were functionalized with a modified methacrylate-ended silane, exploiting silicon chemistry (*silanization*).[120] The details of the cell culture protocol, fabrication of silicon master and PDMS mold and glass slide functionalized are further discussed in the experimental section.

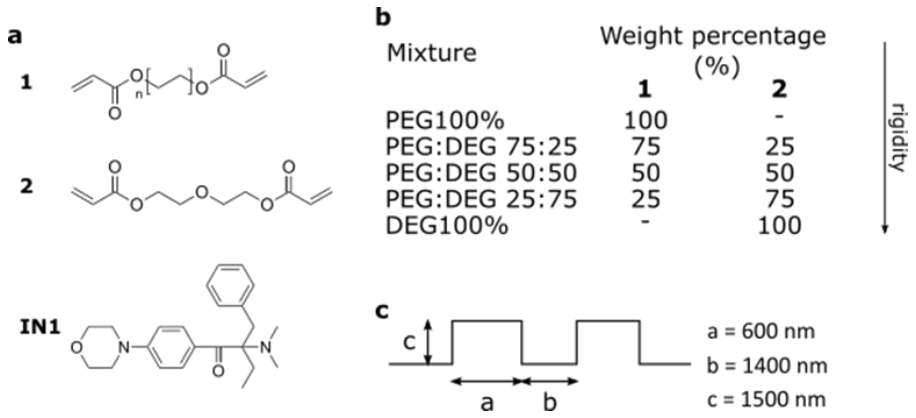

*Figure 3.1: Mixtures used for the preparation of the micropatterned hydrogels for cell growth. (a): Molecules used throughout the experiment. (b): Weight percentages of PEGDA and DEGDA (molecules **1** and **2**, respectively) in each monomer mixture. (c): Scheme of pattern topography.*

The effect of pattern spacing on cell growth was studied in previous literature works and by our research group.[103,109,121] Keeping the spacing between lines the same throughout the experiment (Figure 3.1c), the amount of molecule **2** in the polymer network was changed. The reference condition was constituted by hiPSC-CMs on cultured on the hydrogel composed of PEGDA (molecule **1**) only. All data were compared with the results from cells cultured on PUA, a rigid substrate that is widely employed in cell cultures of hiPSC-CMs.[109,113] Changing the amount of **2** in the hydrogel mixture affects substrate rigidity, which increases as the content of DEGDA gets higher in the mixture. The physical quantities used in this study to compare the functionality of cells cultured on different substrates are calcium transient (CaT) amplitude and cell shortening upon stimulation. The former is obtained via an experiment in which the amount of Ca^{2+} that increases in the cell cytoplasm and is released after the contraction is measured through fluorescence microscopy and calcium-indicators. Calcium ion is important in mediating contraction in muscle cells, and acts as a chemical signal. In adult cardiomyocytes the higher the CaT amplitude, the stronger is the contraction. In the case of hiPSC-CMs, the development of calcium dynamics is also associated to an increase in cell contractility. In this set of experiments, cell fractional shortening is calculated as the ratio between the lengths of a cell before and after contraction, thus reflecting hiPSC-CM contractile properties (maximal shortening and kinetics of contraction). Cell shortening is directly

related to the generated force upon stimulation when cells contract. The two experiments were conducted simultaneously. All experiments were carried out at 37 °C and at external [Ca^{2+}] = 1.8 mM.

CaT amplitude was measured using a calcium-sensitive dye, that binds Ca^{2+}. The amplitude is proportional to the fluorescence of the dye; the higher the signal from the calcium-binding dye, the higher the calcium content. It can be observed how there is little difference in average CaT amplitudes of cultured cells when up to 75% w/w DEGDA is added to the PEGDA hydrogel. CaT amplitude experiences a significant variation when the substrate is composed of DEGDA only, a condition in which cells show CaT amplitude values that are comparable to cells cultured on PUA. CaT amplitude increased as crosslink density got higher, confirming the influence of the rigidity of the substrate on cell maturation. Moreover, a qualitative analysis of the sample traces reported shows how the kinetics of calcium handling become faster at increasing rigidity (Figure 3.2).

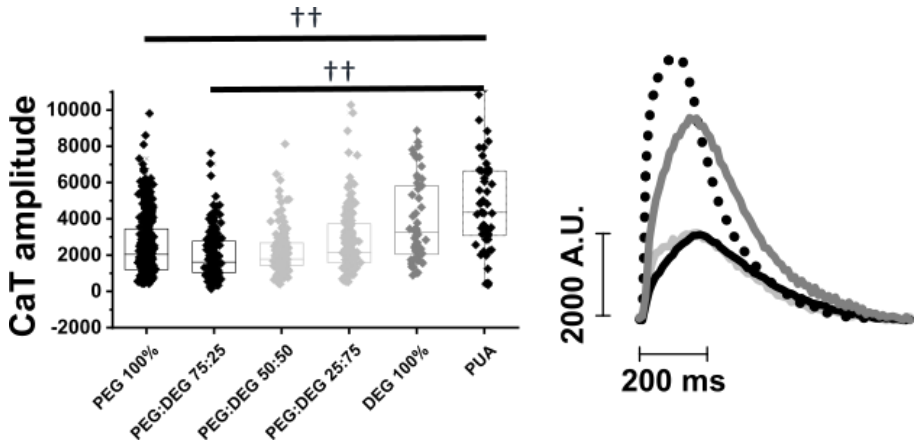

Figure 3.2: Impact of substrate rigidity on hiPSC-CM calcium transient amplitude. Right: CaT amplitude at day 60 p.d. as a function of crosslinker concentration in the hydrogel, compared to a substrate in PUA with the same linear micropattern. Left: representative CaT profiles at day 60 and of CaT amplitude. For PEGDA substrates, N=3 and n=336; for PEGDA:DEGDA 75:25, N=2 and n=150; for PEGDA:DEGDA 50:50, N=2 and n=147; for PEGDA:DEGDA 25:75, N=2 and n=150; for DEGDA, N=2 and n=50; for PUA, N=2 and n=5.

Cell fractional shortening, expressed as a percentage of the initial cell length, is reported for hydrogels composed of either PEGDA or DEGDA, since these two extreme

conditions only show a significant change in this parameter (Figure 3.3). These experiments confirm the results previously commented for the CaT amplitude measurement, since the more rigid the substrate the higher the percentage shortening in the cell, and thus a better performance of the cells during contraction. This analysis further supports the hypothesis that hiPSC-CMs prefer more rigid substrates to develop a fully mature functionality.

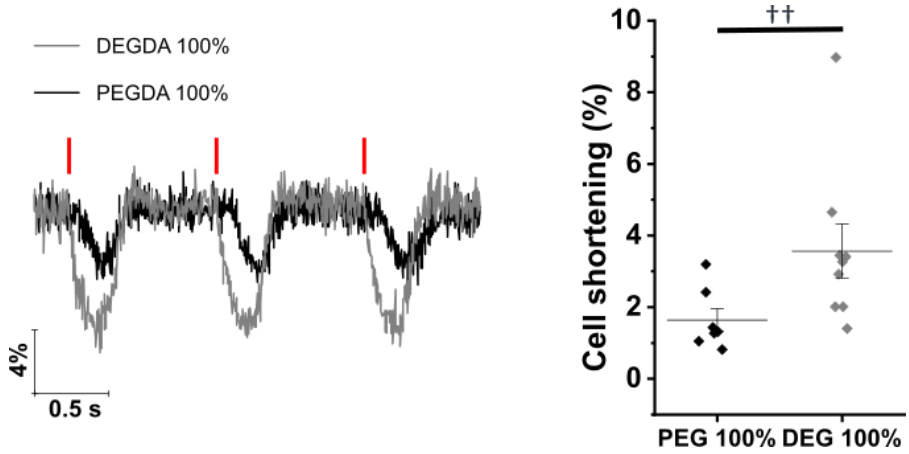

Figure 3.3: Cell fractional shortening of control-CMs on PEGDA and DEGDA-based micropatterned surfaces. Values of cell contractility at 1 Hz pacing are expressed as percentage of shortening from relaxed cell length. For PEGDA substrates, N=2 and n=7; for DEGDA, N=2 and n=7.

Thus, micropatterned substrates with tunable stiffness seem to impact hiPSC-CM adaptation and influence their maturation. In particular, both calcium transient dynamics and cell contractility progress towards a more adult-like cardiomyocytes. However, the gap between hiPSC-CM maturational stage and adult cardiomyocyte characteristics is still far; novel technologies, that may combine biomaterials and growth factors in culture, may help to reduce this distance in further developments of this research.

3.1.3 Experimental section

The preparation of the polymer substrates followed a four-step procedure, depicted in Figure 3.4. Biological experiments were performed in the laboratories of dr. J.M. Pioner, dr. R. Coppini and dr. C. Ferrantini at the Università degli Studi di Firenze. The silicon

masters were kindly provided by dr. F. Ferrarese Lupi and dr. L. Boarino at the Istituto Nazionale di Ricerca Metrologica (Torino, Italy).

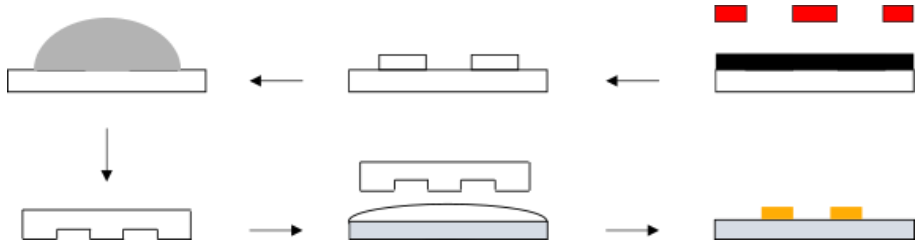

Figure 3.4: Preparation of the micropatterned PEGDA-DEGDA hydrogel for hiPSC-CM culture. The silicon master was patterned via UV mask (red) lithography on a commercial resist (black), then the pattern was replicated using a commercial PDMS mixture (grey). The PDMS mold (white) was then used to pattern a PEGDA-DEGDA mixture (with 1% w/w photoinitiator) to obtain the micropatterned hydrogel (orange) on a silanized glass slide (grey).

Fabrication of the silicon master. Masters were prepared via UV lithography (μPG101 laser writer, 800 nm resolution, Heidelberg). A photoresist (AZ1505, Merck Performance Materials GmbH) was spun onto a silicon wafer, with an area of 2 cm x 2 cm, and exposed to a mercury lamp equipped with a notch filter (with λ=365 nm as emission wavelength) irradiating the resist through a photomask to give the desired pattern. After irradiation, the samples were developed for 30 s in a 1:1 solution of AZ Developer (Merck Performance Materials GmbH) in water and rinsed in deionized water for 120 s.

Fabrication of the PDMS mold. A commercial PDMS elastomer kit (Sylgard 184, Sigma Aldrich) was used to fabricate the mold. It contained two components, respectively named *base* and *curing agent*, that were mixed in a 10:1 w/w ratio. After thorough mixing, the mixture was degassed in a vacuum desiccator to remove air bubbles. Then, the mixture was poured onto the silicon master, and the master with the PDMS mixture on top was degassed again. The PDMS was cured for 1h in oven at 100°C and gently peeled off the master afterwards.

Glass slides treatment. In Figure 3.5, the glass slide treatment to promote the adhesion of the polymer to the substrate is sketched. To enhance adhesion of the PEGDA/DEGDA hydrogel to the glass slides, glass slide surface was functionalized with a methacrylate-modified silane. The surface of the glass slides was activated by washing them in alkaline

piranha solution (5:1:1 v/v mixture of distilled water, aqueous ammonia 30% w/w in water and hydrogen peroxide solution 30% w/w in water at 75°C) for 15 min. After washing, slides were washed in water and isopropanol and dried with an air gun. The activated slides were immersed in a 0.064 M solution of 3-(trimethoxysilyl)propyl methacrylate (MAPTMS) in ethanol for 90 min. Afterwards, slides were washed in isopropanol and dried in oven at 100°C.

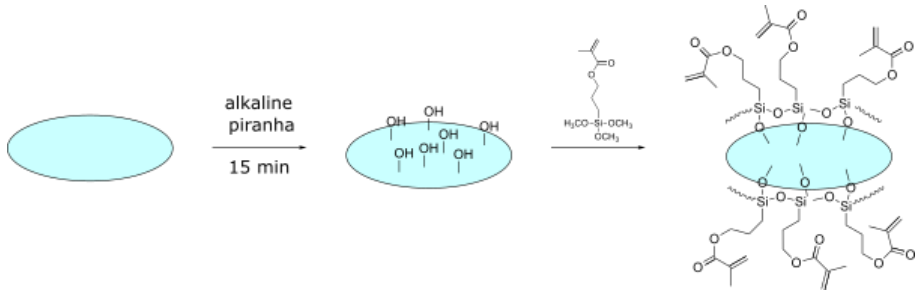

Figure 3.5: Glass slide treatment. Slides are treated with alkaline piranha to activate their surface and made react with MAPTMS to silanize the hydroxy- groups on the surface.

Fabrication of the micropatterned PEGDA-DEGDA hydrogel. PEGDA and/or DEGDA were mixed at different mutual ratios (in weight) with Irgacure 389 photoinitiator at 1% w/w concentration. A small amount (20-50 μL) was poured on the treated glass slide, and the mold was put on the drop. The monomeric mixture was irradiated with a UV lamp (M385L2-C4, Thorlabs) for 10 min through the patterned mold. After photopolymerization, the PDMS mold was peeled off, leaving the hydrogel with the linear pattern; after washing in water and isopropanol and drying with an air gun, it was ready to be used again. In Figure 3.6 two scanning electron microscopy images of the linear patterns obtained are shown.

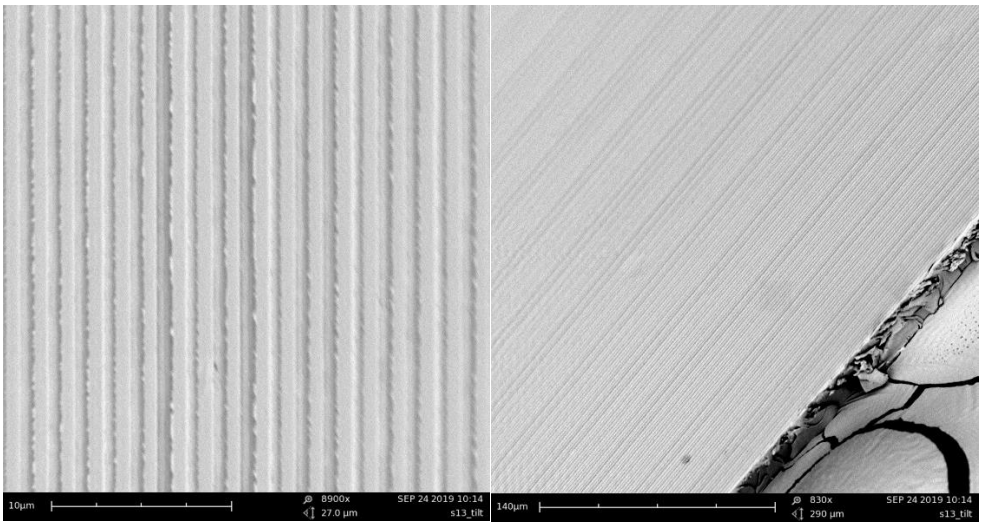

Figure 3.6: Scanning electron microscope photograph of the PEGDA-based patterns obtained through soft lithography from PDMS mold. The scale bar in the left-hand-side image is 10 µm, while in the right-hand-side one is 140 µm.

Biological experiments. The isolation of human cells and the subsequent reprogramming into iPSC lines was performed in compliance with the Declaration of Helsinki. Cells were harvested from urine, reprogrammed into hiPSC and differentiated into hiPSC-CMs as described in previous works from our collaborators.[4]

In brief, at day 20 p.d. on the appropriate differentiation substrate, single cells were obtained via enzymatic dissociation and cultured on the micropatterned hydrogels at the density of 20,000 cells/cm^2 (Figure 3.7). Recording of calcium transients was carried out at day 60, 75 and 90 p.d., loading the cells with 2 µL/ml of Cal630 (AAT Bioquest, Sunnyvale, CA, USA) and 5 µL of Power Load™ concentrate (Thermo Fisher, Waltham, MA, USA) for 30 min at 37 ◦C and then washing with pre-warmed culture media before placing the cover slide into the experimental chamber.

The experimental chamber possessed platinum electrodes, for electrical field stimulation, connected to a stimulator (DigiTimer, Welwyn Garden City, UK), which delivered short (3 ms) voltage pulses. During measurements, cells were continuously perfused with heated Tyrode buffer to keep the temperature stable at 37 ± 1 °C. For fluorescence studies, cells were illuminated with a LED light at 580 nm for Cal630 dye excitation. A band-pass filter (Semrock) was used to allow fluorescence light from the

dye to be collected by a camera (Photometrics Prime sCMOS), allowing red light in the 615-655 nm region (emission of Cal630).

Molecular Devices MetaMorph software was used to collect and analyze fluorescence in images. The camera collected images at an average rate of 90 frames per second. In each study, the desired number of single hiPSC-CMs was selected and chosen as region of interest. The background-corrected average fluorescence values from the pixels in each selected region of interest (myocyte) were recorded at the emission wavelength, under different stimulation conditions. For the analysis of calcium transient during steady-state stimulation, the average of 5-10 subsequent CaT traces was calculated to reduce noise.

Data are reported as mean ± standard error of the mean; one-way analysis of variance (ANOVA) was conducted on the data, using a Tukey post-hoc test with statistical significance set at $p < 0.05$ (†) and $p < 0.01$ (††) to assess the differences among the various data sets; *NS* stands for "non-significant". In each set, *N* is the number of differentiations and *n* is the number of cells. Data are represented as a box plot reporting the median and first and third quartile.

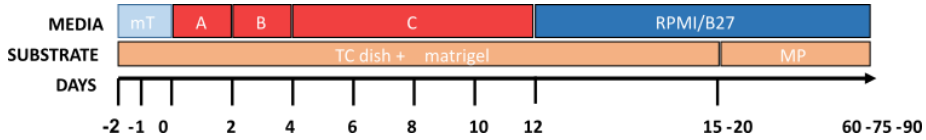

Figure 3.7: Cell culture protocol. Time course of media (mT mTeSR+suppl.; A+B+C cardiac differentiation kit) and substrates (TC: tissue plate; MP: hydrogel micropatterned substrates). The image is a kind courtesy of dr. J.M. Pioner.

3.2.The importance of shape-changing materials in tissue engineering and the use of Liquid Crystalline Elastomers as cell scaffolds

One of the newest interests in the use of SMPs in biomedical engineering is the fabrication of stimulable cell scaffolds, to take advantage of the shape-changing properties of the materials in order to provide cell cultures with a dynamic environment, similarly to the biological one.[66]

In this sense, LCEs display a degree of stimulability that is not easily achieved by other soft systems (as previously discussed for their use as artificial muscles), also exhibiting a set of desirable properties to be used to host cell cultures. Their rigidity is easily tunable, functionalization of their surface and bulk is possible, and a plethora of fabrication methods are available to prepare substrates with different architectures.
The field is not extensively reviewed, since the applications of LCEs in the biological and biomedical fields represent the cutting edge of LC science.[8,53,77].

3.2.1 Introduction

The presence of LC ordering in cell cultures and in biological systems could constitute one of the main factors underlying the demonstrated biocompatibility of certain classes of LCs and LCEs. Besides this important characteristic, through the years LCEs have demonstrated their potential to outperform the currently used synthetic materials to host cell cultures and offer them a biomimetic environment during the growth process: they are biocompatible, they direct cell alignment (the exact mechanism is still to be unveiled, but contact guidance is the most valued hypothesis) and their shape-changing properties have been harnessed to fabricate cell scaffolds capable of continuous mechanical stimulation to cultured cells. These last two phenomena have been studied in the last five-seven years and made LCEs potential candidates for the next breakthrough in tissue engineering as active cell culture substrates. Some examples are reported here to trace the state of the art of this application of LC substances (Figure 3.8).
Seminal works Luk *et al.* and by Lockwood *et al*. disclosed the role of LCs in cell cultures. The former assessed the cytotoxicity of different classes of LCs, finding that widely used cyanobiphenyl derivatives are highly toxic, while cholesteryl derivatives and fluorinated mesogens proved not to be cytotoxic.[122] The latter studied the effect of LC ordering on a cell culture of human embryonic stem cells, fabricating a support composed of a fluorinated mesogen mixture coated with a protein-based gel for cell cultures: they found that the appearance of the LCs under POM observation changed over time, thus determining reorganization of mesogens induced by the cell culture.[123]

The first example of a LCE used as a cell scaffold dates to 2015. Sharma *et al*. designed a multi-arm block copolymer with an azide functional group to bind, in a subsequent step, a modified biocompatible cholesteryl derivative equipped with an alkyne-terminated chain via CuAAC reaction. It resulted in a SmA LCE that was crosslinked via ring-opening metathesis and presented an intrinsically porous microstructure. Its biocompatibility to neuroblastoma cell line (SH-Sy5Y) and C2C12 myoblasts was demonstrated.[34] A similar approach was used in a later work by Prévôt *et al*., who exploited ring-opening metathesis to obtain a chlorine-bearing polymer, which was subsequently functionalized with an azide moiety to exploit again CuAAC to attach a cholesteryl group to the polymer backbone. The LC polymer was mixed with a diisocianate crosslinker and a template salt; crosslinking reaction via urethane bond formation was performed in a second step. The process led to the preparation of an LCE-based foam, after salt leaching in water. Its biocompatibility and biodegradability were assessed, and the foam proved to be able to host a neuroblastoma (SH-Sy5Y) cell culture.[76] Thiol-ene chemistry, as discussed in the first chapter of this work, is another feasible strategy to fabricate MC-LCEs. The biocompatibility of these materials towards L929 fibroblasts was evaluated by Yakacki *et al*. in their work on monodomain MC-LCEs obtained via this synthetic route and aligned through two-step Finkelmann's method.[124] This seminal paper paved the way to the use of thiol-ene-based LCEs to fabricate intervertebral discs replacements and biocompatible LCE-based foams, as presented by Shaha *et al*. in 2020. They exploited the different mechanical properties exhibited by monodomain and polydomain LCEs, to fabricate a biomimetic dual layer device.[125]

The first example of cell-instructiveness of a substrate with LC alignment can be found in a paper by Kirkwood and Fuller dating to 2009, who cultured human fibroblasts on films of collagen that displayed banding typical of cholesteric LCs. This structural organization resulted in a high degree of alignment exhibited by the cultured cells, which followed the guidance offered by the linear pattern.[126] Low-molecular-weight mixtures of reactive LCs were exploited by Martella *et al*., who demonstrated cell-instructiveness of planarly-aligned films in different cell lines, such as murine C2C12 myoblasts, human

dermal fibroblasts (HDFs) and hiPSC-CMs.[74,127] The ability to help differentiation of skeletal muscle cells into myotubes was demonstrated in a paper disclosed in 2021.[128] HDF self-organization on planarly aligned films of LCNs was also studied by Turiv *et al*. They pinpoint the presence micrometric features that help the alignment of the seeded cells due to the anisotropic swelling in the culture medium experienced by the LCN.[129]

Stimulability and shape-changing properties of LCEs have been used to mimic the mechanical signaling offered by our body to cells in other works with successful outcomes. Agrawal *et al*. developed a LCE-nanocarbon composite, using siloxane chemistry and two-step alignment. The addition of carbon black nanoparticles resulted in an enhancement of the electrical conductivity of the material, capable of 3% strain under 40 V electrical stimulus. Neonatal rat ventricular myocytes were cultured on these electrically active substrates, which proved to be biocompatible with and without paced stimulation.[75] Koçer *et al*. and Hendrikx *et al*. assessed the biocompatibility of NIH3T3 fibroblasts on two types of light-responsive reconfigurable surfaces obtained through photopolymerization of low-molecular-weight acrylate-ended reactive mesogens. [130,131] This approach will be examined in depth in the next part of this chapter.

Latest applications of LCEs as cell culture substrates explored the use of nanogrooves originated by the self-assembly of smectic mixtures on planarly-aligned substrates and the use of complex directionalities induced by photoalignment of reactive mesogens (such as circular alignment). These systems proved to be biocompatible, respectively, to HDFs and A172 glioblastoma cells.[132,133]

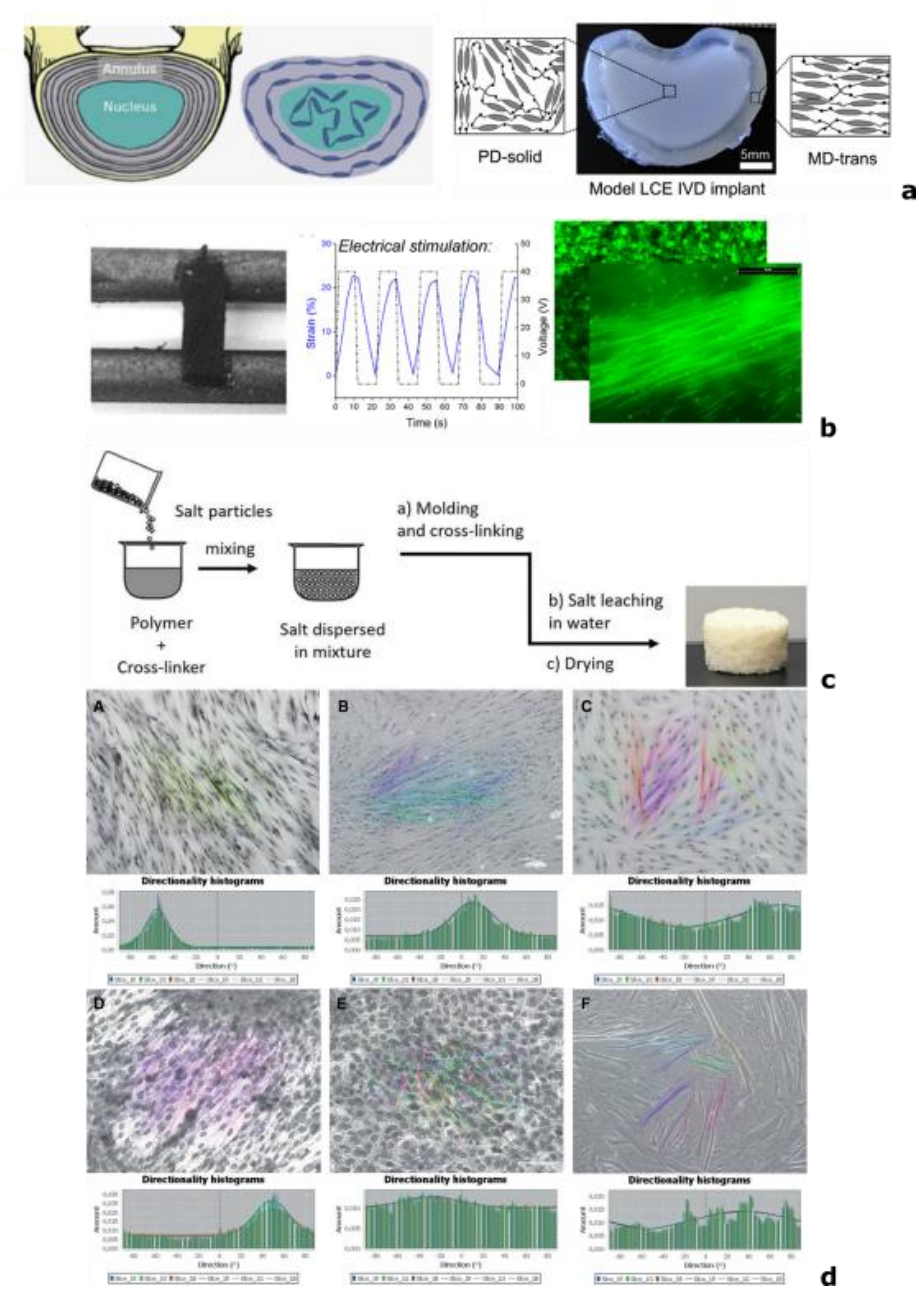

Figure 3.8: Different examples of LCEs as cell scaffolds. (a): Biomimetic intervertebral disc replacement based on a polydomain LCE that simulates the nucleus of the disc and external aligned layer which mimics the annulus. Adapted from ref. 125*. (b): Electrically stimulable LCE-nanocarbon composite, capable of uniaxial stretching upon stimulation, that support neonatal rat ventricular myocyte cultures. Adapter from ref.* 75*. (c): Fabrication process of a LCE-based foam for cell cultures of neuroblastoma cells. Adapted from ref.* 76*. (d): LCE-induced cell alignment for HDFs (top) and murine C2C12 myoblasts (bottom).*

Leftmost and center columns contain the orientation map and directionality histograms for cell cultures on LCE-based films at different crosslinker concentrations (respectively 20% mol/mol and 10% mol/mol), to be compared on the same cell lines cultured on standard Petri dishes, in the rightmost column. Cell-instructiveness is demonstrated, and the effect is rigidity-dependent, showing the superiority of the most rigid LCE compared to standard cell culture substrates and a softer LCE in aligning cells. Adapted from ref. 73.

3.2.2 Use of a reconfigurable LCE-based surface for cell growth

The roots of the research work presented here lie in the studies carried out by our research group on topographical cues to enhance cell growth and alignment of hiPSC-CMs and in the possibility to prepare reconfigurable surface patterns exploiting, firstly, the shape-changing behavior of LCEs and, secondly, their desirable properties at the interface with biological systems discussed so far. As previously mentioned, Koçer *et al*. and Hendrikx *et al*. studied the effect of reconfigurable surfaces on cell adhesion and migration, using a LC polymer system (with a different surface topography) which is very similar to the one that will be presented in this research work.[130,131] In the first of the two cited articles, the biocompatibility of pillared LCE coatings (obtained through photopolymerization of acrylate-ended mesogens) towards NIH3T3 fibroblast was assessed. In another study, the authors demonstrated the ability of these pillared surfaces in influencing cell motility and migration speed. Plus, they showed how cells seeded on top of the polymer remained viable even after illumination of surfaces from the bottom with UV light, paving the way to the use of such coatings to live stimulation of cells. Indeed, after irradiation and, thus, surface change towards a rougher state compared to the initial one, cells showed a lower motility.

The aim of the present study was the preparation of active cell culture substrates based on fingerprint-like stimulable patterns originated by cholesteric LCs on homeotropically aligning coatings. The stimulable scaffolds were developed in collaboration with prof. D. J. Broer and dr. D. Liu at the Stimuli-Responsive and Functional Materials and Devices (SFD) research group at Eindhoven Technical University. The reconfigurable surfaces were prepared using cholesteric reactive LC mixtures, able to give rise to worm-like patterns with height modulation under homeotropic anchoring.

The rise of fingerprint textures is due to the sum of two effects: homeotropic anchoring of cholesteric LCs and Marangoni effect. Regarding the former, chiral nematic LCs often align with the helix axis perpendicular to the substrate; on the other hand, if a strong homeotropic anchoring is provided (through one of the earlier proposed methods, such as surface effect mediated by an aligning coating), the helix axis is brought parallel to the substrate, enabling modulation of the different alignments along the length of a cholesteric pitch. The rotation of mesogens along the helix, indeed, makes it possible to alternate zones with planar, tilted and homeotropic alignment, showing a fingerprint-like texture.[134] The surface tension difference between these alternating zones promotes Marangoni effect, mass transport along a surface tension gradient. This phenomenon is responsible for the modulation of height in the coating; areas with homeotropic alignment exhibit *hills*, while planarly aligned zones are topographically lower in height, being *valleys*.[135,136] For fingerprint-like texture to be triggered in cholesteric LCs, an important geometrical constraint must be observed; since the rise of the pattern is linked to the tradeoff between homeotropic anchoring (whose interaction energy is distance-dependent) and the right alignment of the helix axis to the substrate surface, it is necessary that the condition:

$$0.3 < \frac{t}{P} < 0.5 \qquad \text{Equation 3.1}$$

where t is coating thickness and P is helix pitch, is respected. This non-dimensional parameter, indeed, takes into account both the LC properties of the mixture and the interaction energy between the aligning substrate and the mesogens, which decreases as the distance (and hence the thickness) increases. If the coating is too thick, mesogens will be unconstrained and a focal conic texture (typical of chiral nematic LCs) will be obtained; if the thickness is, on the other hand, too thin, the twisting force of the cholesteric helix will not be able to make the orientation of mesogens rotate, thus establishing homeotropic anchoring of the mesogens to the substrate (Figure 3.9).[134,136]

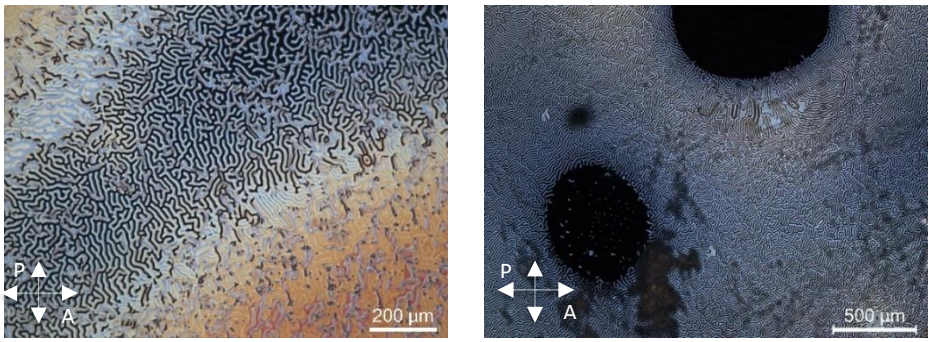

Figure 3.9: POM images of LC samples with fingerprint-like patterns, focal conic textures and homeotropically aligned zones. Left: transition from fingerprint pattern (central zone, low thickness) to focal conic texture (corners, thick zone of the sample) in an inhomogeneously covered sample. Right: coexistence of homeotropically aligned zones (black) and fingerprint pattern in a sample with inhomogeneous thickness.

Polymers obtained under radical-mediated conditions undergo a consistent shrinkage during polymerization reaction.[137] In the case of LCEs, anisotropic shrinkage of the network is observed, with up-to-6% contraction in the direction parallel to the director and 0.1% perpendicularly to molecular alignment.[9] In cholesteric LC systems with fingerprint-like texture, this anisotropy leads to the inversion of the topography during polymerization: hills become pits and valleys become protrusions, since the former shrink more than the latter during polymerization.[138]

To make LCE coatings light-responsive, a diacrylate azobenzene was added to the mixture. The actuation of azobenzene-doped fingerprint patterns takes into account different physical phenomena. Besides light-induced loss of order (which was mentioned previously when dealing with LC mixtures doped with azobenzenes), an important role is played by free volume effect, which is the creation of free voids in the polymer network which are needed to allow the motion of azobenzene molecules. Yager *et al*. studied this effect on linear side-chain polymers obtained via polymerization of Disperse Red 1 Acrylate, where they observed a 17%-shrinkage upon irradiation.[139] Liu *et al*. found a 10% density decrease in azobenzene-doped LCE when irradiated, further supporting the evidence of the importance of this phenomenon in the dynamics of LCEs.[135,140,141] Moreover, this effect can be controlled triggering simultaneous forward and backwards trans-to-cis photoisomerization of azobenzene, as demonstrated by Liu

and Broer.[142] Free volume creation and induced loss of order, thus, exert a concerted effect on the LC network, leading to the actuation of the fingerprint coatings. Moreover, being the free volume creation highly thermodynamically unfavorable, relaxation to the initial state is a faster process than back isomerization of azobenzene and LC ordering reorganization, since this process can also take several hours.

3.2.3 Results and discussion

Fingerprint-patterned LCE coatings were fabricated following the research work of Liu and Broer.[136] The composition of the different materials that were prepared throughout the study is reported in Figure 3.10; all mixtures contain 2% wt. photoinitiator **IN2**.
First, two nematic mixtures designated as **LCN3** and **LCN4** were prepared to fabricate unpatterned substrates with homeotropic and planar alignment. Then, their surface modification via the addition of the chiral dopant was carried out, preparing mixtures **LCN5** and **LCN6**. These monomer mixtures differed one another in the amount of chiral dopant **CL3**, and, thus, in pattern spacing. **LCN7** possessed a higher **D3** dye amount than **LCN5-6** (8.21% wt.), while retaining the same **CL3** amount as **LCN6**. The actuation of the samples was characterized, along with their biocompatibility towards HDF and murine C2C12 myoblast lines.

Fabrication of nematic LCE coatings and biocompatibility assessment

The difference between **LCN3** and **LCN4** mixtures lied in the presence of the azobenzene dye **D3**. The first experiments had the objective to assess the biocompatibility of planarly and homeotropically aligned LCEs fabricated with monomers **M2**, **M3** and **CL2**, to be used as a reference for the subsequent studies on fingerprint patterns, and if the presence of dye **D3** affected their ability to host cell cultures.

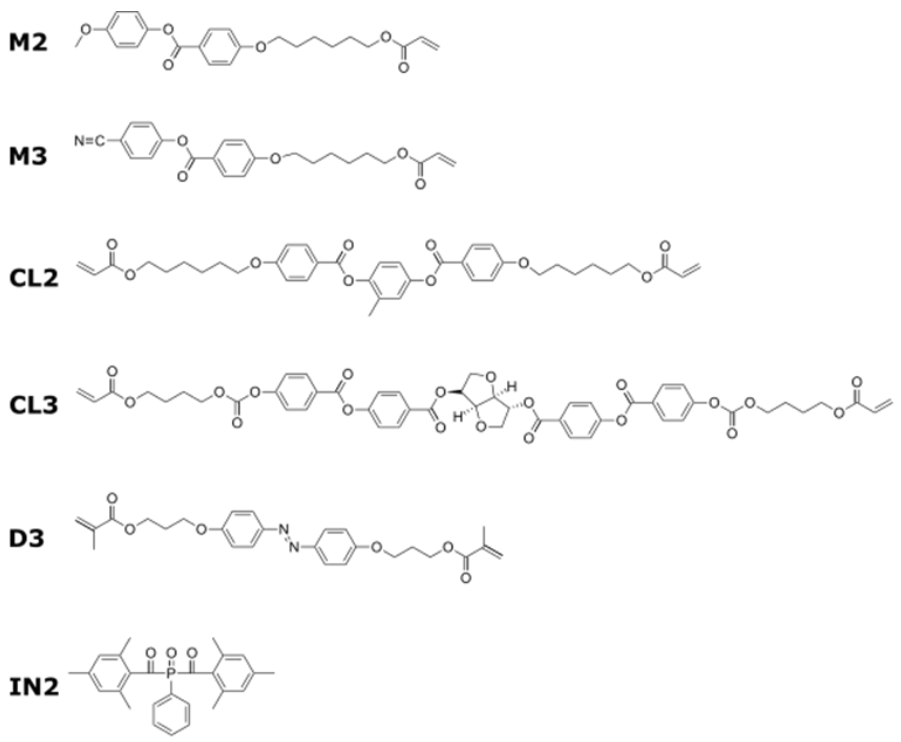

Weight percentage (%)

	LCN3	LCN4	LCN5
M2	44.57	44.57	44.57
M3	31.50	31.50	31.50
CL2	21.93	19.93	19.50
CL3	-	-	0.43
D3	-	2.00	2.00

	LCN6	LCN7
M2	44.57	45.73
M3	31.50	32.32
CL2	19.64	11.39
CL3	0.29	0.29
D3	2.00	8.21

*Figure 3.10: Mixtures used throughout the work and chemical structures of the reagents. Top: chemical structures of LC and non-LC monomers (**M2**, **M3**, **CL2**, **CL3**), the dye (**D3**) and the photoinitiator (**IN2**). Bottom: on the right, chemical composition of the LCE-based materials. All mixtures **LCN3-7** contain 2% wt. of photoinitiator **IN2**. All mixtures were dissolved in various weight ratios in THF. In the inset on the left, the absorption spectrum of **D3** is shown (adapted from ref.* 143*).*

Samples from mixtures prepared without and with the azobenzene **D3** (respectively, **LCN3** and **LCN4**) were fabricated; the LC properties were not affected by the presence

of such a small amount of azobenzene dye. T_{NI} of the LC mixtures and T_g of the polymers were assessed through DSC: the former resulted to be 55.4°C, while the latter was 24.9°C. The information on the glass transition temperature of the polymer is important to evaluate its mechanical state in the culture conditions: at 37°C, the temperature at which cells are grown, the LC network was rubbery. Attenuated total reflectance infrared spectroscopy (ATR-IR) was used to confirm the complete polymerization of the network, through the quantitative evolution of the C=C stretching peak intensity (1604 cm^{-1}) and the intensity of the peak related to C=C-H out-of-plane bending of the hydrogen on the acrylate group (810 cm^{-1}). The intensities of both peaks were normalized to the intensity of the C=O stretching peak intensity at 1725 cm^{-1}. Both analyses gave an average degree of polymerization (DP) >90%. In Figure 3.11 it is possible to observe the complete disappearance of the peak at 810 cm^{-1} after the polymerization.

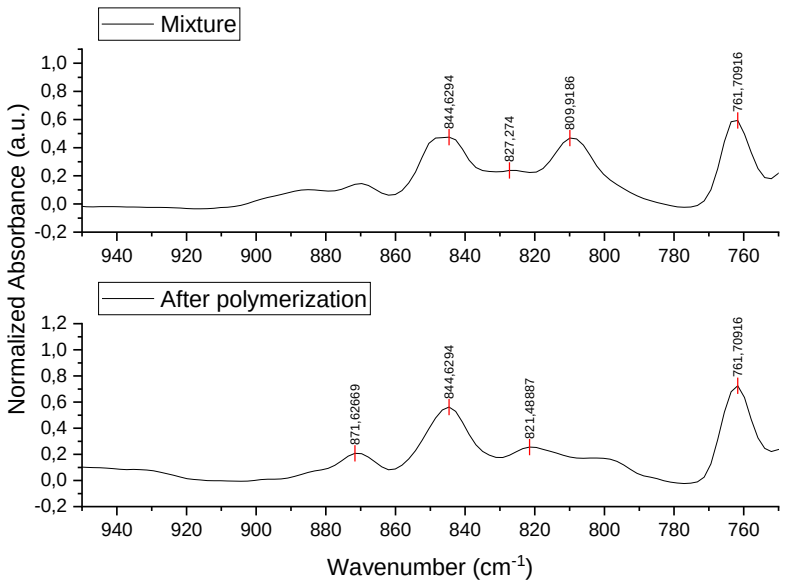

Figure 3.11: Representative DP calculation via the ATR-IR spectrum of the LCNs. A close-up of the interval between 950 cm^{-1} and 750 cm^{-1} is shown, to highlight the peak of the C=C-H out-of-plane bending of the hydrogen on the acrylate group at 810 cm^{-1}, which disappears after polymerization.

Alignment was checked via POM (Figure 3.12): for the homogeneous planar samples, the difference in transmittance between the two POM photos reported is indicative of the correct uniaxial alignment; conversely, no difference in transmittance was observed

for homeotropic samples when observed at 0° and 45° with respect to the axis of the polarizers, indicating that mesogens lie perpendicularly to the plane of the substrate as expected.

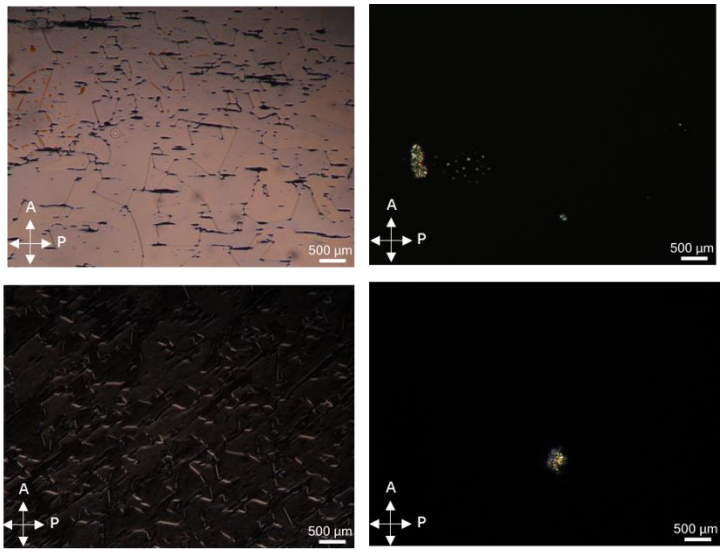

*Figure 3.12: POM photos of polymers obtained with **LCN4** mixture. Right: planarly aligned substrates, at 45° with respect to the polarizers (top) and aligned parallelly to one polarized (bottom). Left: homeotropically aligned substrates, at 45° with respect to the polarizers (top) and aligned parallelly to one polarized (bottom).*

The average thickness, confirmed by interferometry on substrates, was 4.45±0.28 µm for homeotropically aligned substrates and 5.21±1.22 µm for planarly aligned samples. Biocompatibility of nematic samples both without the azobenzene (**LCN3**) and with the dye **D3** (**LCN4**) was checked for HDFs and murine C2C12 myoblasts (Figure 3.13).

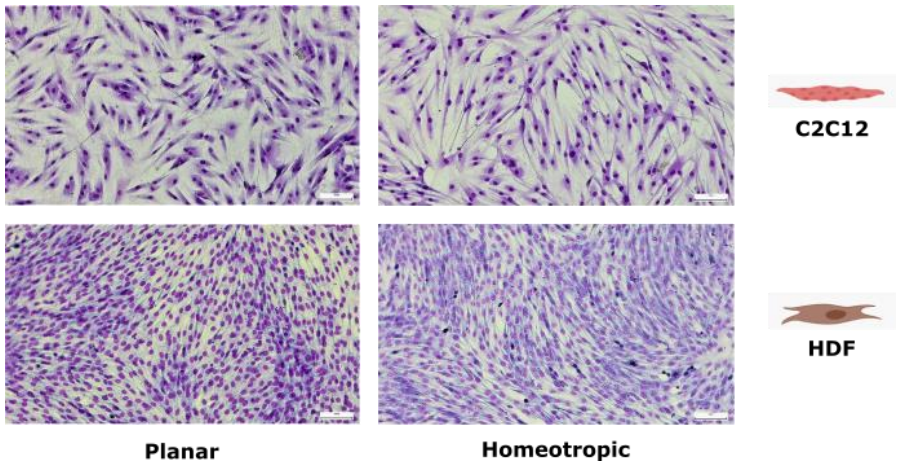

*Figure 3.13: Biocompatibility assessment for planar and homeotropic LCE coatings derived from **LCN4** mixture, equipped with **D3** azobenzene. No spatial organization induced by LC ordering was found.*

Cells cultured on LCE coatings obtained with **LCN4** mixture, equipped with the **D3** dye, proved to be biocompatible and capable of hosting both C2C12 and HDF lines, showing a high number of live cells after days of culturing similar to standard supports (e.g. Petri dishes).

However, no organization induced by LC alignment was observed. **LCN3**, without the azobenzene, proved to be biocompatible as well (photos not shown), even though also in this case no alignment of cells was observed in the cultures. Thus, **D3** azobenzene did not have any effect on the biocompatibility of the LCE coatings, but the two mixtures could not induce any spatial organization in cells.

Fabrication of fingerprint-patterned LCE coatings based on cholesteric LC mixtures with a low azobenzene amount

The nematic samples obtained with mixtures **LCN3-4** were then modified with the addition of the chiral dopant **CL3** in a small amount, to fabricate two types of fingerprint-patterned surfaces doped with 2% wt. **D3** azobenzene, preparing mixtures **LCN5** and **LCN6**.

It is worthy to remember that cholesteric pitch *P* is related to chiral dopant amount via the relation:

$$P = \frac{1}{HTP \cdot c}$$ Equation 3.2

where *HTP* is *helical twisting power*, and *c* is the concentration of the chiral dopant. *HTP* expresses the ability of a specific chiral dopant to exert a twisting torque on the nematic mesogens.[6,134] Thus, to modulate the spacing between the motifs (which were separated by half of cholesteric pitch distance *P*), two amounts of **CL3** were chosen on the basis of previous studies.[136] Surface roughness and pitch distance (and thus, chiral dopant amount) are intimately related and the two parameters vary altogether; the effect of the variation of chiral crosslinker concentration on pattern spacing and surface roughness was assessed, keeping the concentration of the other components in the mixtures unchanged (Figure 3.14).

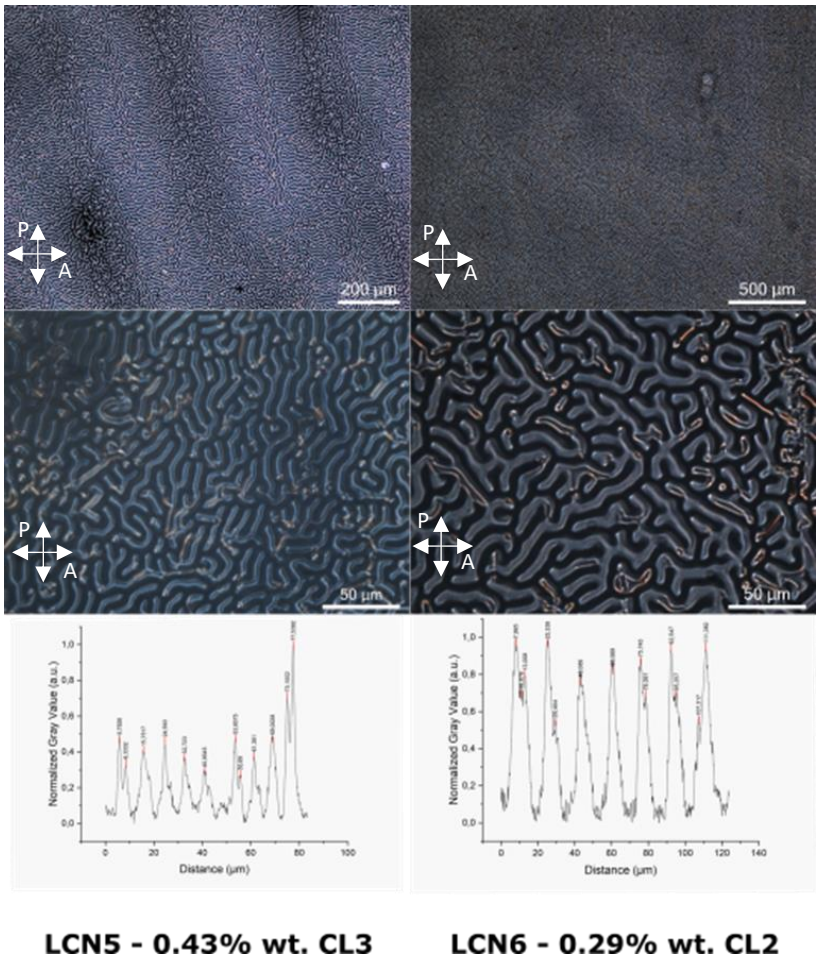

*Figure 3.14: POM images at different magnifications (top and center) and grey-value-to-distance plot (used to assess pattern spacing, bottom) of fingerprint-patterned surfaces obtained with different amounts of **CL3** chiral crosslinker. Left: **LCN5**, with 0.43% wt. **CL3**, had a mean pattern spacing of 8.52±0.57 µm. Right: **LCN6**, with a lower chiral dopant amount than the other mixture (0.29% wt.), had a mean pattern spacing of 11.37±1.02 µm.*

The modulation of chiral dopant concentration reflected itself on surface roughness (evaluated in the unactuated state as areal mean surface roughness S_a according to ISO 25178 norm, see the experimental section for a detailed definition) change (Figure 3.15). The LCE coating with the highest amount of chiral dopant, 0.43% wt. (**LCN5**), had the narrowest pattern spacing, 8.52±0.57 µm, and the lowest mean roughness, 18.07±0.01 nm. On the other hand, the mixture with the lowest amount of **CL3** (**LCN6**), 0.29% wt., exhibited a larger spacing than the previous one, 11.37±1.02 µm, and a more corrugated

surface in the unactuated state, with S_a of 33.17±1.72 nm. Thus, the lower is the amount of chiral dopant, the more corrugated is the surface and the less narrow is pattern spacing. The ratio between the thickness of the two coatings and cholesteric pitch (the double of the pattern spacing) respected the condition stated in Equation 3.1, being $d/P \approx 0.22$-0.24. The fabrication of the samples was carried out keeping the amount of azobenzene dye **D3** at 2% wt. in both mixtures.

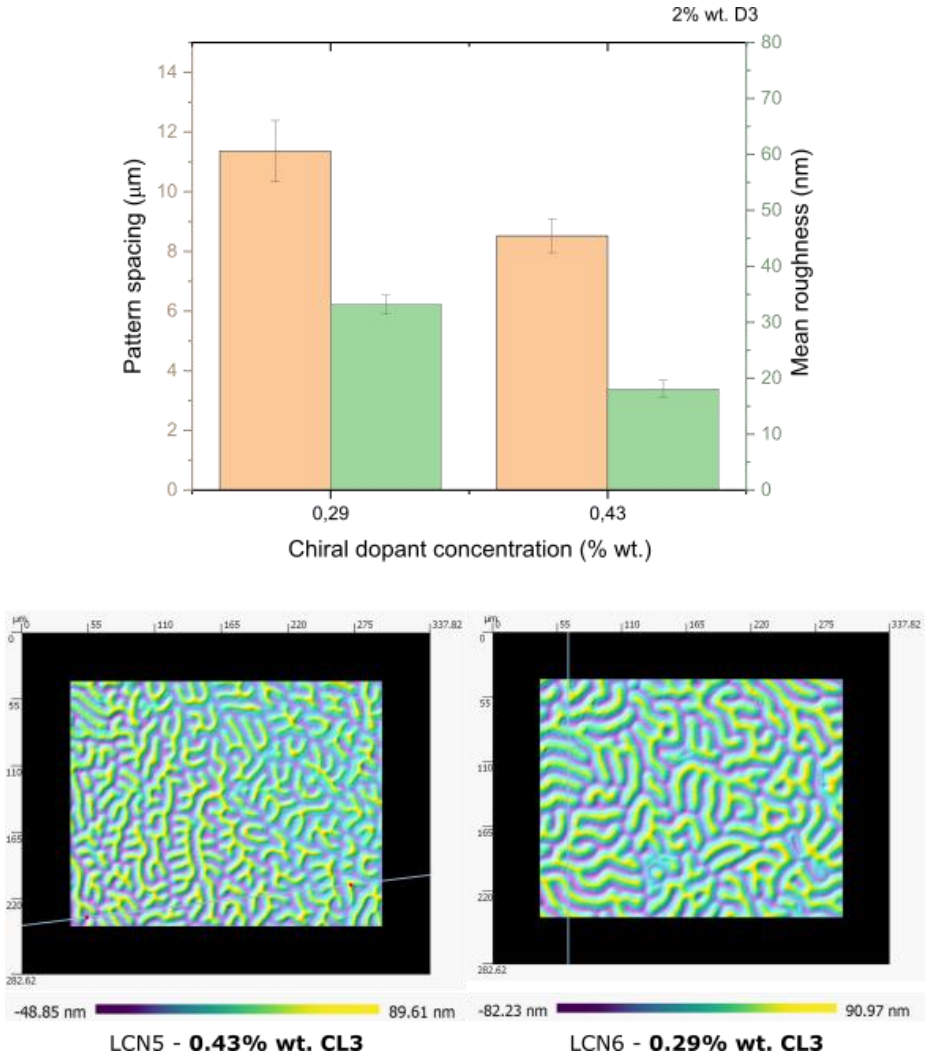

*Figure 3.15: Effect of chiral dopant concentration on mean surface roughness and pattern spacing, keeping **D3** dye amount fixed at 2% wt. Top: dependence of mean surface roughness (green bars) and pattern spacing (orange bars) on **CL3** amount. Bottom: sample confocal microscopy images of two LCE coating*

with different amounts of chiral dopant. The difference in the scale bars highlights the differences in the roughness of surface motifs.

Preparation and characterization of fingerprint-patterned LCE coatings with enhanced actuation properties

Samples with 2% wt. azobenzene in the network did not exhibit a marked actuation, evaluated as the displacement of two neighboring peak and valley summed up and normalized by the initial thickness of the sample (calculation of actuation is reported in the experimental section), when irradiated with UV light, since they displayed a percentage actuation of 0.54±0.10 % when irradiated for 60 s with UV light at 385 nm at 200 mW/cm^2.

Thus, **LCN7** material was prepared: it contained ≈8% wt. **D3**. Dye content was increased at the expense of **CL2** crosslinker amount; hence, its LC properties were slightly different compared to **LCN3-6** mixtures.

Substituting a diacrylate mesogen with a non-LC substance made T_{NI} decrease by 8°C (being 47°C for **LCN7**), and T_g change to 33°C (as confirmed by DSC). Despite this variation, the polymer was still rubbery at cell culture conditions (37°C). The amount of chiral dopant **CL3** that gave the most corrugated surface (0.29% wt.) was chosen to fabricate these samples with a higher dye amount. The percentage of dye was chosen to be the best compromise between the highest dye content possible, within the limits of its solubility in the LC mixture, and the mesogenic properties of the mixture, not to shrink the chiral nematic temperature range. Polymerization procedure was changed to raise mean surface roughness; exploiting **D3** dichroic properties, the first polymerization step was carried out at extremely low power for a longer irradiation time than previously (0.1 mW/cm^2 for 90 min for **LCN7**, as opposed to 10 mW/cm^2 for 10 min for **LCN3-6**) to trigger light-induced matter transport from planar areas to homeotropic ones.

It resulted in a 2.2-fold increase in mean surface roughness: **LCN7** had a S_a of 70.17±8.76 nm (compared to the previous value of 33.17±1.72 nm found for **LCN6**) preserving pattern spacing (which resulted to be 10.19±0.52 µm) and DP (always >90%) (Figure 3.16).

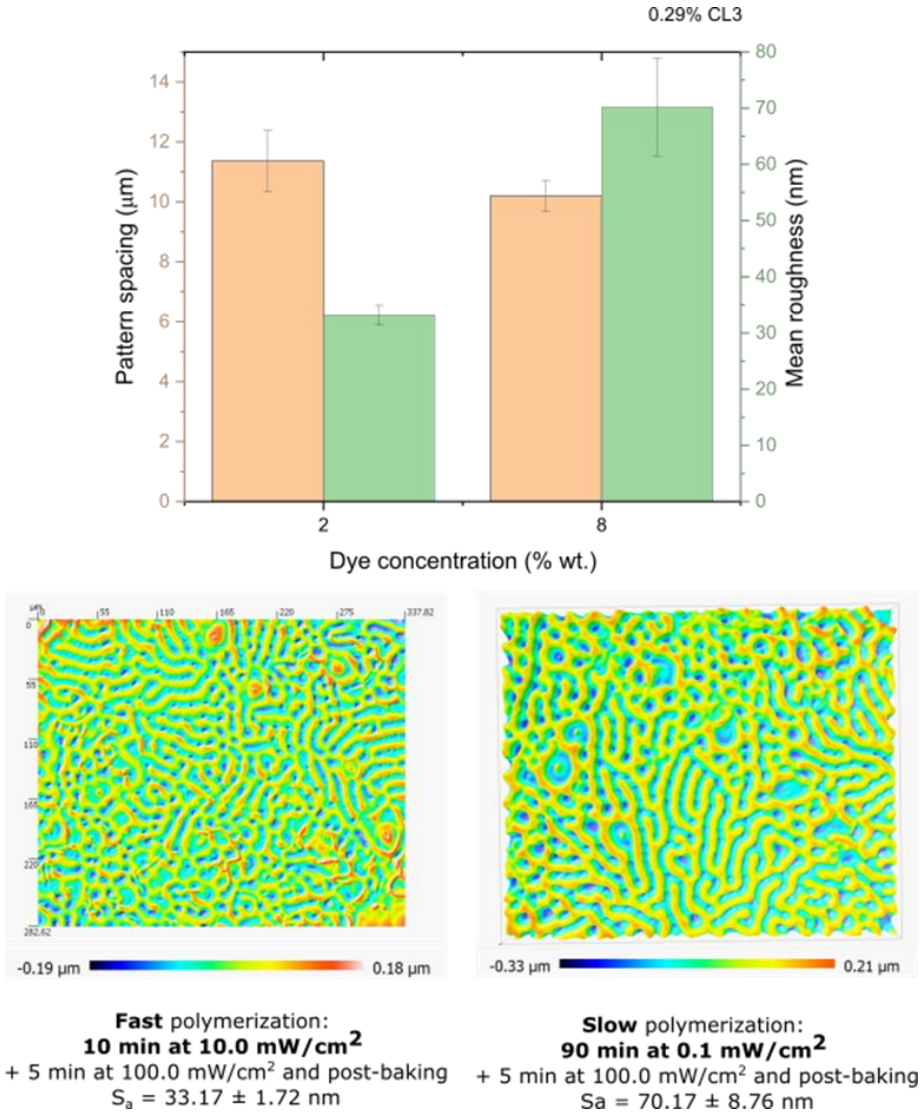

*Figure 3.16: Comparison between surface topographies of **LCN7** samples polymerized with two different procedures with different dye amounts, keeping the weight percentage of the chiral dopant fixed at 0.29% wt. Left: samples polymerized with the recipe used for samples from mixtures **LCN3-6**. The LCE coating is subjected to a high-power fast polymerization. Right: samples polymerized using low light intensity for a long irradiation time. The surface becomes more corrugated.*

LCN7 samples displayed a good light responsiveness, undergoing complete topography inversion when stimulated with UV light at 385 nm (Figure 3.17). Live actuation of a line profile (white line) and two neighboring surface corrugations (a peak and a valley close to each other enclosed in the white circle) was followed, under irradiation with UV

light at 385 nm at 200 mW/cm^2 and, subsequently, blue light at 455 nm at 90 mW/cm^2. Illumination with blue light only drives the reorganization of the surface to its initial profile, which can be observed in Figure 3.17a and Figure 3.17b.

During the experiment, UV light was first shone on the sample for 60 s, triggering topography inversion. Maximum of actuation was obtained within 5-10 s. To try to enhance actuation and further displacement of surface motifs downwards and upwards, the coating was irradiated with both UV and blue light (as reported by Liu) after UV stimulation in the first phase.[141] However, irradiation with 90 mW/cm^2 contemporarily to UV light at 200 mW/cm^2 did not have the effect of improving actuation pushing the topography inversion further, but instead it triggered a certain degree of shape recovery to the initial state, and an intermediate state between inverted and unactuated topography was observed. The third graph in Figure 3.17a shows the comparison between the sample irradiated with both UV and blue light and the same profile stimulated with blue light only: the fingerprint irradiated with two wavelengths, to trigger backwards and forward isomerization of azobenzene, generates a topography lying between the initial and the inverted state. The last graph, then, demonstrates the almost complete shape recovery upon irradiation with blue light only experienced by the LCE coating, and the reversibility of the actuation of the fingerprint pattern. An absolute value of >300 nm displacement was observed for both a peak and a neighboring valley under sustained UV irradiation for 60s, as reported in Figure 3.17b. In this graph, the effect of blue light is even more evident in the green region, where shape recovery begins as blue light is shone on the sample along with UV light (the just-created valley begins rising upwards again). Observing the evolution of the topography (Figure 3.17d), it is possible to see how surface topography experienced complete inversion, with peaks plunging and becoming valleys and pits becoming hills. The deformation is fully reversible.

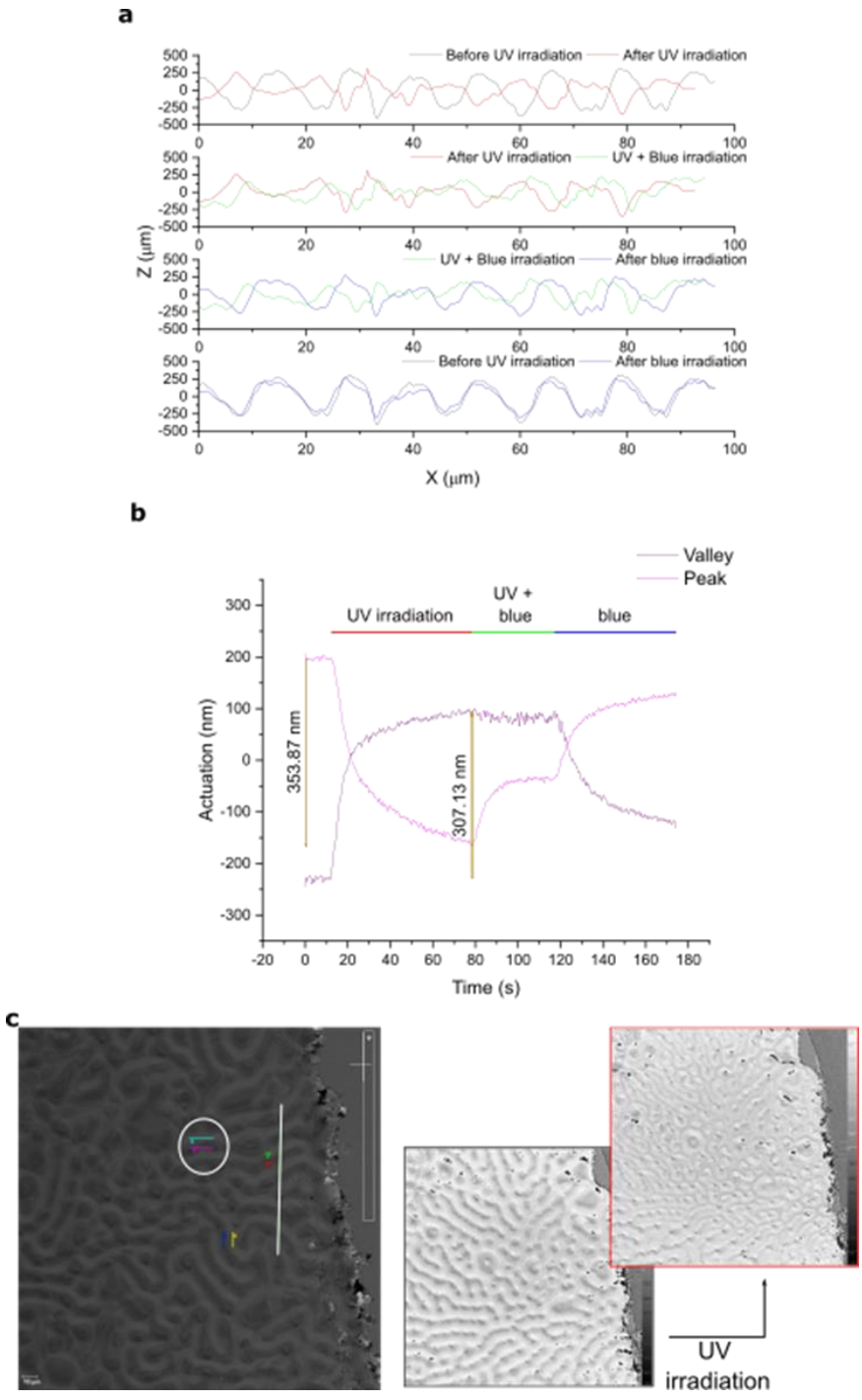

*Figure 3.17: Actuation of LCE coatings obtained with **LCN7** mixture. (a): Evolution of line profile (white line in c) during the different stages of the experiment. (b): Live actuation of two neighboring surface motifs (a peak and a valley enclosed in the white circle in c) at different stages of the experiment, under different*

illumination conditions. (c): DHM images of the LCE coating. Left: topography in the unactuated state, highlighting the line profile and the two structures whose live actuation is reported in a and b. Evolution of six different regions of the same sample was measured during each experiment (the colored squares in the image, as they were marked in Koala DHM software). Right: comparison between actuated and unactuated state of the LCE coating, showing topography inversion of the whole area observed.

The samples exhibited a non-linear dependence of percentage actuation on light power supplied and on temperature variation at constant light intensity (200 mW/cm^2) (Figure 3.18). In some cases, a displacement of peak and valley areas of about >300 nm was achieved; summing the two contributions and normalizing on sample initial thickness, an average percentage actuation of 4.15±1.22 % was obtained for samples prepared with **LCN7** mixture when actuated at 200 mW/cm^2 intensity for 60 s, which were the reference light power value and irradiation time throughout the study. Thus, all experiments were conducted irradiating the samples at 200 mW/cm^2 light intensity unless otherwise stated. **LCN7** coatings reached >5% actuation when irradiated at 300 mW/cm^2.

The decrease in percentage actuation at high temperature can be explained considering the thermal backwards isomerization of azobenzene, which could be the responsible of the actuation degree observed at 50°C and 75°C, which is similar to the value the LCE coatings exhibit at 25°C. On the other hand, the marked increase found when actuating the samples at 37°C can be explained based on the free volume effect mentioned above, and considering the glass transition temperature of the mixture, 33°C; when transitioning from glassy to rubbery, free volume increases in polymeric systems, thus the motility of the azobenzene moieties and the network is enhanced. This factor could explain the more-than-double rise in actuation when temperature was increased from 25°C to 37°C.

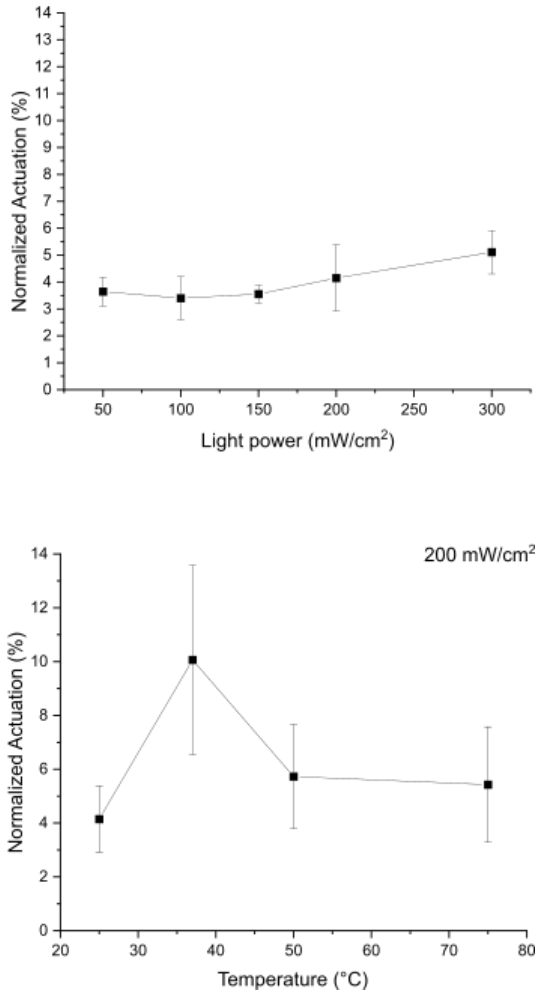

Figure 3.18: Dependence of percentage actuation on light intensity and temperature. Top: Actuation - light power curve, keeping the sample at room temperature. Bottom: Actuation – temperature curve, keeping light intensity constant at 200 mW/cm^2.

In view of the use of LCE coatings as active cell culture substrates with reconfigurable surfaces, their optical and thermal properties were characterized (Figure 3.19). Since UV light is harmful to live cells, it is important that, upon stimulation, the incident radiation is completely absorbed by the coating, not to reach the other side of the LCE where cells are cultured.

Thus, UV-Vis spectra for reflectance and transmittance were recorded for samples with 8% wt. **D3** dye (**LCN7**) and compared with samples with the same pitch containing 2%

wt. **D3** dye. Fingerprint-patterned surfaces equipped with 8% **D3** dye exhibited 2.4% transmittance and 3.9% reflectance at 385 nm; thus, 93.7% of incident light was absorbed or reflected by the polymer at the stimulation wavelength. On the other hand, samples with 2% wt. **D3** dye absorbed or reflected 64.6% of the incident light. Regarding thermal properties, heat generation was measured using a forward-looking IR camera upon irradiation of the coatings with UV light. Samples were kept at 25°C on a hotplate not to disperse heat on a cold surface. Networks with 2% wt. **D3** dye heated up to 35.6±0.3 °C upon irradiation, while the networks containing 8% wt. dye experienced a temperature increase to 38.5±0.3 °C when illuminated. This value is near cell culture conditions, 37°C, and could prove to be biocompatible in view of live cell stimulation experiments. However, tuning dye composition it is possible to modify the temperature increase in order to obtain a value within the biocompatible range.

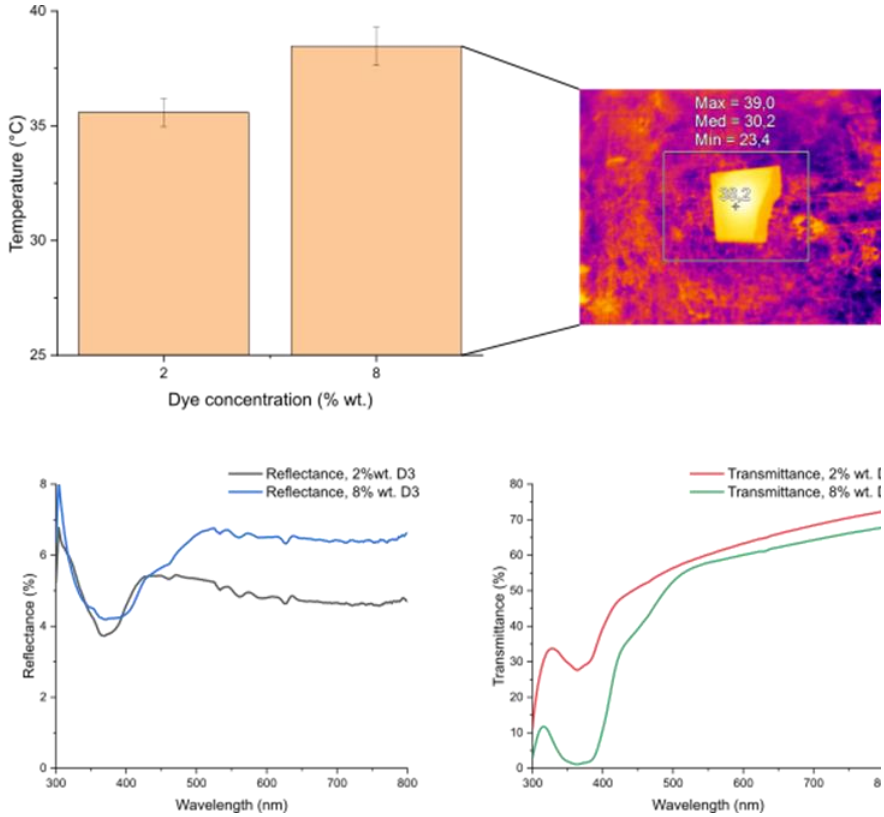

*Figure 3.19: Thermal and optical characterization of coatings from **LCN7** mixture. Top: temperature generation upon irradiation with UV light at 200 mW/cm^2 for 60 s. Samples from **LCN7** mixture are*

*compared with samples from **LCN6**, pinpointing the influence of dye content on temperature generation. Bottom: optical characterization of LCE coatings. **LCN7** and **LCN6** samples are compared.*

Biological experiments on fingerprint-patterned surfaces

To assess the biocompatibility of fingerprint patterns, cells were seeded on uncoated polymers, letting cells adhere and grow over their surface without any coating to enhance cell adhesion.

First, the influence of pattern spacing on cell adhesion and growth was evaluated, seeding cells on surfaces with two different chiral dopant amounts and, thus, pattern spacing (**LCN5-6**). In both cases, cells were sparsely distributed, and attached to the substrate in a few zones only, without firm interconnection among them. Compared to the Petri dish, the fingerprint patterns do not show any capability in supporting adhesion and growth of these two cell lines. Moreover, both murine C2C12 myoblasts and HDFs did not show any degree of spatial organization on both materials. In the case of dermal cells, plus, the number of adhered cells was very low, and the contact between neighboring cells was hindered (Figure 3.20).

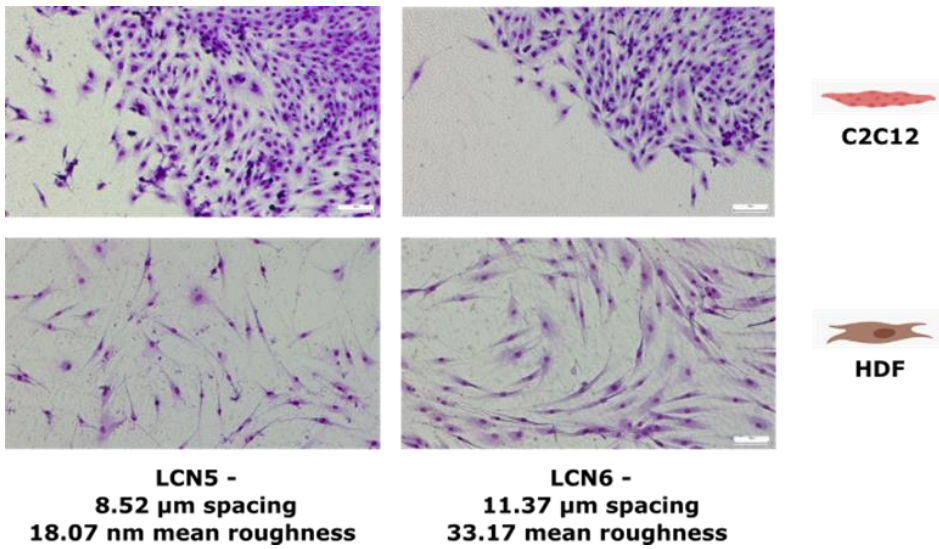

*Figure 3.20: Biocompatibility assessment of fingerprint-patterned substrate with low dye content and different pitch spacing (**LCN5-6**).*

Cells were also seeded on fingerprint-patterned surfaces with high dye content (**LCN7**), whose surface roughness is higher than in the previously used networks, to assess

whether the depth of the pattern could positively influence adhesion and growth of the two cell lines on the fingerprint-like coatings (Figure 3.21). On these substrates, however, adhesion was less firm than in the other samples. It is important to highlight that in these first experiments cells were seeded without any surface treatment to improve their adhesion, neither of chemical nature nor using protein-based coatings usually employed in biological experiments.

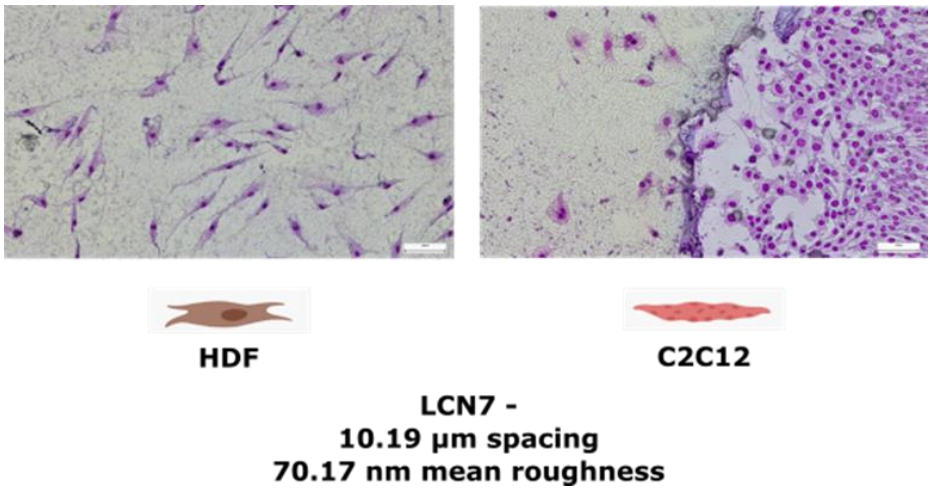

*Figure 3.21: Adhesion experiments on **LCN7** substrates with higher surface roughness compared to **LCN5** and **LCN6**. It is evident how cells did not adhere on the grooved polymer and died in both cases, both for HDFs and for murine C2C12 myoblasts. In the latter case, it is possible to see in the photo reported above how cells preferred the surface of the bare glass over the grooved surface.*

Next steps focused on the use of the LCEs treating them with an adhesion-promoting protein such as fibronectin, to enhance the adhesion and further explore the role of pattern spacing on cell functionality on fingerprint patterns, since it was observed that materials with fingerprint patterns inhibited cell adhesion, but samples without any kind of surface motif allowed randomly aligned cell growth (similarly to what happens on standard substrates).

A set of experiments was conducted to study the properties of **LCN7** coated with fibronectin and of **LCN5** on a planarly-aligning substrate (thus not showing fingerprint pattern), with and without fibronectin, towards the adhesion of C2C12 murine myoblasts. The former experiment had the objective to assess whether coating the surface motifs with an adhesion promoter such as fibronectin could lead to effective

adhesion of cells on the patterns, and thus unveil its role in inhibiting cell adhesion; the latter focused on the presence of **CL3**, to study if its presence was not beneficial to cell adhesion (cells grew on **LCN3-4** substrates without this component, but not on **LCN5-7**, which were equipped with **CL3** to give rise to fingerprints, so that concerns arose on the toxicity of this reagent to the cell lines employed). Results are shown in Figure 3.22. In the case of **LCN7**, cells could not adhere on the fingerprint pattern coated with fibronectin, thus confirming the poor biocompatibility of this particular structure towards C2C12 murine myoblasts. It is possible to confirm that this structure is not suitable for growth of muscle cells with these topographical characteristics.

In the other experiments, **LCN5** was deposited on a planarly-aligned polyimide. This way, the surface of the sample is not decorated with fingerprint motifs, since cholesteric helix does not lie parallelly to the glass substrate but indeed points perpendicularly to it. Cells could adhere on this kind of LC, which did not possess any surface structuring, even though the sample was not homogeneously covered by cells. Coating this substrate with fibronectin resulted in homogeneous growth, without any kind of cell ordering induced by LC ordering, similarly to what happened for **LCN3** and **LCN4**. Thus, neither substrate rigidity nor **CL3** presence hinder cell adhesion and growth, and these studies on fibronectin-coated samples confirmed how the only factor which hinders cell adhesion and growth of both cell lines on the LCE-based materials studied was the presence of the fingerprint surface pattern.

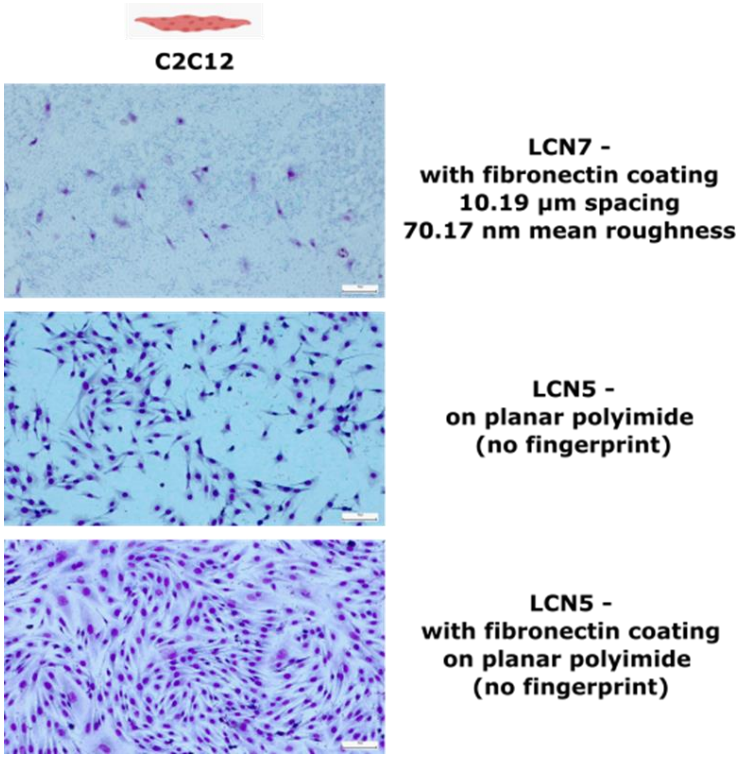

Figure 3.22: Characterization of LC substrates coated with fibronectin to enhance cell adhesion. From the top to the bottom: ***LCN7*** *samples, with fingerprint-like surface motifs;* ***LCN5*** *on planarly-aligning polyimide, thus with cholesteric helix direction pointing perpendicularly to the glass substrate, without and with fibronectin coating. Absence of fingerprint allows cell adhesion and growth.*

The reason underlying the ineffective adhesion and growth of cells on fingerprint-like structures could be found in the characteristics of the pattern.

Different models are being currently invoked to explain the response of cells to substrates with topographical cues (comprehensive reviews by Tamiello *et al*. and Leclech *et al*. deal with this topic).[105] *Focal adhesion* model is currently the most accepted theory within the scientific community to explain cell-substrate interaction, overall for submicron surface motifs, while for mesoscale topographical cues it is possible to take into account *gap avoidance* model. In the context of the former theory, alignment is possible only if groove width poses a geometrical constraint for focal adhesions (protein complexes which account for mechanosensing in cells) to grow in an ordered manner, without spreading homogeneously in all directions of the space; thus, it explains alignment through a biochemical pathway. The latter, instead, invokes

configurational entropy arguments to explain cell alignment on patterns, and minimization of contacts with non-adhesive gaps.[104,144] The correct mechanism is still debated, but both theories agree on the strong dependency of cell alignment on pattern characteristic length scale.

In the case of the study presented here, however, fingerprint spacing is large and maybe it did not provide cells neither with the necessary lateral confinement needed to firmly adhere on the substrate nor for the right contact area on top of the hills. Moreover, another reason for the difficulty of the chosen cell lines in attaching to the fingerprints could be found in the curvature of the pattern, which could have resulted steep for cells to stick on its surface.[104] Lastly, fingerprint spacing resulted to be maybe too large for cells to bridge the gap between two consecutive motifs, and their wavy structure did not provide them with the surface area necessary for them to attach to the surface and grow. Further research will have the objective of fabricating fingerprint-like structures with narrower spacing (thus increasing chiral dopant amount) in order to unveil the relation between the lateral features of the coatings and cell growth. Moreover, by carefully balancing UV light power that impinges on the substrate, a flat surface can be formed from fingerprint patterns upon partial topography inversion. Since the unpatterned cholesteric LC network presented above proved to be able to host cell cultures in its flat state, the non-adhesive properties of the fingerprint motifs could be exploited in the creation of a tunable adhesive/non-adhesive coating for cell cultures. A system in which there is coexistence of alternating zones in which growth is permitted and other zones where adhesion is inhibited could be fabricated, to drive migration and spatial patterning of cell cultures. Plus, if a tissue is formed on the flat fingerprint patterned structure, the non-adhesive properties of fingerprints could be exploited to trigger its separation from the substrate, towards the preparation of a self-detachable support.

3.2.4 Experimental section

Materials. Monoacrylate monomers **M2**, **M3** and the diacrylate crosslinker **CL2** were obtained from Merck GmbH. Chiral crosslinker **CL3** was purchased at BASF. Light-responsive crosslinker **D3** was purchased at Syncom. Photoinitiator **IN2** was purchased

at Ciba. All reagents are solid and used without any further purification. **M2** and **CL2** are liquid crystalline; **M3** shows a monotropic nematic phase and is added to broaden the nematic range of the mixture. **CL3** is a diacrylate chiral crosslinker used to induce the cholesteric mesophase. **D3** is a diacrylate azobenzene, which is responsive to UV light at 365 nm and blue light at 455 nm. **IN2** is a UV-responsive photoinitiator.

Fabrication. Glass substrates were cleaned by sonication in acetone for 20 min and in isopropanol for 20 min, dried with a nitrogen flux and treated with UV ozone for 20 min. To obtain planar alignment, polyimide AL1254 (Optimer) was used, while homeotropic anchoring of mesogens was achieved via the use of polyimide SE5661 (Nissan Sunever). Both polyimides were spin coated on the substrates at 800 rpm for 5 s and at 5000 rpm for 40 s. Spin coated substrates were cured on a hotplate for 10 min at 90°C and in oven for 90 min at 180°C. The reagents were dissolved in THF at various concentrations: 33% wt. concentration for nematic samples (without the addition of dopant **CL3**); at different concentrations (ranging between 25% wt. and 35% wt.), accordingly to the concentration of molecule **CL3** in each mixture, for chiral nematic ones. The nematic mixtures were spin coated at 4500 rpm for 30 seconds, either on planarly or homeotropically aligning polyimide-covered glass slides, and heat treatment (heating to 75°C on hotplate and subsequent slow cooldown at 2.5°C/min to 45°C) was conducted to enhance the alignment of liquid crystalline mesogens on the substrate. Chiral nematic mixtures were spin-coated on homeotropically aligning substrates at 1500 rpm for 30 s, and heat treatment was not needed to obtain self-assembled structures. Sometimes, to obtain more regular and reproducible structures by self-assembly of the cholesteric LC samples, unidirectional rubbing (using a velvet cloth) was carried out on the SE5661-polyimide-coated slides prior to casting the mixture on the substrate, and spin coating speed had to be slightly adjusted. Spin coated substrates were kept on a hotplate at 40°C to suppress crystallization of the LC mixture before polymerization. LC coatings were then photopolymerized from the top of the samples using a UV lamp (Omnicur EXFO S2000, Excelitas Technologies) equipped with a cut-off filter (FSQ-GG400, Newport) to prevent azobenzene isomerization during irradiation. The normalized power output of the light source was measured using a radiometer before polymerization (RM12

equipped with UVA+ detector, Opsytec Dr. Grobel GmbH). Photopolymerization of the samples was carried out under nitrogen atmosphere at 36°C (which lies within the liquid crystalline phase temperature ranges of all mixtures) in two stages: first, the samples were polymerized at low intensity; then, for 5 min at high intensity (100.0 mW/mm^2). Samples were baked at 120°C in nitrogen atmosphere after photopolymerization for 5 min afterwards. The final thickness of LC coatings depended on the concentration of solids and, for chiral nematic samples, on fingerprint pitch; it lied in the 3.5-5.5 μm range.

Characterization. The alignment of liquid crystalline substrates and the presence of fingerprint patterns were checked via polarized optical microscopy (DM6000, Leica). Attenuated total reflectance infrared (ATR-IR) spectroscopy (Varian 670-IR, Agilent) was used to assess polymerization degree of samples. Differential scanning calorimetry (DSC) was used to confirm transition temperatures of the mixtures (Q2000, TA Instruments) observed with the POM equipped with a hotstage. Surface topography was mapped using confocal microscopy (SNeox, Sensofar); sample thickness was measured by making a scratch on the coating and using interferometry to measure step height of the coating, taking the bare glass slide as a reference. Digital holographic microscopy in reflection configuration (DHM-R, Lyncée Tech) was used to live record the actuation pattern of the surfaces under light stimulation, using the bare glass as reference. Monochromatic light was provided by LED lamps at different emission wavelengths (M365LP1C1 and M455L3, Thorlabs). To calculate percentage actuation, a couple of a peak and the neighboring valley was chosen; then, its live actuation was followed under sustained irradiation (>60 s) with UV light, to reach a photostationary state in which the actuation of the surface was fully developed. Summing the contributions of the displacements of a single point from the valley rising upwards and the corresponding neighboring peak plunging, absolute actuation was evaluated. Then, this parameter was normalized on sample initial thickness. All experiments were conducted illuminating the sample with the UV light from the bottom using a UV-reflective mirror (BB01-E01, Thorlabs) and with the blue light from the top (the blue light is out of the frame on the left-hand side in Figure 3.23). Thermal images upon actuation were obtained through a

forward-looking IR camera (Fluke). UV-Vis spectra were recorded on a Shimadzu spectrometer.

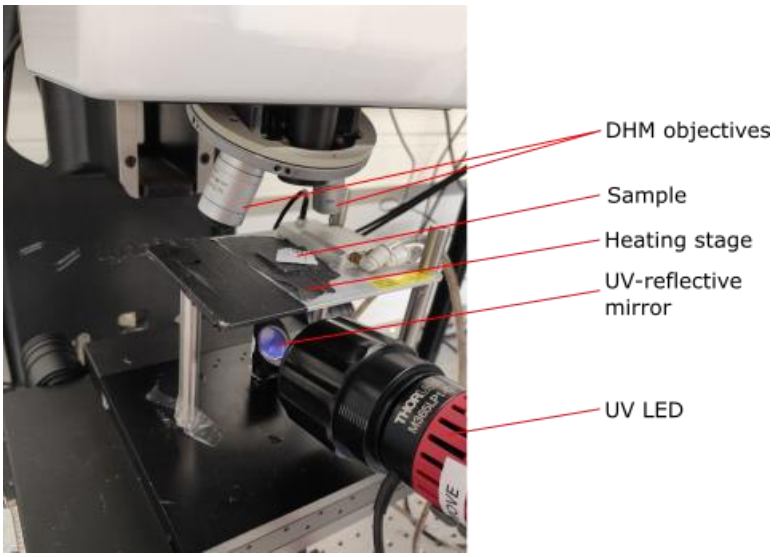

Figure 3.23: Experimental setup used to characterize sample actuation, comprising a digital holographic microscope in reflection mode (DHM-R), a UV LED, a UV-reflective mirror and a heating stage.

Data analysis. Polarized optical microscopy (POM) images were analyzed using ImageJ (National Institute of Health). Once the pixel-to-micrometer conversion was set, brightness and contrast were adjusted to have single peaks in images. To assess the distance between two consecutive surface reliefs (which is half of the cholesteric pitch), images with magnification of 50x, that allow an accurate estimation of the spacing between structures, were used. Then, the chosen image was converted to an 8-bit one and the topography along a line profile was analyzed by plotting grey value as a function of distance. Numeric data were analyzed using Originlab 2021 (OriginLab Corporation). Spacing between peaks (corresponding to planarly aligned areas, and hence two consecutive wells) was calculated, filtering outliers that result from artifacts in the images that give origin to secondary peaks, and averaged over a line profile. To measure step height, a profile line was drawn perpendicularly to the scratch on the sample, and calculated using SensoView software (Sensofar). To record topography, the central zone of the sample was mapped as the region of interest, using a 50x objective. Recommendations of ISO25178 norm were followed to obtain surface roughness and

areal parameters. Raw data were filtered removing the main slope and both short and long wavelength components, which account for microroughness and waviness.

Mean surface roughness S_a is used as metric for surface roughness for each sample, being $S_a = \frac{1}{A} \iint z(x,y)dxdy$. DHM images were analyzed using ImageJ to construct live actuation videos. Images were also used to extract line profiles to calculate actuation degree of the samples. Koala software (Lyncée Tech) was used to follow live actuation of the structures. In each field of view, six different zones with three couples of neighboring peaks and valleys were followed. Percentage actuation was obtained summing up the contribution of the neighboring motifs and normalizing this value by sample initial thickness. Results were averaged for each sample and each fabrication batch.

Each dataset of each physical quantity, containing averaged data for at least three experiments from all the fabrication batches, was checked for normality; data are expressed as mean ± standard error of the mean. Each fabrication batch contained at least 3 samples and at least 3 batches were fabricated for each mixture equipped with the chiral dopant.

Biological experiments. The samples were sterilized with several washings in ethanol and placed in 35 mm Petri dishes. Then, approximately 60.000 cells were seeded on the LCE coating. Those were incubated at standard cell culture conditions (37ºC in 5% CO_2 humidified atmosphere) on Dulbecco's Modified Eagle's Medium (DMEM) supplemented with 10% Fetal Bovine Serum (FBS). After 48h the films were washed with phosphate-buffered saline (PBS), fixed and stained with the Hemacolor staining kit (Merck). The presence of HDFs and C2C12 murine myoblasts adherent cells on the films was evaluated using a phase-contrast microscope. To coat the LC substrates with fibronectin, where needed, the protein was diluted in phosphate saline buffer, and the sample was immersed in the solution and incubated at cell culture conditions overnight. Excess solution was then removed, leaving the LC sample coated.

3.3. Conclusions

In this chapter, two research works were presented. Their common focus was the importance of scaffold materials to recapitulate the characteristics of a biological environment towards cell growth outside a natural context.

The first study had the objective of evaluating the influence of substrate rigidity to mimic the necessary conditions to grow hiPSC-CMs to full maturity. The importance of this type of reprogrammed stem cells in the biomedical field was examined in depth, pinpointing their role in drug and disease modeling and towards personalized medicine. Then, the most important cues to enhance growth of hiPSC-CMs were discussed, with a particular focus on substrate patterning and rigidity. The research work had the objective to compare different patterned substrates, obtained via soft lithography on a mixture of commercially available poly(ethylene glycol) oligomers equipped with acrylate ends and crosslinked with di(ethylene glycol) diacrylate, in hosting cultures of hiPSC-CMs. Their performance was assessed measuring the amplitude of their calcium transient and cell shortening percentage.

Results showed the superiority of a rigid substrate, composed of di(ethylene glycol) diacrylate only, which is tightly crosslinked. CMs cultured on this substrate, indeed, had a higher calcium transient amplitude and showed higher cell fractional shortening compared to blends of di(ethylene glycol) diacrylate with poly(ethylene glycol) diacrylate.

Further studies will have the objective of unveiling the relation between substrate rigidity and cell maturity, towards the use of other types of materials capable of stimulating cultured cells actively to broaden the spectrum of the mechanical cues available to reconstruct an environment similar to the one found *in vivo*.

The second work presented in this chapter had the objective of assessing the biocompatibility of a substrate based on cholesteric LCEs with reconfigurable surface upon light stimulation. Application of LCEs as cell scaffold represent one of the latest interests for researchers in this field; some examples of the use of these materials to fabricate substrates for cell growth were discussed, along with the physical phenomena underlying the preparation of fingerprint-patterned LCE coatings.

Starting from the first results on the use of nematic LCEs to host cell cultures, these first samples were modified with the addition of a chiral dopant in the mixture, to trigger fingerprint pattern formation, with alternating hills and valleys. Two different systems were prepared and characterized, with two different pattern spacings and surface roughness. The one with the most corrugated surface was then further modified to enhance its actuation upon light stimulation. Its morphology under UV irradiation was characterized: samples resulted capable of up-to-5% actuation upon stimulation, complete and reversible topography inversion (with valley rising upwards and hills plunging downwards), heat generation in a biocompatible temperature range. Biological experiments evaluated the biocompatibility of these fingerprint-patterned substrates towards C2C12 murine skeletal muscle cells and HDFs. However, the as-prepared untreated surfaces proved not to be able to host cultures of these cell lines, impeding cell adhesion and growth regardless of pattern spacing and surface roughness.

Another experiment, in which the previously prepared fingerprint patterned LCEs are covered with a protein-based coating for cell cultures, was carried out to understand if the coating with an adhesion-promoting protein could positively influence cell growth. However, C2C12 murine myoblasts could only grow on cholesteric LC coatings without fingerprint-like structures, that were prepared using a planarly-aligning polyimide layer to align LC mesogens. Thus, it was deduced that even though the LC mixtures used throughout this study possesses the right rigidity to host HDF and C2C12 myoblast cell cultures, neither they could not instruct their alignment, nor were capable to host cultures when the surface presented fingerprint-like patterns. Indeed, the large spacing between two consecutive motifs is too high to exert lateral confinement on cells and direct their growth, and curvature of the coating could also be another major determinant in the ineffectiveness of these substrates in hosting cell cultures.

The relation between lateral features, such as pattern spacing, and cell adhesion and growth will be the subject of further characterization, in view of the use of the reconfigurable surfaces to actively stimulate cells during growth and direct their migration.

4. Conclusions

Smart materials have the potential to revolutionize the current paradigms of materials science and engineering in all contexts of application. In the biomedical field, moreover, they possess a set of characteristics that allow them to overcome the limitations posed by standard materials, and to constitute the breakthrough in the design of a new generation of devices for the healthcare sector. Among the wide spectrum of smart materials, LCEs have become the newcomer in this context and are being extensively researched thanks to their particular properties. In the research work presented in this Thesis, two applications of LCEs in the biomedical field are discussed.

In chapter 2, the design of a miniaturized biomimetic contractile unit based on an array of miniLEDs and a light-responsive matrix composed of a LC material was discussed. The idea underlying the research was to realize a contraction assist device based on an LCE artificial muscle, following the first proof-of-concept results published by our research group on the possibility to support muscle contraction of a murine heart muscle. Thus, the objective was to improve the efficiency of the first system that was developed, acting on a two-pronged plan: on one side, the improvement of the performance of the material by tuning its composition and exploring new dyes to be embedded in the network; on the other side, the fabrication of a local miniaturizable illumination system to activate the LCE matrix. Switching to a dye with an absorption peak in the blue region of the visible spectrum and fabricating a double linear array of blue miniLEDs to stimulate the material, efficiency rose from 10^{-11} to almost 10^{-5}. This massive improvement in the performance of the system paves the way for the next steps of the study, which will take into account the possibilities offered by microLEDs to enhance the homogeneity of light stimulation of the material and the exploration of different mesogens, crosslinkers and processing methods to further improve the efficiency of the device.

Among the constraints posed by the current approach, indeed, sample size and alignment by surface effects are most limiting factors that hinder the upscaling of the artificial muscle. Nevertheless, the next phase of the research will focus on the use of shear-stress

alignment of LCE fibers through 3D printing and the use of photoalignment substrates on larger areas, to circumvent these size restrictions.

In chapter 3, the influence of topographical cues on cell growth and alignment is discussed, studying two applications of the use of substrates with surface patterns to direct cell ordering.

The objective of the first research work was to unveil the relation between two functional parameters, linked to contractility, and the rigidity of the culture substrate. The cell model employed were hiPSC-CMs cultured on nanopatterned grooved surfaces. The effectiveness of the ridged motifs in directing cell ordering had been established previously; in the course of the research presented here, the focus shifted to the effect of the rigidity of the substrate. Thus, crosslinking percentage was varied in a poly(ethylene glycol)-diacrylate/di(ethylene glycol)-diacrylate blend, varying the rigidity of the hydrogel. It was found that cells presented better functional parameters on the hydrogels with the highest rigidity among the four formulations prepared with increasingly crosslinker weight percentage. This study paves the way for further work combining mechanical, chemical and topographical signaling in order to develop a cell culture substrate able to recapitulate all the characteristics needed to guarantee cell growth of hiPSC-CMs to full maturity.

In the second study presented, dye-doped cholesteric LCEs with fingerprint surface motifs were studied as substrate for human dermal cells and C2C12 murine myoblasts, in view of their use as a reconfigurable scaffold able to live stimulate cells in culture. Fingerprints proved to be able to undergo full topography inversion, with peaks and valleys respectively plunging downwards and rising upwards upon light stimulation. The substrates had micron-sized pattern spacing and height, with up-to-5% actuation. However, the two cell lines studied did not adhere on the fingerprint-patterned substrates, maybe due to their large spacing. The objective of further study will be unveiling the relation between the lateral features of the surfaces and cell adhesion and growth, to explore the possibility to use fingerprint grooves with narrower spacing as cell scaffold.

References

1. Takagi, T. A Concept of Intelligent Materials. *J. Intell. Mater. Syst. Struct.* **1**, 149–156 (1990).
2. De Gennes, P. G. Réflexions sur un type de polymères nématiques. *C. R. Acad. Sci. Ser. B* **281**, 101–103 (1975).
3. Ferrantini, C. *et al.* Development of Light-Responsive Liquid Crystalline Elastomers to Assist Cardiac Contraction. *Circ. Res.* **124**, e44–e54 (2019).
4. Pioner, J. M. *et al.* Optical investigation of action potential and calcium handling maturation of hiPSC-cardiomyocytes on biomimetic substrates. *Int. J. Mol. Sci.* **20**, (2019).
5. Jones, R. A. L. *Soft condensed matter*. (Oxford University Press, 2002). doi:10.1088/0143-0807/23/6/703.
6. Demus, D., Goodby, J., Gray, G. W., Spiess, H. -W. & Vill, V. *Handbook of Liquid Crystals*. *Handbook of Liquid Crystals* vol. 26 (1998).
7. White, T. J. & Broer, D. J. Programmable and adaptive mechanics with liquid crystal polymer networks and elastomers. *Nat. Mater.* **14**, 1087–1098 (2015).
8. Hussain, M. *et al.* Liquid Crystal Elastomers for Biological Applications. *Nanomaterials* **11**, 813 (2021).
9. Broer, D. J., Crawford, G. P. & Žumer, S. Cross-linked liquid crystalline systems: From rigid polymer networks to elastomers. **20**, 1–615 (2011).
10. Warner, M. & Terentjev, E. M. *Liquid Crystal Elastomers*. (Oxford University Press, 2003).
11. de Jeu, W. H. *Liquid Crystal Elastomers: Materials and Applications*. (Springer Berlin Heidelberg, 2014).
12. Kularatne, R. S., Kim, H., Boothby, J. M. & Ware, T. H. Liquid crystal elastomer actuators: Synthesis, alignment, and applications. *J. Polym. Sci. Part B Polym. Phys.* **55**, 395–411 (2017).
13. Ula, S. W. *et al.* Liquid crystal elastomers: An introduction and review of emerging technologies. *Liq. Cryst. Rev.* **6**, 78–107 (2018).
14. Wani, O. M., Zeng, H., Wasylczyk, P. & Priimagi, A. Programming

Photoresponse in Liquid Crystal Polymer Actuators with Laser Projector. *Adv. Opt. Mater.* **6**, 2–7 (2018).

15. Küpfer, J. & Finkelmann, H. Nematic liquid single crystal elastomers. *Die Makromol. Chemie, Rapid Commun.* **12**, 717–726 (1991).
16. Clarke, S. M., Hotta, A., Tajbakhsh, A. R. & Terentjev, E. M. Effect of crosslinker geometry on equilibrium thermal and mechanical properties of nematic elastomers. *Phys. Rev. E - Stat. Physics, Plasmas, Fluids, Relat. Interdiscip. Top.* **64**, 8 (2001).
17. Bergmann, G. H. F., Finkelmann, H., Percec, V. & Zhao, M. Liquid-crystalline main-chain elastomers. *Macromol. Rapid Commun.* **18**, 353–360 (1997).
18. Beyer, P., Braun, L. & Zentel, R. (Photo)crosslinkable smectic LC main-chain polymers. *Macromol. Chem. Phys.* **208**, 2439–2448 (2007).
19. Ambulo, C. P. *et al.* Four-dimensional Printing of Liquid Crystal Elastomers. *ACS Appl. Mater. Interfaces* **9**, 37332–37339 (2017).
20. López-Valdeolivas, M., Liu, D., Broer, D. J. & Sánchez-Somolinos, C. 4D Printed Actuators with Soft-Robotic Functions. *Macromol. Rapid Commun.* **39**, 1700710 (2018).
21. Kotikian, A., Truby, R. L., Boley, J. W., White, T. J. & Lewis, J. A. 3D Printing of Liquid Crystal Elastomeric Actuators with Spatially Programed Nematic Order. *Adv. Mater.* **30**, 1–6 (2018).
22. Roach, D. J., Kuang, X., Yuan, C., Chen, K. & Qi, H. J. Novel ink for ambient condition printing of liquid crystal elastomers for 4D printing. *Smart Mater. Struct.* **27**, (2018).
23. Thomsen, D. L. *et al.* Liquid crystal elastomers with mechanical properties of a muscle. *Macromolecules* **34**, 5868–5875 (2001).
24. Schuhladen, S. *et al.* Iris-like tunable aperture employing liquid-crystal elastomers. *Adv. Mater.* **26**, 7247–7251 (2014).
25. Liu, D. & Broer, D. J. Liquid crystal polymer networks: Preparation, properties, and applications of films with patterned molecular alignment. *Langmuir* **30**, 13499–13509 (2014).

26. Martella, D., Nocentini, S., Nuzhdin, D., Parmeggiani, C. & Wiersma, D. S. Photonic Microhand with Autonomous Action. *Adv. Mater.* **29**, 1704047 (2017).
27. Komp, A., Rühe, J. & Finkelmann, H. A versatile preparation route for thin free-standing liquid single crystal elastomers. *Macromol. Rapid Commun.* **26**, 813–818 (2005).
28. Vasilets, V. N. *et al.* Orientational order of a nematic polymer grafted on polytetrafluoroethylene. *Polym. Adv. Technol.* **11**, 330–333 (2000).
29. Wermter, H. & Finkelmann, H. Liquid crystalline elastomers as artificial muscles. *E-Polymers* **1**, 1–13 (2001).
30. Hong, Y. *et al.* Micron-sized main-chain liquid crystalline elastomer actuators with ultralarge amplitude contractions. *J. Am. Chem. Soc.* **131**, 15000–15004 (2009).
31. Martella, D., Parmeggiani, C., Wiersma, D. S., Piñol, M. & Oriol, L. The first thiol-yne click chemistry approach for the preparation of liquid crystalline elastomers. *J. Mater. Chem. C* **3**, 9003–9010 (2015).
32. Lupi, F. *et al.* Dithiols as Liquid Crystalline Building Blocks for Smart Polymers via Thiol-yne Click Chemistry. *ACS Appl. Polym. Mater.* **3**, 1602–1609 (2021).
33. Royes, J. *et al.* Preparation of side-chain liquid crystalline Azopolymers by CuAAC postfunctionalization using bifunctional azides: Induction of chirality using circularly polarized light. *J. Polym. Sci. Part A Polym. Chem.* **50**, 1579–1590 (2012).
34. Sharma, A. *et al.* Biocompatible, biodegradable and porous liquid crystal elastomer scaffolds for spatial cell cultures. *Macromol. Biosci.* **15**, 200–214 (2015).
35. Herbert, K. M. *et al.* Synthesis and alignment of liquid crystalline elastomers. *Nat. Rev. Mater.* **7**, 23–38 (2022).
36. Cresta, V., Romano, G., Kolpak, A., Zalar, B. & Domenici, V. Nanostructured composites based on liquid-crystalline elastomers. *Polymers (Basel).* **10**, 1–27 (2018).
37. Ji, Y., Marshall, J. E. & Terentjev, E. M. Nanoparticle-liquid crystalline

elastomer composites. *Polymers (Basel).* **4**, 316–340 (2012).

38. Rastogi, P., Njuguna, J. & Kandasubramanian, B. Exploration of elastomeric and polymeric liquid crystals with photothermal actuation: A review. *Eur. Polym. J.* **121**, 109287 (2019).
39. Yu, H. & Ikeda, T. Photocontrollable liquid-crystalline actuators. *Adv. Mater.* **23**, 2149–2180 (2011).
40. C. H. Legge & G. R. Mitchell. Photo-induced phase transitions in azobenzene-doped liquid crystals. *J. Phys. D. Appl. Phys.* **25**, 492–499 (1992).
41. Sung, J. H. *et al.* Dynamics of photochemical phase transition of guest/host liquid crystals with an azobenzene derivative as a photoresponsive chromophore. *Chem. Mater.* **14**, 385–391 (2002).
42. Ikeda, T. Photochemical modulation of refractive index by means of photosensitive liquid crystals. *Mol. Cryst. Liq. Cryst. Sci. Technol. Sect. A Mol. Cryst. Liq. Cryst.* **364**, 187–197 (2001).
43. Li, M. H., Auroy, P. & Keller, P. An azobenzene-containing side-on liquid crystal polymer. *Liq. Cryst.* **27**, 1497–1502 (2000).
44. Finkelmann, H., Nishikawa, E., Pereira, G. G. & Warner, M. A new opto-mechanical effect in solids. *Phys. Rev. Lett.* **87**, 015501/1-015501/4 (2001).
45. Cembran, A., Bernardi, F., Garavelli, M., Gagliardi, L. & Orlandi, G. On the Mechanism of the cis-trans Isomerization in the Lowest Electronic States of Azobenzene: S0, S1, and T1. *J. Am. Chem. Soc.* **126**, 3234–3243 (2004).
46. Bandara, H. M. D. & Burdette, S. C. Photoisomerization in different classes of azobenzene. *Chem. Soc. Rev.* **41**, 1809–1825 (2012).
47. Weis, P. & Wu, S. Light-Switchable Azobenzene-Containing Macromolecules: From UV to Near Infrared. *Macromol. Rapid Commun.* **39**, 1–12 (2018).
48. Wang, X. *Trans–Cis Isomerization*. (2017). doi:10.1007/978-3-662-53424-3_2.
49. Williams, D. F. *Definitions in Biomaterials: Proceedings of a Consensus Conference of the European Society for Biomaterials, Chester, England, March 3-5, 1986*. (Elsevier, 1987).
50. *Biomaterials Science An Introduction to Materials in Medicine*. *Biomaterials*

Science: An Introduction to Materials: Third Edition (Elsevier Inc., 2013).

51. Machado, L. G. & Savi, M. A. Medical applications of shape memory alloys. *Brazilian J. Med. Biol. Res.* **36**, 683–691 (2003).
52. Wang, K., Strandman, S. & Zhu, X. X. A mini review: Shape memory polymers for biomedical applications. *Front. Chem. Sci. Eng.* **11**, 1–11 (2017).
53. Martella, D. & Parmeggiani, C. Advances in Cell Scaffolds for Tissue Engineering: The Value of Liquid Crystalline Elastomers. *Chem. - A Eur. J.* **24**, 12206–12220 (2018).
54. World Health Organization. The top 10 causes of death. https://www.who.int/news-room/fact-sheets/detail/the-top-10-causes-of-death (2020).
55. Division for Heart Disease and Stroke Prevention & National Center for Chronic Disease Prevention and Health Promotion. Heart Disease. https://www.cdc.gov/heartdisease/index.htm (2021).
56. Department of Economic and Social Affairs - United Nations. Goal 3: Ensure healthy lives and promote well-being for all at all ages. https://sdgs.un.org/goals/goal3 (2015).
57. United Nations Statistics Division. Goal 3: Ensure healthy lives and promote well-being for all at all ages. https://unstats.un.org/sdgs/report/2016/goal-03/ (2016).
58. Zoghbi, W. A. *et al.* Sustainable development goals and the future of cardiovascular health: A statement from the global cardiovascular disease Taskforce. *J. Am. Heart Assoc.* **3**, 1–2 (2014).
59. Tanai, E. & Frantz, S. Pathophysiology of heart failure. *Compr. Physiol.* **6**, 187–214 (2016).
60. Han, J. & Trumble, D. Cardiac Assist Devices: Early Concepts, Current Technologies, and Future Innovations. *Bioengineering* **6**, 18 (2019).
61. Radisic, M. & Christman, K. L. Materials science and tissue engineering: Repairing the heart. in *Mayo Clinic Proceedings* vol. 88 884–898 (Elsevier Inc, 2013).

62. Zhang, J., Zhu, W., Radisic, M. & Vunjak-Novakovic, G. Can we engineer a human cardiac patch for therapy? *Circ. Res.* **123**, 244–265 (2018).
63. Mirvakili, S. M. & Hunter, I. W. Artificial Muscles: Mechanisms, Applications, and Challenges. *Adv. Mater.* **30**, 1–28 (2018).
64. Mantovani, D. Shape memory alloys: properties and biomedical applications. *Jom* **52**, 36–44 (2000).
65. Sabahi, N., Chen, W., Wang, C. H., Kruzic, J. J. & Li, X. A Review on Additive Manufacturing of Shape-Memory Materials for Biomedical Applications. *Jom* **72**, 1229–1253 (2020).
66. Sarvari, R. *et al.* Shape-memory materials and their clinical applications. *Int. J. Polym. Mater. Polym. Biomater.* **0**, 1–21 (2020).
67. Leng, J., Lu, H., Liu, Y., Huang, W. M. & Du, S. Shape-memory polymers - A class of novel smart materials. *MRS Bull.* **34**, 848–855 (2009).
68. Kirillova, A. & Ionov, L. Shape-changing polymers for biomedical applications. *J. Mater. Chem. B* **7**, 1597–1624 (2019).
69. Haines, C. S. *et al.* Artificial muscles from fishing line and sewing thread. *Science (80-.).* **343**, 868–872 (2014).
70. Ariano, P. *et al.* Polymeric materials as artificial muscles: An overview. *J. Appl. Biomater. Funct. Mater.* **13**, 1–9 (2015).
71. Hsiao, J. H., Chang, J. Y. & Cheng, C. M. Soft medical robotics: clinical and biomedical applications, challenges, and future directions. *Adv. Robot.* **33**, 1099–1111 (2019).
72. Sanchez, V., Walsh, C. J. & Wood, R. J. Textile Technology for Soft Robotic and Autonomous Garments. *Adv. Funct. Mater.* **2008278**, 1–55 (2020).
73. Martella, D. *et al.* Liquid Crystalline Networks toward Regenerative Medicine and Tissue Repair. *Small* **13**, 1–8 (2017).
74. Martella, D. *et al.* Liquid Crystal-Induced Myoblast Alignment. *Adv. Healthc. Mater.* **8**, 1–10 (2019).
75. Verduzco, R. *et al.* Electromechanically Responsive Liquid Crystal Elastomer Nanocomposites for Active Cell Culture. *ACS Macro Lett.* **5**, 1386–1390 (2016).

76. Prévôt, M. E. *et al.* Liquid crystal elastomer foams with elastic properties specifically engineered as biodegradable brain tissue scaffolds. *Soft Matter* **14**, 354–360 (2018).
77. Prévôt, M. E., Ustunel, S. & Hegmann, E. Liquid crystal elastomers-A path to biocompatible and biodegradable 3D-LCE scaffolds for tissue regeneration. *Materials (Basel).* **11**, (2018).
78. Nocentini, S., Martella, D., Parmeggiani, C. & Wiersma, D. S. Photoresist design for elastomeric light tunable photonic devices. *Materials (Basel).* **9**, 1–11 (2016).
79. Guin, T. *et al.* Layered liquid crystal elastomer actuators. *Nat. Commun.* **9**, 1–7 (2018).
80. Saed, M. O. *et al.* Thiol-acrylate main-chain liquid-crystalline elastomers with tunable thermomechanical properties and actuation strain. *J. Polym. Sci. Part B Polym. Phys.* **55**, 157–168 (2017).
81. Ware, T. H. & White, T. J. Programmed liquid crystal elastomers with tunable actuation strain. *Polym. Chem.* **6**, 4835–4844 (2015).
82. Kotikian, A., Truby, R. L., Boley, J. W., White, T. J. & Lewis, J. A. 3D Printing of Liquid Crystal Elastomeric Actuators with Spatially Programed Nematic Order. *Adv. Mater.* **30**, 1–6 (2018).
83. Saed, M. O. *et al.* High strain actuation liquid crystal elastomers via modulation of mesophase structure. *Soft Matter* **13**, 7537–7547 (2017).
84. Ghazali, F. A. M. *et al.* Micro-electromechanical-system actuators for biomedical applications: a review. *J. Micromechanics Microengineering* **30**, 073001 (2020).
85. El-Atab, N. *et al.* Soft Actuators for Soft Robotic Applications: A Review. *Adv. Intell. Syst.* **2**, 2000128 (2020).
86. Kongahage, D. & Foroughi, J. Actuator materials: Review on recent advances and future outlook for smart textiles. *Fibers* **7**, (2019).
87. Ambulo, C. P. *et al.* Processing advances in liquid crystal elastomers provide a path to biomedical applications. *J. Appl. Phys.* **128**, (2020).
88. Miriyev, A., Stack, K. & Lipson, H. Soft material for soft actuators. *Nat. Commun.* **8**, 1–8 (2017).

89. Huang, X. *et al.* Shape memory materials for electrically-powered soft machines. *J. Mater. Chem. B* **8**, 4539–4551 (2020).

90. Özkaya, N., Leger, D., Goldsheyder, D. & Nordin, M. *Fundamentals of Biomechanics: Equilibrium, Motion, and Deformation*. *Fundamentals of Biomechanics* (Springer International Publishing AG, 2016).

91. Tesi, C., Colomo, F., Piroddi, N. & Poggesi, C. Characterization of the cross-bridge force-generating step using inorganic phosphate and BDM in myofibrils from rabbit skeletal muscles. *J. Physiol.* **541**, 187–199 (2002).

92. Piroddi, N. *et al.* Tension generation and relaxation in single myofibrils from human atrial and ventricular myocardium. *Pflugers Arch. Eur. J. Physiol.* **454**, 63–73 (2007).

93. Martella, D. *et al.* Light activated non-reciprocal motion in liquid crystalline networks by designed microactuator architecture. *RSC Adv.* **7**, 19940–19947 (2017).

94. Zeng, H., Wani, O. M., Wasylczyk, P. & Priimagi, A. Light-Driven, Caterpillar-Inspired Miniature Inching Robot. *Macromol. Rapid Commun.* **39**, 1–6 (2018).

95. Nocentini, S., Martella, D., Micheletti, F., Parmeggiani, C. & Wiersma, D. S. Polarization-dependent deformation in light responsive polymers doped by dichroic dyes. *Soft Matter* **15**, 1312–1318 (2018).

96. Zeng, H. *et al.* High-resolution 3d direct laser writing for liquid-crystalline elastomer microstructures. *Adv. Mater.* **26**, 2319–2322 (2014).

97. Jansen, K. A. *et al.* A guide to mechanobiology: Where biology and physics meet. *Biochim. Biophys. Acta - Mol. Cell Res.* **1853**, 3043–3052 (2015).

98. Kim, H. N. *et al.* Nanotopography-guided tissue engineering and regenerative medicine. *Advanced Drug Delivery Reviews* vol. 65 536–558 (2013).

99. Li, Y. *et al.* Engineering cell alignment in vitro. *Biotechnol. Adv.* **32**, 347–365 (2014).

100. Li, Y., Xiao, Y. & Liu, C. The Horizon of Materiobiology: A Perspective on Material-Guided Cell Behaviors and Tissue Engineering. *Chem. Rev.* **117**, 4376–4421 (2017).

101. Chueng, S. T. D., Yang, L., Zhang, Y. & Lee, K. B. Multidimensional nanomaterials for the control of stem cell fate. *Nano Converg.* **3**, (2016).

102. Li, W., Yan, Z., Ren, J. & Qu, X. Manipulating cell fate: dynamic control of cell behaviors on functional platforms. *Chem. Soc. Rev.* **47**, 8639–8684 (2018).

103. Kim, D. H. *et al.* Nanoscale cues regulate the structure and function of macroscopic cardiac tissue constructs. *Proc. Natl. Acad. Sci. U. S. A.* **107**, 565–570 (2010).

104. Leclech, C. & Barakat, A. I. Is there a universal mechanism of cell alignment in response to substrate topography? *Cytoskeleton* **78**, 284–292 (2021).

105. Tamiello, C., Buskermolen, A. B. C., Baaijens, F. P. T., Broers, J. L. V. & Bouten, C. V. C. Heading in the Right Direction: Understanding Cellular Orientation Responses to Complex Biophysical Environments. *Cell. Mol. Bioeng.* **9**, 12–37 (2016).

106. Yang, Y., Wang, K., Gu, X. & Leong, K. W. Biophysical Regulation of Cell Behavior—Cross Talk between Substrate Stiffness and Nanotopography. *Engineering* **3**, 36–54 (2017).

107. Guimarães, C. F., Gasperini, L., Marques, A. P. & Reis, R. L. The stiffness of living tissues and its implications for tissue engineering. *Nat. Rev. Mater.* **5**, 351–370 (2020).

108. Liu, G., David, B. T., Trawczynski, M. & Fessler, R. G. Advances in Pluripotent Stem Cells: History, Mechanisms, Technologies, and Applications. *Stem Cell Rev. Reports* **16**, 3–32 (2020).

109. Pioner, J. M. Novel in vitro models for mechanistic studies on genetic cardiomyopathies : human iPSC- derived cardiomyocytes. (Università degli Studi di Siena, 2016).

110. Kalra, S., Montanaro, F. & Denning, C. Can Human Pluripotent Stem Cell-Derived Cardiomyocytes Advance Understanding of Muscular Dystrophies? *J. Neuromuscul. Dis.* **3**, 309–332 (2016).

111. Santoro, R., Perrucci, G. L., Gowran, A. & Pompilio, G. Unchain My Heart: Integrins at the Basis of iPSC Cardiomyocyte Differentiation. *Stem Cells Int.*

2019, (2019).

112. Ahmed, R. E., Anzai, T., Chanthra, N. & Uosaki, H. A Brief Review of Current Maturation Methods for Human Induced Pluripotent Stem Cells-Derived Cardiomyocytes. *Front. Cell Dev. Biol.* **8**, 1–9 (2020).
113. Macadangdang, J. *et al.* Nanopatterned Human iPSC-Based Model of a Dystrophin-Null Cardiomyopathic Phenotype. *Cell. Mol. Bioeng.* **8**, 320–332 (2015).
114. Au, H. T. H., Cheng, I., Chowdhury, M. F. & Radisic, M. Interactive effects of surface topography and pulsatile electrical field stimulation on orientation and elongation of fibroblasts and cardiomyocytes. *Biomaterials* **28**, 4277–4293 (2007).
115. Kitsara, M., Agbulut, O., Kontziampasis, D., Chen, Y. & Menasché, P. Fibers for hearts: A critical review on electrospinning for cardiac tissue engineering. *Acta Biomater.* **48**, 20–40 (2017).
116. Querceto, S. *et al.* The harder the climb the better the view: The impact of substrate stiffness on cardiomyocyte fate. *J. Mol. Cell. Cardiol.* **166**, 36–49 (2022).
117. Ribeiro, M. C. *et al.* A cardiomyocyte show of force: A fluorescent alpha-actinin reporter line sheds light on human cardiomyocyte contractility versus substrate stiffness. *J. Mol. Cell. Cardiol.* **141**, 54–64 (2020).
118. Carson, D. *et al.* Nanotopography-Induced Structural Anisotropy and Sarcomere Development in Human Cardiomyocytes Derived from Induced Pluripotent Stem Cells. *ACS Appl. Mater. Interfaces* **8**, 21923–21932 (2016).
119. Ellis, A. B. *et al.* Replication and Compression of Surface Structures with Polydimethylsiloxane Elastomer. *J. Chem. Educ.* **76**, 537 (2009).
120. Schlecht, C. A. & Maurer, J. A. Functionalization of glass substrates: Mechanistic insights into the surface reaction of trialkoxysilanes. *RSC Adv.* **1**, 1446–1448 (2011).
121. Lupi, F. Photopolymerization approaches towards smart responsive surfaces and materials. (Università degli Studi di Firenze, 2019).

122. Luk, Y. Y., Campbell, S. F., Abbott, N. L. & Murphy, C. J. Non-toxic thermotropic liquid crystals for use with mammalian cells. *Liq. Cryst.* **31**, 611–621 (2004).
123. Lockwood, N. A. *et al.* Thermotropic liquid crystals as substrates for imaging the reorganization of matrigel by human embryonic stem cells. *Adv. Funct. Mater.* **16**, 618–624 (2006).
124. Yakacki, C. M. *et al.* Tailorable and programmable liquid-crystalline elastomers using a two-stage thiol-acrylate reaction. *RSC Adv.* **5**, 18997–19001 (2015).
125. Shaha, R. K. *et al.* Biocompatible liquid-crystal elastomers mimic the intervertebral disc. *J. Mech. Behav. Biomed. Mater.* **107**, 103757 (2020).
126. Kirkwood, J. E. & Fuller, G. G. Liquid crystalline collagen: A self-assembled morphology for the orientation of mammalian cells. *Langmuir* **25**, 3200–3206 (2009).
127. Martella, D. *et al.* Liquid Crystalline Networks toward Regenerative Medicine and Tissue Repair. *Small* **13**, 1–8 (2017).
128. Martella, D. *et al.* Cell Instructive Liquid Crystalline Networks for Myotube Formation. *iScience* **24**, 103077 (2021).
129. Turiv, T. *et al.* Topology control of human fibroblast cells monolayer by liquid crystal elastomer. *Sci. Adv.* **6**, 1–11 (2020).
130. Koçer, G. *et al.* Light-Responsive Hierarchically Structured Liquid Crystal Polymer Networks for Harnessing Cell Adhesion and Migration. *Adv. Mater.* **29**, 1–8 (2017).
131. Hendrikx, M. *et al.* Re- and Preconfigurable Multistable Visible Light Responsive Surface Topographies. *Small* **14**, (2018).
132. Babakhanova, G. *et al.* Cell alignment by smectic liquid crystal elastomer coatings with nanogrooves. *J. Biomed. Mater. Res. - Part A* **108**, 1223–1230 (2020).
133. Jiang, J. *et al.* Controlled Dynamics of Neural Tumor Cells by Templated Liquid Crystalline Polymer Networks. *Adv. Healthc. Mater.* **9**, 1–8 (2020).
134. Chilaya, G. Always cholesterics⋯ but sometimes chiral smectic C, TGB and blue

phases. *Mol. Cryst. Liq. Cryst.* **561**, 8–35 (2012).

135. Feng, W. Topographical deformation of electro / light-active liquid crystal coatings. (Technische Universiteit Eindhoven, 2020).
136. Liu, D. & Broer, D. J. Self-assembled dynamic 3D fingerprints in liquid-crystal coatings towards controllable friction and adhesion. *Angew. Chemie - Int. Ed.* **53**, 4542–4546 (2014).
137. Ligon-Auer, S. C., Schwentenwein, M., Gorsche, C., Stampfl, J. & Liska, R. Toughening of photo-curable polymer networks: A review. *Polymer Chemistry* vol. 7 257–286 (2016).
138. Feng, W. *et al.* Static and Dynamic Control of Fingerprint Landscapes of Liquid Crystal Network Coatings. *ACS Appl. Mater. Interfaces* **12**, 5265–5273 (2020).
139. Yager, K. G., Tanchak, O. M., Godbout, C., Fritzsche, H. & Barrett, C. J. Photomechanical effects in azo-polymers studied by neutron reflectometry. *Macromolecules* **39**, 9311–9319 (2006).
140. Visschers, F. L. L., Hendrikx, M., Zhan, Y. & Liu, D. Liquid crystal polymers with motile surfaces. *Soft Matter* **14**, 4898–4912 (2018).
141. Liu, D. Volume generation towards dynamic surface morphing in liquid crystal polymer networks. *Liq. Cryst.* **43**, 2136–2143 (2016).
142. Liu, D. & Broer, D. J. New insights into photoactivated volume generation boost surface morphing in liquid crystal coatings. *Nat. Commun.* **6**, (2015).
143. Feng, W., Broer, D. J. & Liu, D. Combined Light and Electric Response of Topographic Liquid Crystal Network Surfaces. *Adv. Funct. Mater.* **30**, (2020).
144. Buskermolen, A. B. C. *et al.* Cellular Contact Guidance Emerges from Gap Avoidance. *Cell Reports Phys. Sci.* **1**, 100055 (2020).

Acknowledgments

The results of the work I carried out through these years and my personal and scientific growth would have not been possible without the help of a lot of people, who I will try to kindly thank here for their effort, their help, their time.

I would like to thank Prof. Camilla Parmeggiani for her supervision and guidance, along with Prof. Diederik S. Wiersma.
I thank the whole research group of Optics of Complex Systems at the European Laboratory for Non-Linear Spectroscopy for the beautiful moments we have been through and the inspiring discussions.
A special thank goes to our collaborators at the Department of Experimental and Clinical Medicine at the Università degli Studi di Firenze, to Prof. Cecilia Ferrantini and the Division of Physiology, and to Dr. Leonardo Sacconi.
I would like to express my truest gratitude to the Stimuli-Responsive Functional Materials and Devices (SFD) research group at Eindhoven Technical University, for having hosted me during my exchange period in their laboratories. I thank Prof. Dirk J. Broer and Prof. Danqing Liu for their kindness and help during the six months I spent in Eindhoven. *Bedankt*.